UNIVERSITY OF CALIFORNIA
RIVERSIDE

A Model-Data Approach to Evaluating Long-Term Warming and Carbon Cycle Changes Across the Late Paleocene to Early-Middle Eocene

A Thesis submitted in partial satisfaction
of the requirements for the degree of

Master of Science

in

Geological Sciences

by

Adam Kazimierz Aleksinski

December 2018

Thesis Committee:
Dr. Sandra Kirtland Turner, Chairperson
Dr. Andrew Ridgwell
Dr. Robert Allen

The Thesis of Adam Kazimierz Aleksinski is approved:

_____

_____

_____

Committee Chairperson

University of California, Riverside

ACKNOWLEDGMENTS

First and foremost, I owe my most sincere gratitude to my advisor, Dr. Sandra Kirtland Turner, for providing me with an amazing opportunity to study a subject that had fascinated me for quite some time but had been out of my wheelhouse until recently. Admittedly, this academic journey was challenging, particularly in the beginning, but Dr. Kirtland Turner's patience and persistence helped me to overcome these difficulties, and fostered in me a sense of enthusiasm and confidence in my project. I can say with certainty that I am excited to explore this subject matter further in the future. Many thanks also go to my other committee members, Drs. Andrew Ridgwell and Robert Allen. I am most grateful to them for imparting to me several of the skills that I have used every day of my research, including coding and experimenting with climate models. I owe thanks to my lab-mates as well, for their insightful comments, advice, and assistance with my work, and I must especially thank Allison Keller and Dr. Ying Lin for their irreplaceable help in the mass spectrometry lab. Lastly, I would like to thank my parents, Mariette and Tomasz Aleksinski, and my lifelong friends, Christopher Garcia and Jeffrey Briggs. They were there to cheer me on when I had the confidence to succeed, and they were there to believe in me when I did not.

Finances for this project were provided by UC Riverside's Graduate Student Fellowship, as well as teaching assistantships through the Earth Science Department, and Dr. Kirtland Turner's graduate student research fund.

ABSTRACT OF THE THESIS

A model-data approach to evaluating long-term warming and carbon cycle changes across the late Paleocene to early-middle Eocene

by

Adam Kazimierz Aleksinski

Master of Science, Graduate Program in Geological Sciences
University of California, Riverside, December 2018
Dr. Sandra Kirtland Turner, Chairperson

There is ample evidence from benthic foraminiferal oxygen isotope records that the Earth's climate experienced dramatic long-term variations from the late Paleocene to early-middle Eocene. Beginning from ~57 Ma and culminating in the Early Eocene Climate Optimum (EECO) between ~53-51 Ma, the recorded 1‰ decrease in $\delta^{18}O$ indicates warming of ~4 to 5 °C, followed by the onset of long-term cooling at the early-middle Eocene boundary (~48 Ma). Benthic foraminifera also record major changes in carbon isotopes during this time period, with a decline in $\delta^{13}C$ of ~2 to 2.5‰, indicating that the temperature changes coincided with profound changes in the carbon cycle. These trends are consistent with an overall increase in atmospheric CO_2 for the duration of the event, perhaps caused by a protracted increase in volcanic outgassing or decrease in net organic carbon burial. However, there is a temporal offset between the benthic foraminiferal $\delta^{13}C$ and $\delta^{18}O$ signals, with the long-term minimum in $\delta^{13}C$ significantly preceding peak global temperatures indicated by the long-term minimum in $\delta^{18}O$. If a

global signal, this offset may suggest changes in the source of carbon fluxes across this interval of long-term global warming, rather than the existence of a single-source carbon forcing and resultant temperature response. To constrain possible causes of the offset, we first analyze the relative timing of isotope signals from each individual site within the Cramer et al. 2009 benthic foraminiferal stable isotope composite. Our analysis shows that trends in $\delta^{13}C$ consistently lead trends in $\delta^{18}O$ at each site. However, the length of the offset varies significantly between sites. We find that the duration of this offset is greatest at southern sites, potentially indicating that changing patterns of deep-water formation contribute to the apparent decoupling between $\delta^{13}C$ and $\delta^{18}O$ trends. As $\delta^{13}C$ is a gauge of water mass age, spatial gradients in benthic foraminiferal $\delta^{13}C$ can indicate regional differences in deep water formation, shedding light on the evolution of global circulation. We next take an additional investigative approach utilizing the cGENIE intermediate complexity Earth system model. We use cGENIE in order to test the impact of enhanced volcanic outgassing on spatial patterns in benthic $\delta^{13}C$ and deep ocean temperature, and relate this to changes in the large-scale ocean overturning circulation.

TABLE OF CONTENTS

LIST OF FIGURES

LIST OF EQUATIONS

LIST OF TABLES

CHAPTER 1 – INTRODUCTION AND BACKGROUND

The Paleogene period (ca. 65-23 Ma) has long been of keen interest to researchers interested in the behavior of the Earth's systems during periods of varying climate extremes. From this interest, a rich collection of climate reconstructions, featuring marine, atmospheric, and ecological data, has been assembled over several decades of research. Of particular note is the transition between the late Paleocene epoch (ca. 56 Ma) and the early-to-mid Eocene epoch (ca. 48 Ma), which features many anomalous events characterized by substantial climatic heating, which appear to occur repeatedly until a cooling pattern began to prevail in the mid-to-late Eocene (Figure 1, Zachos et al., 2008). These unprecedented warming events have been of great interest to paleoclimatologists, as they have been hypothesized to have been caused by exceptional increases in marine and atmospheric carbon and thus an enhanced greenhouse effect, and are often thought of as analogues to modern-day anthropogenic climate change. The short-lived warming events, frequently known as hyperthermals, are particularly associated with the early Eocene epoch, are believed to be the result of extremely abrupt (typically less than 20 kyr) carbon releases, and also are characterized by rapid recovery (typically less than 40 kyr) (Turner et al., 2014). While the exact identity of the carbon sources that drove hyperthermals is widely disputed, two of the most accepted candidates are volcanogenic and methanogenic sources (Dickson et al., 2015; Zeebe et al., 2009). These hyperthermals occurred against the backdrop of a much longer-lived warming event

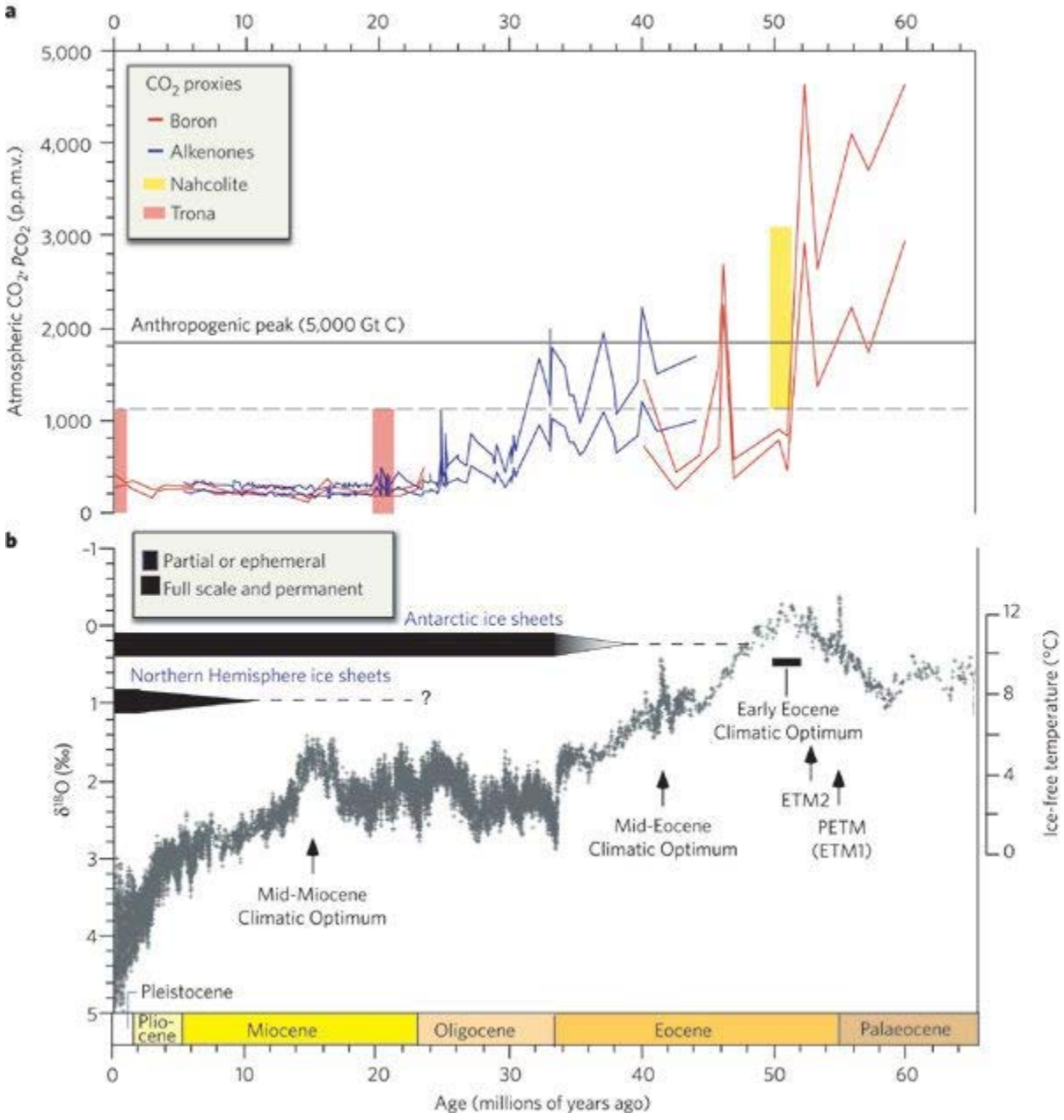

Figure 1: Aggregated ρCO_2 (a) and deep ocean temperature (b) data across the Cenozoic era, from Zachos *et al*., (2008). Prominent hyperthermals include PETM (the Paleocene-Eocene Thermal Maximum, also called ETM1) and ETM2. The climate remains very warm through the Early Eocene Climatic Optimum, until recovery of the carbon cycle brings temperatures on a downward trend.

known as the Early Eocene Climatic Optimum (EECO). EECO took place between ~51 and ~53 Ma and recorded global average deep ocean temperatures as high as 12 °C (Zachos et al., 2008). Whereas hyperthermals were most likely caused by sudden and short-lived carbon releases, EECO persisted for approximately two million years and was indicative of a much larger change to the carbon cycle and climate, suggesting fundamentally different drivers compared to the hyperthermals. Hypotheses regarding the timing and magnitude of the climate forcing associated with EECO have pointed to large and long-lived instances of volcanic activity, such as the active period of the North Atlantic Igneous Province (NAIP; between 62-52 Ma, with a very prominent eruption occurring at 54 Ma), but this has not been established as the primary cause of the perturbation (Egger and Brückl, 2006; Saunders et al., 1997). As such, gaining knowledge of the Earth's carbon cycle and climate dynamics through EECO would provide fundamental understanding of the controls on Earth's climate system, with particular relevance for understanding the long-term climate response to radical shifts in the Earth's carbon reservoirs occurring today.

In order to assemble catalogues of climatic data through the Earth's history, researchers have long used a well-established repository of oceanic conditions from the late Mesozoic through Cenozoic: the fossils of marine microorganisms, accumulated over millions of years as seafloor sediment. This approach draws on two important aspects of the preservation of such organisms in deep sea marine sediment. First, techniques exist to constrain sedimentation rates of marine sediment deposits, such as detailed biostratigraphy and magnetostratigraphy and the measurement of cosmogenic radiogenic

nuclides; thus, age models can be constructed with great precision, especially when concerning open ocean sediments that have minimal terrestrial input (Eldrett et al., 2004; Schmitz and Davydov, 2012). Second, these marine microorganisms, such as foraminifera, coccolithophorids, radiolarians, and others, all construct their various tests, shells and skeletons from the seawater that surrounds them, suggesting that they preserve snapshots of marine chemistry (Spero et al., 1997). Unlike other more widely motile sea life, the geographic range of these organisms is tightly constrained, and they may be assumed to have lived at the same locality as their remains are found in sediments today. In this study, and in many others that precede it, foraminifera are the prime target for analysis. These zooplanktic protists construct their tests from calcium carbonate ($CaCO_3$), utilizing Dissolved Inorganic Carbon (DIC) from their immediate surroundings, and within this carbonate, they record the stable isotopic values of both the carbon and the oxygen of their marine environment. These isotopes provide valuable information about the temperature and the carbon cycle of the ocean that the foraminifera lived in, and thus can be used as paleo-proxies for vital marine and climatic metrics. The ratio of stable oxygen isotope oxygen-18 to the more common oxygen-16 in a foraminifera sample, when compared to a well-known standard such as the Vienna Pee Dee Belemnite (‰VPDB) value, is reported as $\delta^{18}O$. This relationship is defined in Equation 1 below.

$$\delta^{18}O = (((^{18}O/^{16}O)_{sample} / (^{18}O/^{16}O)_{VPDB}) - 1) \times 1000‰$$

Equation 1: The relationship between $\delta^{18}O$ and the isotope values measured from a sample and the VPDB standard. Note that $\delta^{13}C$ is calculated in a very similar manner, only using ^{13}C measurements rather than ^{18}O, and ^{12}C measurements rather than ^{16}O.

$\delta^{18}O$ is a metric of the isotopic composition of the oxygen concomitant with seawater. As a measurement, it is highly useful as a paleothermometer, as increased or decreased fractionation with respect to oxygen-18 within marine carbonate minerals, such as those that comprise foraminifera tests, is dependent on the ambient temperature of the surrounding water (Epstein and Mayeda, 1953; McCrea, 1950). By utilizing measurements of $\delta^{18}O$ from foraminifera samples, with a calibrated paleotemperature equation - such as the inorganic carbonate fractionation equation described in Kim and O'Neil (1997) in Equation 2 below - the water temperature of the foraminifera's marine environment can be ascertained and linked to the age of the foraminifera (Bemis et al., 1998). For ice-free climates like the Paleogene, a value of -1.27‰ is typically assumed for seawater $\delta^{18}O$ (Zachos et al., 2001).

$$T(°C) = 16.1 - 4.64(\delta_c - \delta_w) + 0.09(\delta_c - \delta_w)^2$$

Equation 2: Paleotemperature equation for the formation of inorganic calcite, as investigated by Kim and O'Neil (1997). The calculation of the formation temperature is dependent on the difference between the isotopic composition of the analyzed carbonate sample (δ_c) and the surrounding water (δ_w). Thus, δ_w must be known or assumed.

A second metric utilized in this study, referred to as $\delta^{13}C$, is similarly the ratio of stable carbon-13 to the more abundant carbon-12, reported once again relative to ‰VPDB. $\delta^{13}C$ reflects the composition of carbon dissolved in seawater. The links between $\delta^{13}C$ in a foraminifera sample and the underlying climatic forcing is more nuanced than for $\delta^{18}O$, as many factors may be responsible for a change in the stable carbon isotope ratio within marine calcium carbonate (Hayes et al., 1999; Kroopnick et al., 1972). Organic processes, such as photosynthesis of surface algae and

methanogenesis of aquatic microbes, fractionate strongly with a preference towards the lighter carbon-12 isotope. Thus, widespread events of consistently high organic carbon productivity (if accompanied by subsequent sedimentary burial) remove carbon-12 from the oceans, leaving a signature of increased marine $\delta^{13}C$ (Kump and Arthur, 1999; Shackleton, 1987). The opposite occurs if global productivity dramatically slows down, resulting in decreases in marine $\delta^{13}C$, but this same kind of signature may also be produced through an increase of volcanic outgassing, as the $\delta^{13}C$ of volcanic-produced carbon dioxide is also depleted relative to marine DIC $\delta^{13}C$, and as volcanic outgassing increases, more of this isotopically-light carbon is dissolved into the oceans (Raymo and Ruddiman, 1992). Therefore, more constraints are needed when diagnosing the cause of shifts in global average carbon isotopic compositions.

Constraints on the paleo-coordinates and paleodepth of sites where fossil foraminifera are obtained are important to correctly interpret foraminiferal geochemical data, but this knowledge is pointless if no consideration is taken to the depth habitat of the analyzed foraminifera. Foraminifera typically have one of two different lifestyles. Planktic foraminifera live in the upper water column and produce a record of the ocean chemistry at varying depths, while benthic foraminifera live at the seafloor and thus record marine conditions only at this level. The variety of foraminifera that is analyzed thus has a large impact on the interpretation of the data that is produced. Isotope measurements taken from planktic foraminifera or from bulk carbonate samples – with measurements taken from the aggregate carbonate of the sample, rather than selected specimens of microfossils – tend to reflect the upper water column, while measurements

from benthic foraminifera express ocean chemistry at the ancient seafloor at the sampling site. The difference between planktic and benthic foraminiferal isotopes, in turn, is also indicative of variations in the ocean-climate system. Vertical ocean circulation between the surface and the deep waters, or ocean overturning, mixes the isotopic composition of the water from shallow to deep depths. Because photosynthesizing organisms live at the surface for readily available sunlight, their activity removes carbon-12 from seawater and increases local $\delta^{13}C$ (Freeman and Hayes, 1992). As organisms near the surface die and sink to the seafloor, respiration of their remains returns carbon-12 the deep waters; thus, when there is little vertical mixing taking place, benthic $\delta^{13}C$ measurements are considerably lighter than those of the upper water column, even at the same geographic location (Zachos et al., 2008). This changes near a site of overturning. High-$\delta^{13}C$ water from the surface ocean is brought deeper, which increases the $\delta^{13}C$ at those depths. Since benthic foraminifera record stable isotopes at the seafloor, the isotope measurements taken from them (from abyssal locations) can be compared to those of coeval planktic foraminifera in order to determine the local prevalence of overturning, which in turn provides a useful context for the state of general ocean circulation for the time period (Cramer et al., 2009).

The use of carbon and oxygen isotopes to compare the past ocean chemistry, along with the differentiation of planktic and benthic specimens to target specific ocean layers, have been in the paleoceanographer's arsenal for decades, and through their application, researchers have been able to characterize changes in Earth's climate and carbon cycle from the late Mesozoic through the Cenozoic (Thomas and Shackleton, 1996). One of the

most thorough compilations of this deep-sea stable isotope data to date has been that of Cramer et al. (2009). In it, Cramer assembled a multitude of past $\delta^{18}O$ and $\delta^{13}C$ benthic foraminiferal datasets from many locations into a single composite, with the goal of illustrating the extent of interior ocean mixing over the past 80 million years. While Cramer utilized the compilation to examine large-scale changes in the ocean composition, these data also provide a unique opportunity to investigate discrete compositional histories of the deep ocean at various Deep Sea Drilling Project / Ocean Drilling Project (DSDP/ODP) sites on the same age scale. In doing this, it is possible to examine inter-site differences in the timing of isotopic signatures that signify important climatic events since the Cretaceous, including EECO. Because benthic $\delta^{13}C$ has utility as a tracer of ocean overturning, the relative timing of $\delta^{13}C$ minima between sites of varying position may be linked to the state of ocean circulation at the time of foraminiferal test formation.

There exists, however, an odd characteristic in EECO-spanning isotope datasets that becomes apparent in Cramer's compilation. These datasets indicate a long asynchronicity between the carbon and oxygen isotope signals, with the carbon isotope minimum leading the oxygen isotope minimum associated with EECO by as much as 1.5 Myr. If EECO warming was driven by a single carbon source, this does not make sense; the carbon and oxygen signals should be temporally synchronous, with a gap between temperature and carbon cycle responses existing for no longer than a few thousand years (Figure 2, Kump & Arthur 1999). More recent box modeling has been unable to reproduce this asynchronicity; for instance, Komar et al. (2013) utilized a coupled

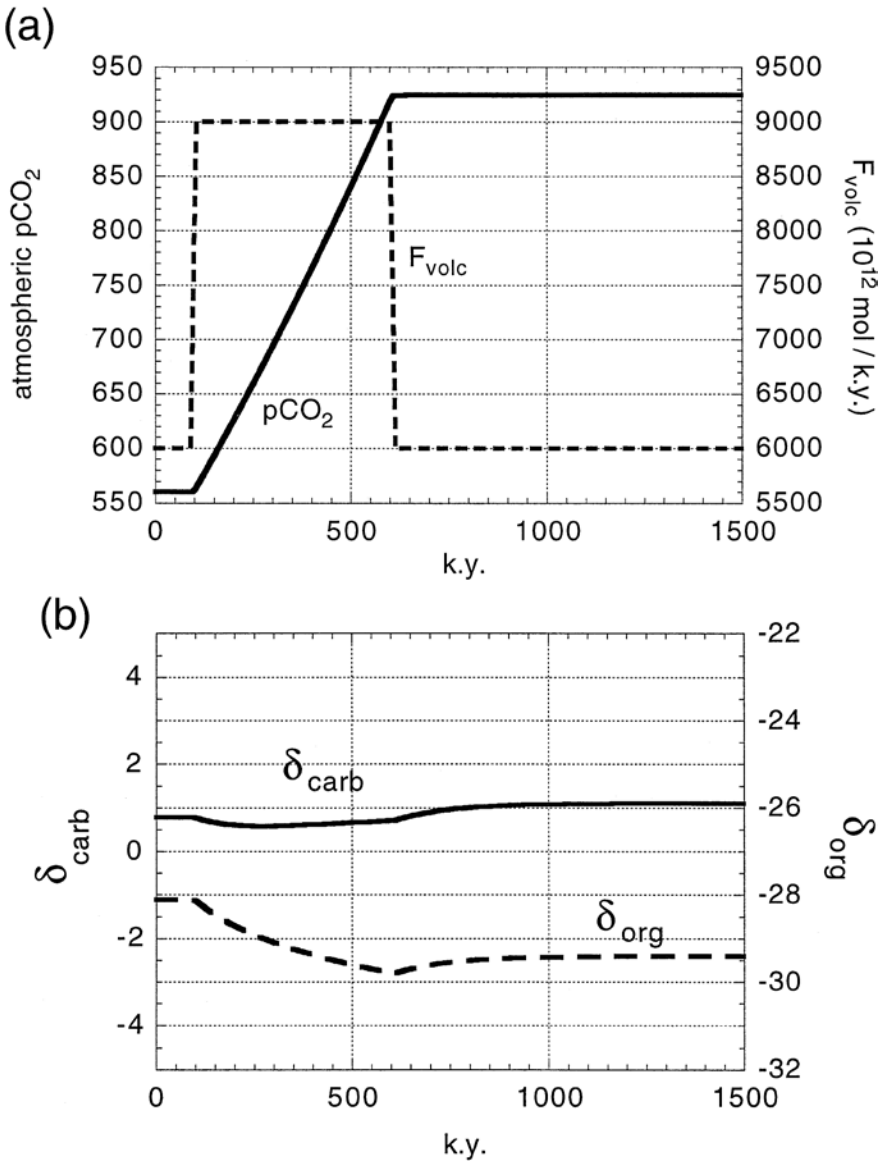

Figure 2: Generalized model response of atmospheric pCO_2 and marine carbon isotopes to simulated volcanic perturbation to the carbon cycle from Kump & Arthur (1999). Atmospheric pCO_2 reaches its peak only very slightly before the carbon isotope minima take place.

GEOCARB III-LOSCAR modeling approach based on extensive benthic foraminiferal data and were unable to reproduce this temporal offset between carbon and oxygen isotope signatures. Instead, this study modeled temperature and carbon isotope shifts as occurring contemporaneously, regardless of what carbon source was used to force the model (Figure 3). Because this does not reflect the published data, it may be inferred that there is a more complicated story behind the carbon cycle changes that fueled EECO.

In this study, I use a variety of methods, including direct numerical analysis of the Cramer benthic foraminiferal composite and experiments with an intermediate complexity Earth system model to investigate possible causes of this offset. Rather than comparing broad interbasinal isotopic gradients as Cramer does, I examine the isotopic chronology of each individual site featured in the compilation across the late Paleocene through early Eocene. I also utilize cGENIE, an intermediate complexity Earth system model, in order to test the impact of various carbon injection scenarios on the isotopic signatures of the deep ocean, and compare these model values to benthic foraminiferal data at various time periods that span EECO. Finally, I generate a high-resolution benthic foraminiferal isotopic dataset, local to ODP Site 1258 on the Demerara Rise off the coast of Guyana, and mainly focusing on the 52-50 Ma age range (at the height of EECO). This is one of the highest resolution benthic foraminiferal stable isotope datasets across EECO. In combination with the similarly-high resolution bulk carbonate dataset from Turner et al. (2014), I determine the vertical carbon isotope and temperature gradients across EECO. Combined, these methods elucidate changes in ocean dynamics through the warmest interval of the past 65 million years of Earth history.

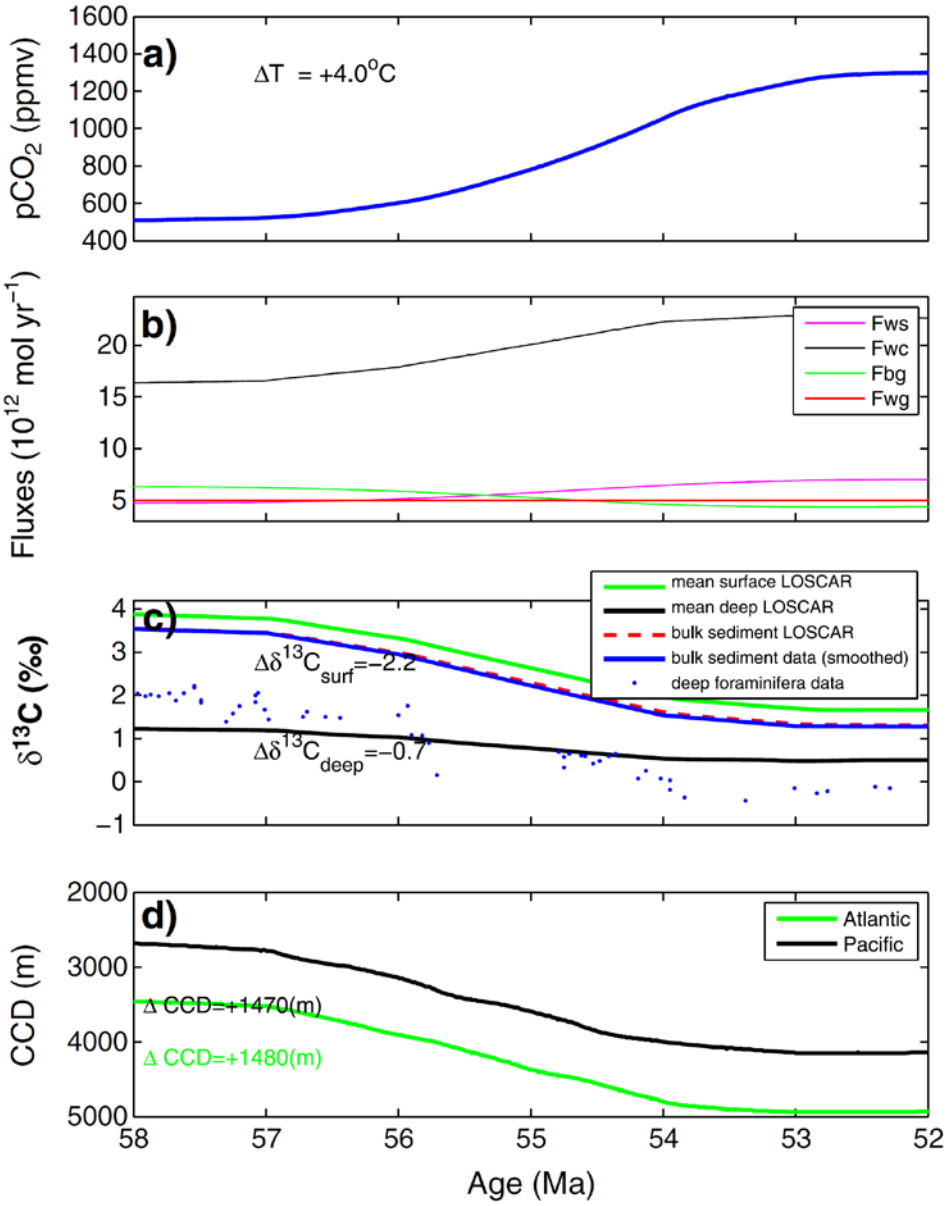

Figure 3: LOSCAR + GEOCARB III model results of Paleocene-Eocene long-term carbon cycle simulation from Komar *et al*. (2013). The onset of long-term warming shown here takes place at the same time as long-term global decreases in $\delta^{13}C$.

CHAPTER 2 – METHODOLOGY

2.1 – SITE-BASED ANALYSIS OF THE CRAMER COMPOSITE

The analysis of the published global benthic isotope data necessitated a unique decomposition of the Cramer compilation. The goal of this analysis was to elucidate the relative trends in $\delta^{18}O$ and $\delta^{13}C$ present in each site utilized in the compilation. I conducted this analysis of the Cramer data using MATLAB. Since this study is focusing on signals present from the late Paleocene through the early Eocene, I only analyzed the segment of the Cramer compilation that ranged in age from 60 Ma to 45 Ma. Then, from this slice of the compilation, I sorted the data by site so that carbon and oxygen isotope records could be examined on an individual basis. As a result, the data initially utilized for this analysis include 18 different Deep Sea Drilling Project (DSDP) and Ocean Discovery Program (ODP) drilling sites: DSDP sites 098, 384, 401, 525, 527, 528, 550, and 577, and ODP sites 689, 690, 698, 702, 738, 865, 1051, 1209, 1258, and 1260.

Because the Cramer dataset was assembled for examining broad interbasinal trends, the data separated by site was not immediately suitable for analysis (Figure 4). Therefore, it was necessary to perform some initial processing on the newly segregated datasets before proceeding. First, there were many ages that had duplicate isotope values, or even multiple different values, due to the compilation being assembled from several different studies. In order to ensure that the trends derived from the segregated datasets were accurate, I identified all isotope datapoints that had the same ages for each site. Next, upon identification of redundant datapoints, I took the mean of the isotope values among the points in question and created a new datapoint with that mean value at the

examined age, and erased all the original duplicates, leaving only the mean values. This way, redundant datapoints were eliminated from the datasets while preserving the values that they represent (Figure 5).

Not all of the datasets utilized in the Cramer compilation were intended for the same use, and this is evident through a quick glance at the data from each site. Some sites targeted specifically for the study of early Cenozoic climate have incredible age resolution throughout my slice of the Cramer compilation, while other sites have considerably sparser values in my time slice. For such sites, a few erratic data points lend a lot more weight to the evaluation of trends, which should be avoided if possible. Therefore, in my initial processing of the segregated datasets, I linearly interpolated between gaps to get each dataset as uniform as possible, so that trends evaluated from

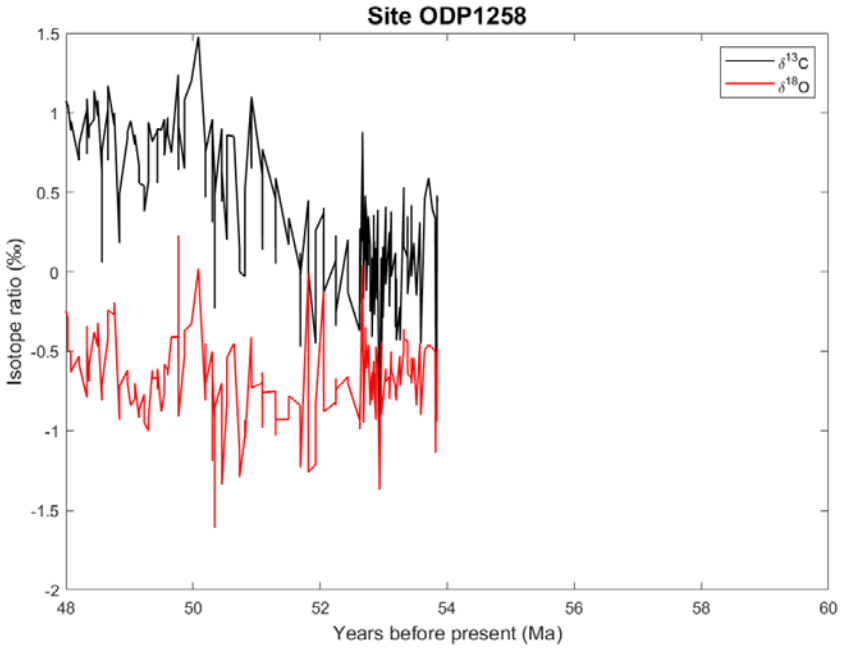

Figure 4: Example of unprocessed Cramer *et al*. (2009) compilation data for ODP Site 1258.

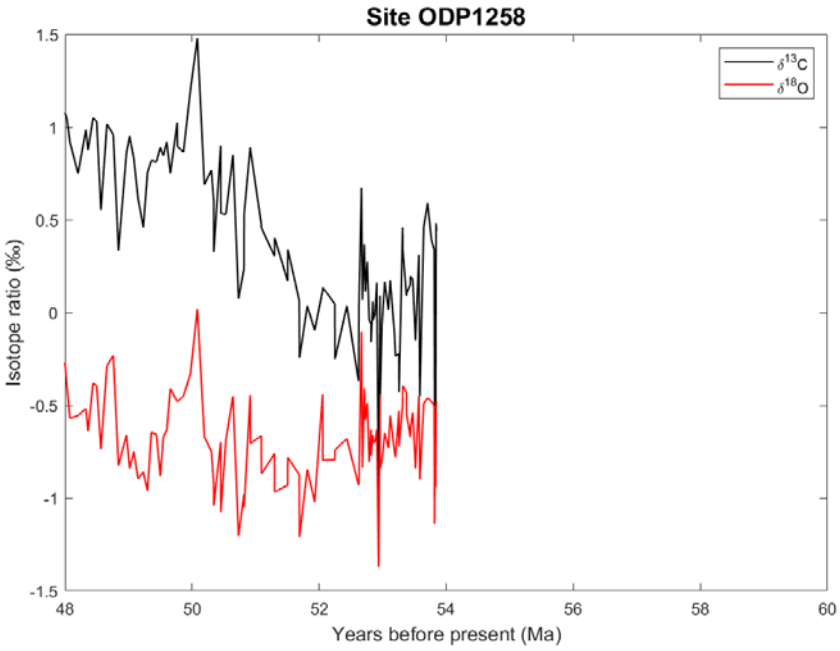

Figure 5: Example of Cramer *et al*. (2009) compilation data for ODP Site 1258 after duplicate datapoints are culled.

these datasets might be more comparable to each other. I first assessed the age range in the dataset being processed. I used the age range of the datasets as the indicator for the ideal density of datapoints that was necessary for a reliable trend to be derived; for example, a dataset that spans several millions of years would need a higher number of datapoints than one that only spans a couple hundred thousand years. Thus, the density of data for each dataset was calculated from the total age range of the dataset divided by 1,200 years, so that the data resolution of the interpolation is even higher than that of the sites with the highest resolution. The starting age, ending age, and the density of data were all utilized as query points in the linear interpolation (Figure 6). Although this interpolation solved inconsistencies in data resolution and sparsity, the resulting data was

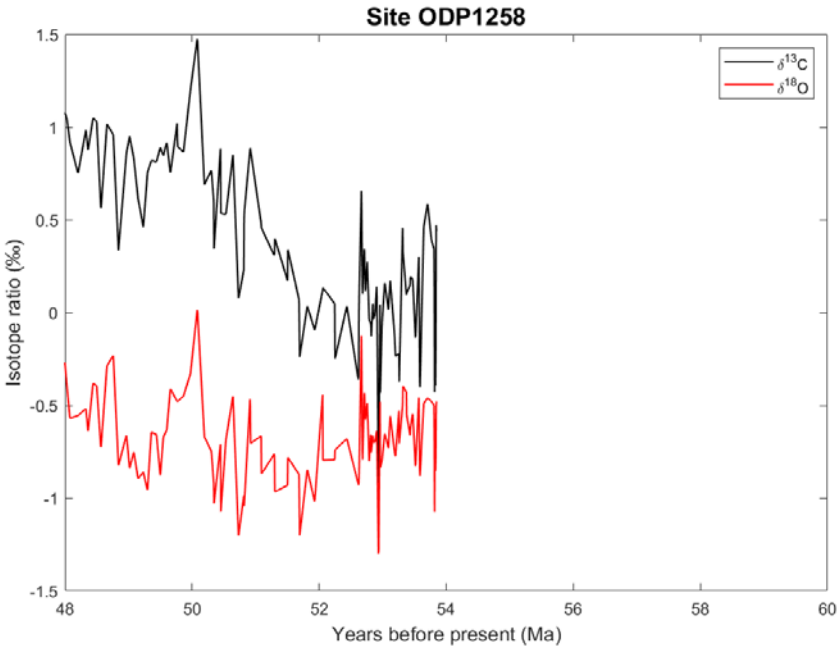

Figure 6: Example of Cramer *et al*. (2009) compilation data for ODP Site 1258 after interpolation operation is performed.

still too noisy for reliably establishing a trend. Next, I smoothed the data according to the "loess" method, which utilizes a quadratic regression over a moving window, as this algorithm appeared to cut through signal noise the most readily. The smoothed dataset is overlain on top of the cleaned dataset in all plots (Figure 7).

Finally, the datasets were ready for trend analysis — in other words, determination of the relative timing of minima in carbon and oxygen isotopes at each site. Trends were established here through the identification of the timing of minima in the isotopic records, which should correspond to EECO conditions. These are numerically identified as the absolute minimum in each datasets for each series of data. Unfortunately, MATLAB does not have a built-in capability for identifying absolute

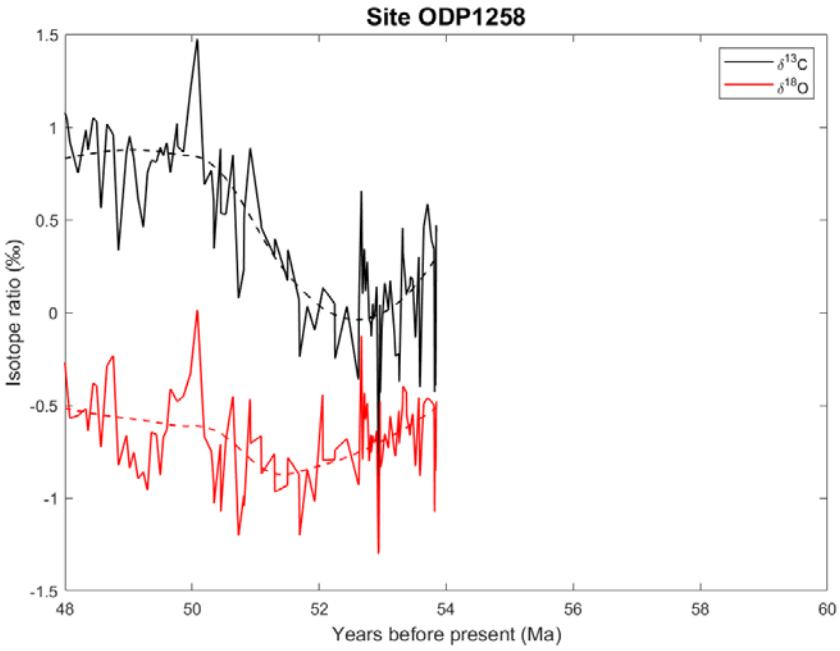

Figure 7: Example of Cramer *et al*. (2009) compilation data for ODP Site 1258 after smoothing operation is performed, with results overlaid with prior data.

minima, but this was sidestepped by creating a dummy version of each dataset with the signs on each value flipped, and identifying the position of the absolute maximum of the dummy set. This, naturally, corresponded to the position of the absolute minimum of the true dataset. This generally reliably located the isotopically-measured height of EECO as recorded in the $\delta^{18}O$ paleotemperature proxy, and its accompanying decrease in $\delta^{13}C$, at each sample location. Finally, I calculated the difference in time between the minimum of $\delta^{18}O$ and the minimum of $\delta^{13}C$ for each site, and reported this as the discrepancy in synchronicity between the signals.

For further analysis of the regional differences in the magnitude of the isotope signal asynchronicity, I next examined the correlation between the magnitude of the

asynchronicity at each sampling site and the distance of the site from the equator (i.e. the absolute value of the site's decimal latitude). For this, I directly compared the time difference between the oxygen and carbon isotope minima at each site versus the absolute value of the site's decimal latitude. To show the strength of correlation, a linear regression was performed on this pair of value sets. I also performed some simple correlation tests between asynchronicity magnitude and a few other sets of geographical parameters, including paleo-depth and true latitude.

2.2 – PROOF-OF-CONCEPT CGENIE EXPERIMENTS

Earth systems models are powerful tools that can simulate millions of years of progressive ocean and climate changes as they respond to various perturbations, shifts in landmass, alterations in biotic activity, and much more. Utilizing such a model can help to assess the paleo-ocean and climate conditions that led up to EECO, and to determine potential processes that could explain the asynchronicity between the carbon and oxygen isotope signals. The intermediate-complexity cGENIE Earth system model (www.seao2.info/mycgenie.html) can effectively simulate the evolution of ocean-atmosphere chemistry over long timescales (up to ~1 Myr), features a robust suite of tracers for various marine conditions (including carbon isotopes), and makes for an ideal platform to perform modeling experiments in this study.

cGENIE includes a frictional 3D geostrophic ocean model, with a 36×36 horizontal grid equal-area in longitude and sine of latitude and 16 vertical levels increasing in thickness with depth, coupled with a relatively simple 2D energy-moisture

balance-based atmospheric model and a sea-ice component (Cao et al., 2009; Edwards and Marsh, 2005; Weaver et al., 2001). Crucially for this study, cGENIE also represents the cycling of a wide array of biogeochemical tracers, including carbon (Ridgwell et al., 2007). The cGENIE model is not without some limitations, however. For this project, the version of the model used is not capable of recording or altering changes in the burial of sedimentary organic carbon. This limitation is particularly important, as variations in this flux have a large impact on the carbon budget of the oceans and atmosphere, and have potentially significant impacts on climate (Zachos et al., 2008).

cGENIE experiments, when started completely fresh, assume a completely uniform ocean with no stratification or currents. Thus it is necessary to let the model's oceans come to equilibrium (or colloquially, 'spin up') before experiments may be meaningfully performed. When the spin-up runs are finished, they can be utilized as 'restarts' for the subsequent experiments.

Modeling experiments carried out for this study utilized the base configuration from the PETM experiments of Ridgwell and Schmidt (2010) as an appropriate simulation of continental and ocean basin configuration for a late Paleocene to early Eocene world, and which features a baseline atmospheric CO_2 concentration equivalent to 3× pre-industrial level. I spun-up the model including an open-system carbon cycle – including volcanic CO_2 outgassing and allowing for fluvial input of weathering products and sedimentary carbonate burial – which ran for 500,000 years of simulation.

My first goal with cGENIE was to test whether I could generate long-term trends in carbon isotopes and temperature that match conditions from the late Paleocene to early

Eocene. I set up two parallel sets of experiments, along with a control run. In the control experiment, no perturbations were introduced, and the model was allowed to run from its spun-up state onward to check for any model drift. Since the carbon cycle had already reached equilibrium by this point, no changes in temperature or $\delta^{13}C$ were expected throughout the experiment duration. The first two experiments introduced perturbations in the CO_2 volcanic outgassing rate of 150% baseline CO_2 flux and 200% baseline CO_2 flux, respectively. The third experimental run was meant to simulate the effects of a severe reduction in sedimentary organic carbon burial, but since this configuration of cGENIE does not represent organic carbon burial, I attempted a simulation of the effect this should have on the carbon isotopic composition of the ocean's DIC pool by modifying the $\delta^{13}C$ signature of the model's volcanic CO_2 outgassing flux to the organic-like -22‰, in order to reflect an imbalance due to less preferential removal of carbon-12. The resultant modeled atmospheric CO_2 concentration and benthic DIC $\delta^{13}C$ are plotted as a time series in order to examine the evolution of these parameters over the course of the experiment runs.

2.3 – VOLCANIC OUTGASSING SCENARIO SIMULATIONS USING CGENIE

Next, in lieu of being able to realistically test the impact of changes in organic carbon burial, I tested further volcanic outgassing scenarios in cGENIE in order to reproduce an EECO-like warming event. I set up these experiments with the same configuration and spin-up methodology as described above. In order to model different volcanic CO_2 outgassing fluxes, I set this flux equal to 150%, 200% and 300% of the

baseline used in the base configuration, as well as a control run with unchanged volcanic CO_2 flux, and an additional experiment set with 75% of the baseline volcanic CO_2 flux, for comparative purposes.

Each experiment was run for 500,000 years. At the end of each experiment, I assessed spatial patterns in benthic $\delta^{13}C$, relative to the control experiment. In order to distinguish regional differences in the isotope signal from global changes, for each set of benthic $\delta^{13}C$ model results, I subtracted out the global average benthic isotopic value. This way, $\delta^{13}C$ anomalies relative to the global average value would stand out. For later analysis, I also examined the modeled global stream-function at the end of each experiment, as well as the time series evolution of benthic $\delta^{13}C$ across all experiments.

2.4 – MODEL-DATA COMPARISONS

Much of this study lies in the relationship between the cGENIE model results and the isotopic records compiled from the Cramer composite across EECO. I selected $\delta^{13}C$ and $\delta^{18}O$ data from three different time slices of the Cramer compilation, focusing on samples collected that date close to 50 Ma, 55 Ma, and 60 Ma, and allowing a deviation of no more than 500 kyr from these dates. These dates are significant in that they roughly outline the onset of EECO, its peak, and the start of climate recovery. This way, I compare model results against a variety of late Paleocene to early Eocene conditions. I also obtained paleo-locations for each of the sites with samples within these time slices, rotated using the Scotese paleomagnetic reconstruction. I then created an overlay in the cGENIE model results that highlights the benthic conditions at these paleo-locations and

extracts them as data points for analysis. Finally, I applied Equation 1 to the $\delta^{18}O$ values from my time slices of the Cramer composite data in order to obtain their representative paleo-temperatures.

I further created a series of scatter plots to compare the $\delta^{13}C$ and paleo-temperature as recorded at the various sites used in the compilation with their geographically-specified counterparts in each of the volcanic outgassing model experiments. I applied a linear regression to each pair of data in order to test goodness of fit.

2.5 – HIGH-RESOLUTION BENTHIC FORAMINIFERAL DATASET FOR ODP SITE 1258

The third major pillar of this study comes from the comparison of the high-resolution bulk carbonate isotopic dataset from ODP Site 1258, with a similarly high-resolution dataset from the same site generated from benthic foraminifera across EECO.

ODP Site 1258 is an equatorial Atlantic ODP drilling site located at 9°26.0'N 54°44.0'W, approximately 378 km off the northern coast of Suriname, South America on the Demerara Rise formation (Bice and Norris, 2005). It was drilled as part of ODP Leg 207, which had as one of its main goals the investigation of carbonate sedimentary facies during the early Cenozoic. As such, the cores have superb temporal resolution throughout much of the Eocene, which thus makes for an excellent opportunity to reconstruct climate and carbon cycle variability during this time period.

I utilized one primary species of benthic foraminifera found throughout the early Eocene at this site, *Nuttalides truempyi*. *N. truempyi* are typically identified by their prominent boss and angled sutures on their convex ventral side, as well as their tightly-spiraling chambers visible on their dorsal side (Figure 8). In samples that lacked a sufficient quantity of *N. truempyi* for analysis, I instead focused on the benthic species *Cibicidoides eoceanus*. The tests of this species are distinguished by their generally "snail shell-like" morphology and the loosely-spiraling chambers visible on their dorsal side (Figure 9).

All of the samples that I analyzed from ODP Site 1258 came from raw core segments stored at the IODP Bremen Core Repository. I processed samples from Holes A and B cores 7-11. All samples were dried, washed over a 63 micron mesh, and dried again and weighed for coarse fraction data before benthic foraminifera were picked from the coarse fraction. A large proportion of the 1258 samples had been stored at room temperature for years; in comparison to more recently requested samples from the Bremen core repository, these old samples were more difficult to wash using deionized water. These samples were instead soaked in a dilute solution of commercial water softener, containing active ingredients of zeolite and polycarboxylate. For isotopic analysis, I typically aimed for about 50 μg worth of carbonate in picked single-species foraminiferal tests for each sample. This typically meant picking between five and seven tests, depending on the size of the tests that I could identify, though I had success in obtaining isotopic data with as few as three tests on a few occasions. For picking benthic

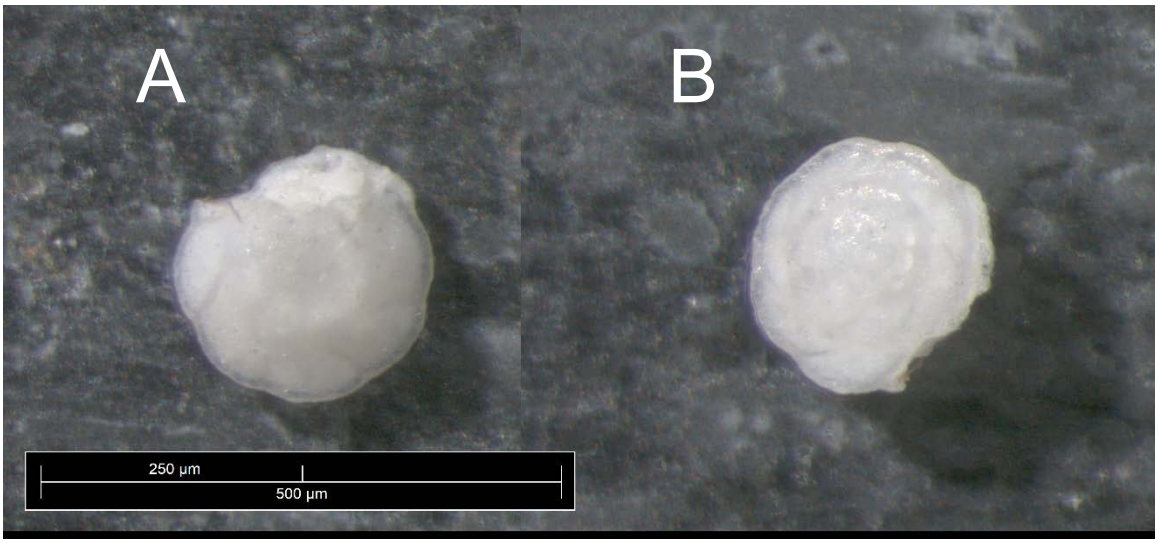

Figure 8: Microphotograph of *Nuttalides truempyi*. (A) shows the foraminifer's dorsal side, while (B) shows its ventral side. Some notable diagenetic calcite overgrowth is visible on the upper edge of the test's dorsal side.

Figure 9: Microphotograph of *Cibicidoides eoceanus*. (A) shows the foraminifer's dorsal side, while (B) shows its ventral side.

foraminifera, I used ordered sieves with mesh sizes of 250 μm, 212 μm, 180 μm, and 150 μm, separating out the portion of the sample into fractions of decreasing size. Portions of the sample that lay above the 250 μm size range were ignored, as this size fraction mainly contained chunks of sediment that remained intact after the washing procedure, as well as larger microfossils that were not the target of this study. Likewise, portions that lay below the 150 μm size range were also ignored, for being too small to visually identify and handle practically. Foraminifera test specimens that contained obvious diagenetic calcite overgrowth or inclusions that could not be easily cleaned with a steel needle were placed in a vial containing deionized water, and then sonicated using a Bransonic Ultrasonic Bath device for no more than five seconds. This method was typically avoided unless completely necessary to obtain a measurement for a given sample, as the device has the tendency to damage the test specimens if used to excess.

Analysis of the isotopic composition of foraminifera tests from each sample was completed utilizing a Thermo Fisher Kiel IV Carbonate Device and Delta V isotope ratio mass spectrometer. The Kiel IV carbonate device reacts introduced carbonates with a few droplets of phosphoric acid, generating carbon dioxide gas, along with a few other constituent gases such as water vapor. This gas is pumped through the Kiel's vacuum system through a series of traps, and frozen to -170°C using liquid nitrogen in order to isolate the carbon dioxide. This is then pumped into the Delta V mass spectrometer for analysis. The Delta V is a dual-inlet mass spectrometer, and as such it has an additional canister of a reference carbon dioxide gas of known isotopic composition, which is introduced into the mass spectrometer intermittently during a sample measurement,

allowing for greater precision in analysis than a continuous flow mass spectrometer. Standard lab procedures are followed during isotopic analysis, including the use of a calibration standard equivalent to NBS-19 (with $\delta^{13}C$ of 1.95‰ and $\delta^{18}O$ of -2.20‰), in order to track the mass spectrometer's precision and accuracy (Friedman et al., 1982).

Following acquisition, the raw $\delta^{13}C$ and $\delta^{18}O$ values were adjusted based on the accuracy of the measured standards. Measurement error was 0.04 for $\delta^{13}C$ and 0.08 for $\delta^{18}O$. Samples that utilized *Cibicidoides sp.* rather than *N. truempyi* were further adjusted using corrections from (Katz et al., 2003), and from there the data were organized stratigraphically and correlated to the radiometric Ar^{40} calibrated astronomical age model from Westerhold and Röhl (2009).

CHAPTER 3 – RESULTS

3.1 – QUANTITATIVE ANALYSIS OF CRAMER DATASET

Despite the steps taken to make the site-by-site decompositions of the Cramer dataset applicable to assess the relative timing of carbon and oxygen isotopic minima, records from several sites were unsuitable for further study. Several of the analyzed sites lacked the temporal resolution necessary to reasonably ascertain isotopic minima surrounding EECO. Other sites only had a small handful of datapoints within my target window, and could not capture EECO properly. Sites that held insufficient data include DSDP Site 98, DSDP Site 384, DSDP Site 525, DSDP Site 527, DSDP Site 528, DSDP Site 550, ODP Site 689, ODP Site 690, ODP Site 1051, and ODP Site 1209. Therefore, I

utilized site-by-site decompositions from the following sites for my signal asynchronicity analysis: DSDP Site 401, DSDP Site 577, ODP Site 698, ODP Site 702, ODP Site 738, ODP Site 865, and ODP Site 1258.

For each of these selected sites, I found that the $\delta^{13}C$ signal invariably led the $\delta^{18}O$ signal by at least several hundred thousand years (Figures 10-16). Mean asynchronicity between the two signals across all sites was ~1.5 Myr, with a standard deviation of ~0.7 Myr. The largest asynchronicity exists at ODP Site 702, in the southern Atlantic, where the $\delta^{13}C$ minimum leads the $\delta^{18}O$ minimum by ~2.5 Myr. Conversely, the smallest asynchronicity exists at ODP Site 865, in the tropical Pacific, where the separation between the signals was ~355 kyr. I found that the $\delta^{13}C$ signal tended to

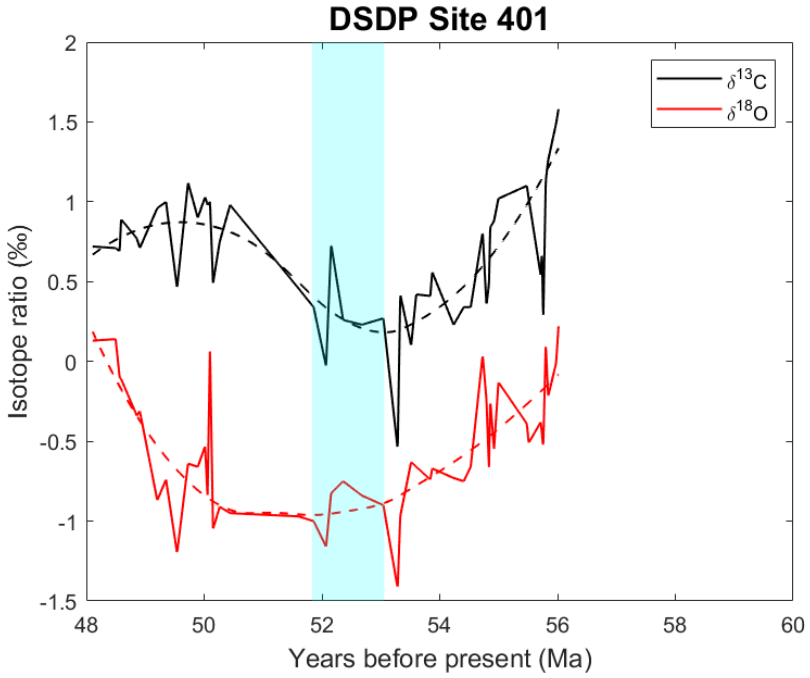

Figure 10: Benthic isotope signals from DSDP Site 401, as recorded in the Cramer dataset. Signal asynchronicity is highlighted in blue.

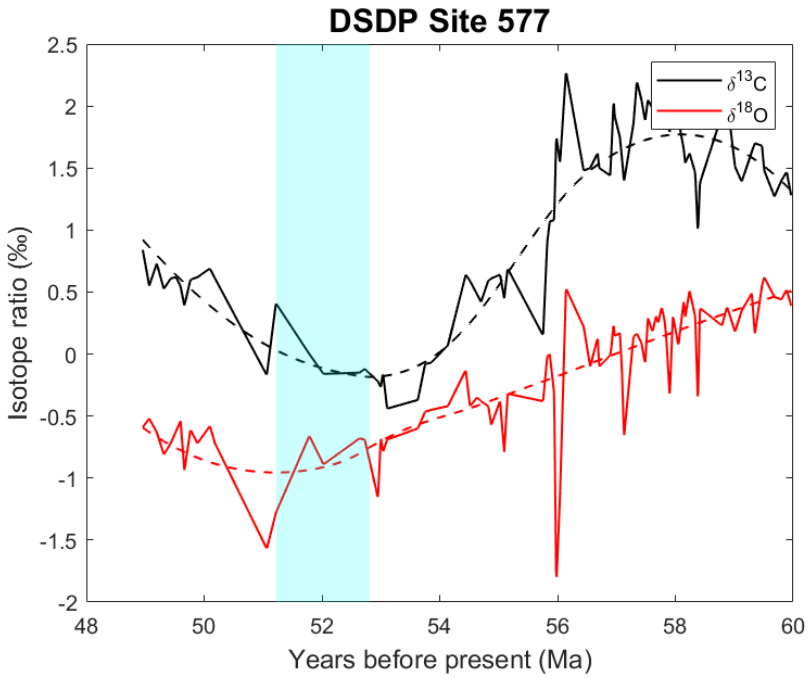

Figure 11: Benthic isotope signals from DSDP Site 577, as recorded in the Cramer dataset. Signal asynchronicity is highlighted in blue.

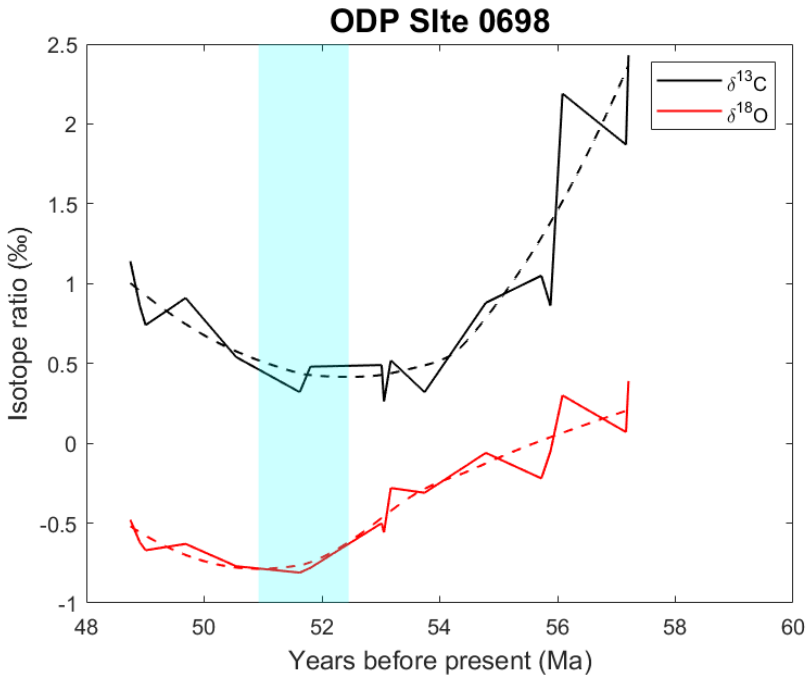

Figure 12: Benthic isotope signals from ODP Site 698, as recorded in the Cramer dataset. Signal asynchronicity is highlighted in blue.

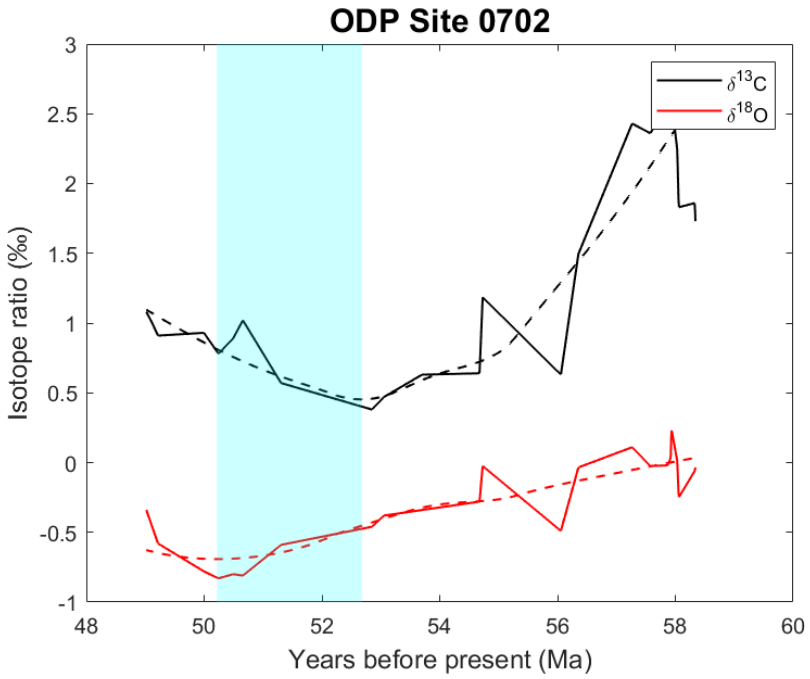

Figure 13: Benthic isotope signals from ODP Site 702, as recorded in the Cramer dataset. Signal asynchronicity is highlighted in blue.

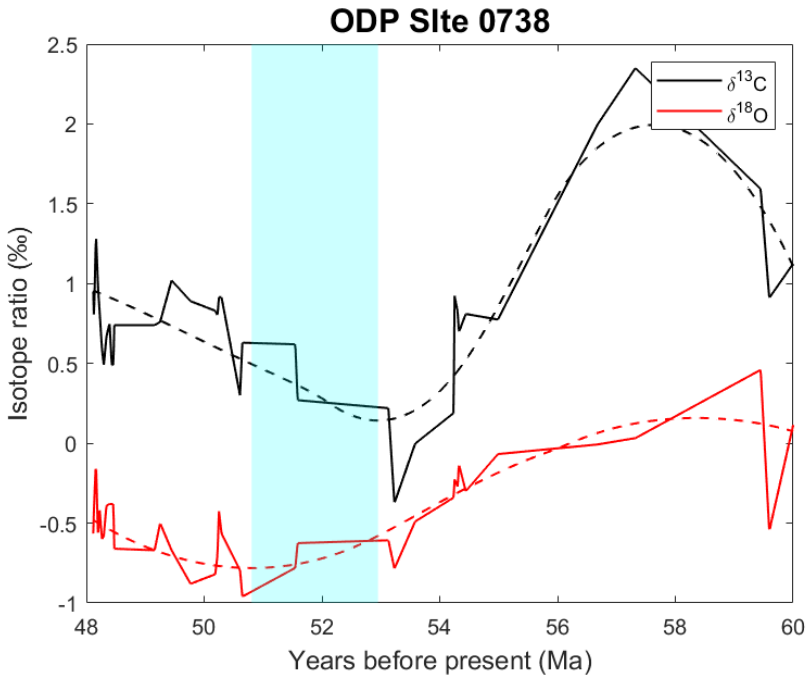

Figure 14: Benthic isotope signals from ODP Site 738, as recorded in the Cramer dataset. Signal asynchronicity is highlighted in blue.

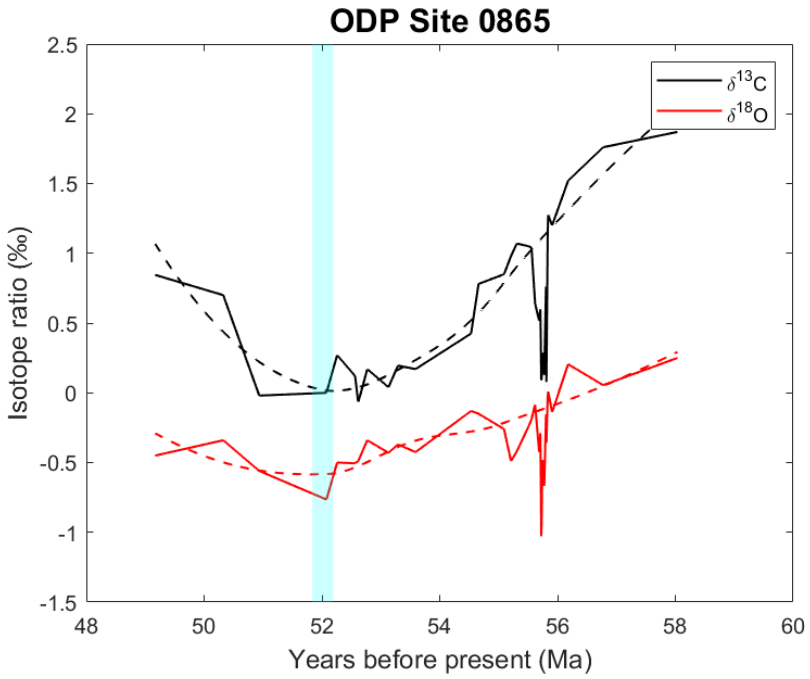

Figure 15: Benthic isotope signals from ODP Site 865, as recorded in the Cramer dataset. Signal asynchronicity is highlighted in blue.

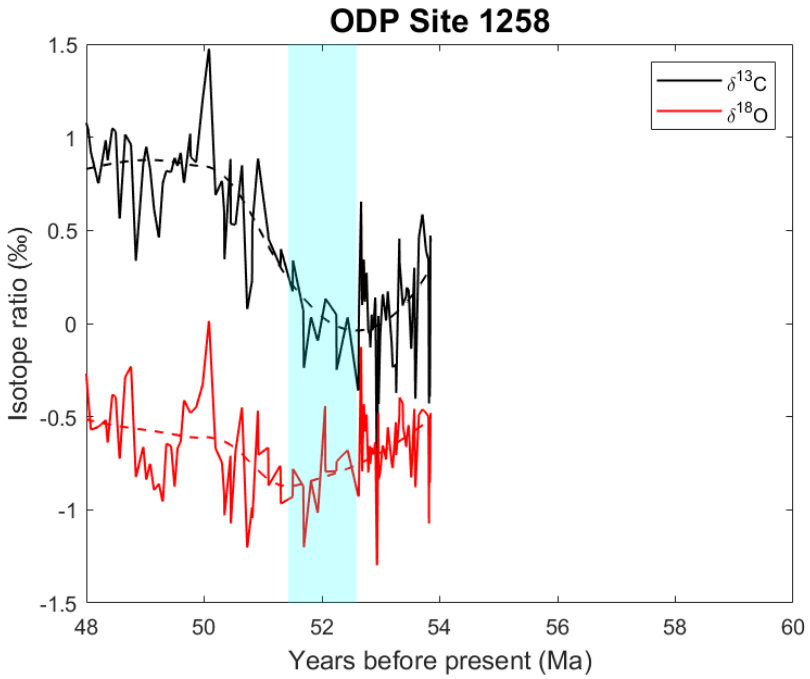

Figure 16: Benthic isotope signals from ODP Site 1258, as recorded in the Cramer dataset. Signal asynchronicity is highlighted in blue.

persistently reach its peak around 52.5 Myr, while the occurrence of the $\delta^{18}O$ peak tended to vary with the sample's location.

In evaluating the correlation between the size of the sites' signal asynchronicity and their paleo-distance from the equator, I found that a linear regression yielded a coefficient of determination of 0.5176 (Figure 17). This indicates a positive correlation between the sizes of the signal asynchronicity and the sites' absolute value paleo-latitude. Other parameters evaluated in comparison to signal asynchronicity magnitude yielded no discernable patterns.

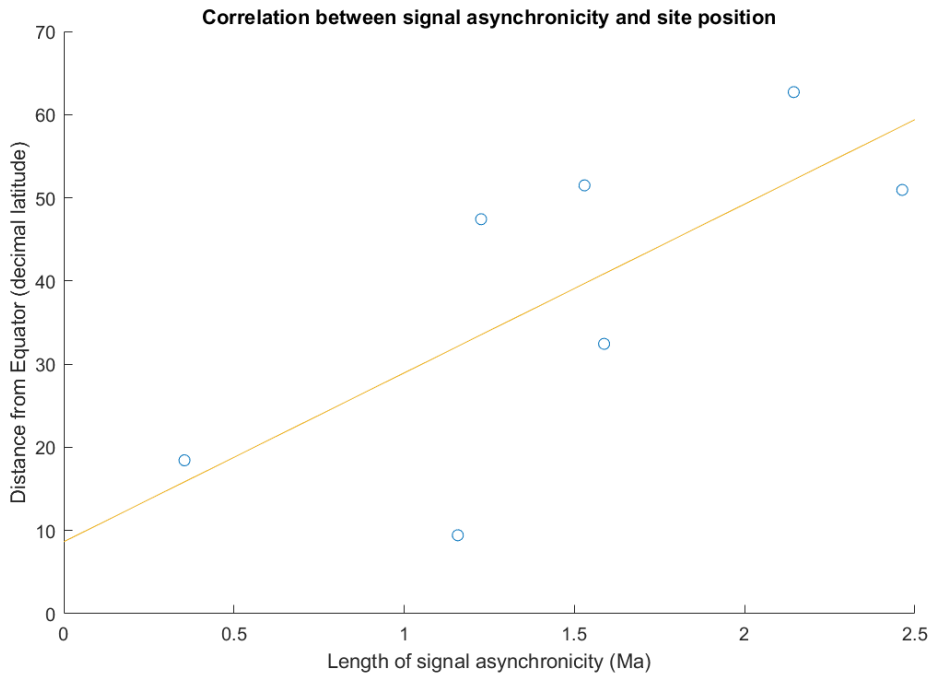

Figure 17: Correlation between site's magnitude of benthic isotopic signal asynchronicity and site's geographic distance from the equator. The linear regression is plotted in yellow.

3.2 – CGENIE MODELING EXPERIMENTS

The first set of cGENIE experiments implemented enhanced volcanic outgassing or altered the isotopic composition of the volcanic outgassing CO_2 flux (Figures 18-19). Time-series of atmospheric CO_2 and benthic DIC $\delta^{13}C$ across the experiment duration show that the various enhancements to volcanic outgassing flux led to large increases in atmospheric CO_2 concentration, with each experiment starting with a concentration of 834 ppm, and the enhanced volcanic outgassing experiments ending at much higher (1940 ppm with 150% outgassing, and 3380 ppm with the 200% outgassing) but given the relatively isotopically heavy composition of volcanic CO_2 (specified as -6‰ to approximate the average mantle value), the $\delta^{13}C$ composition of benthic DIC displayed less significant changes by the conclusion of the experiments, starting from a composition of 1.063‰ and changing only to 0.219‰ in the 150% outgassing scenario, and -0.452‰ in the 200% outgassing scenario (Figure 18). Inversely, altering only the $\delta^{13}C$ of the volcanic CO_2 outgassing flux had very little impact on the amount of CO_2 in the atmosphere (not changing CO_2 concentration at all from its starting value of 840 ppm), but had a profound effect on global benthic DIC $\delta^{13}C$, bringing the starting composition of 1.063‰ down to -6.881‰ (Figure 19).

The volcanic outgassing experiments testing a larger range of flux adjustments warrant a more detailed examination of the results. I opt here to assess each experiment separately. First, the spatial distributions of DIC $\delta^{13}C$ for each experiment, including the control, were plotted utilizing the Muffinplot suite of MATLAB functions acquired from www.seao2.info/mycgenie.html (Figures 20-24). Plots were made for a vertical depth 'k'

value of 5, corresponding to an ocean depth averaged on ~2,300 meters, in order to best match the reconstructed paleodepth of most data in the Cramer composite. Next, in order to ascertain the effects of altered volcanic outgassing on benthic DIC $\delta^{13}C$, I generated comparative plots that examine the difference between the various altered outgassing experiments and the control experiment (Figures 25-28). These plots were also made for a 'k' value of 5. In order to examine the spatial $\delta^{13}C$ differences in these plots, I offset the plotted $\delta^{13}C$ values by the difference in mean global benthic DIC $\delta^{13}C$ between the completed control experiment and the adjusted volcanic outgassing experiment. This has the effect of highlighting ocean regions with higher or lower relative $\delta^{13}C$.

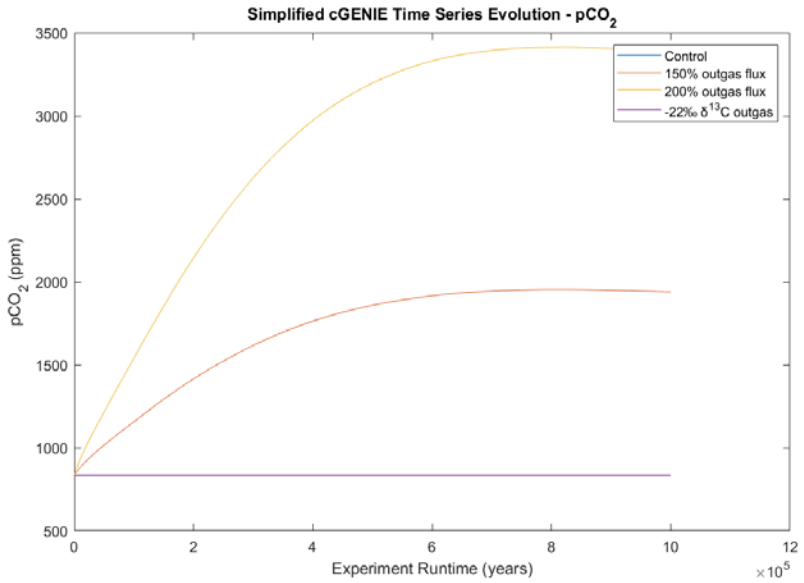

Figure 18: Time series evolution of global average atmospheric CO_2 concentrations throughout the simplified set of cGENIE experiments. It should be noted that the control experiment and -22‰ $\delta^{13}C$ outgas experiment results overlap each other completely.

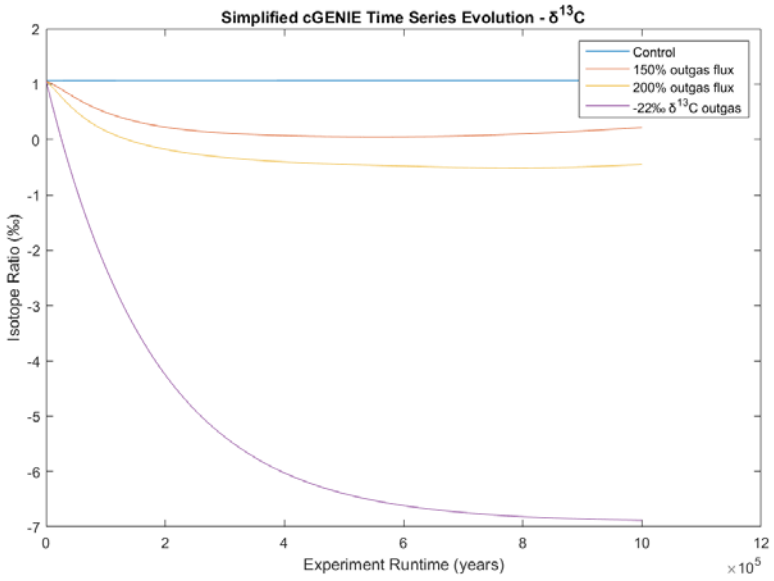

Figure 19: Time series evolution of global average benthic-level $\delta^{13}C$ throughout the simplified set of cGENIE experiments.

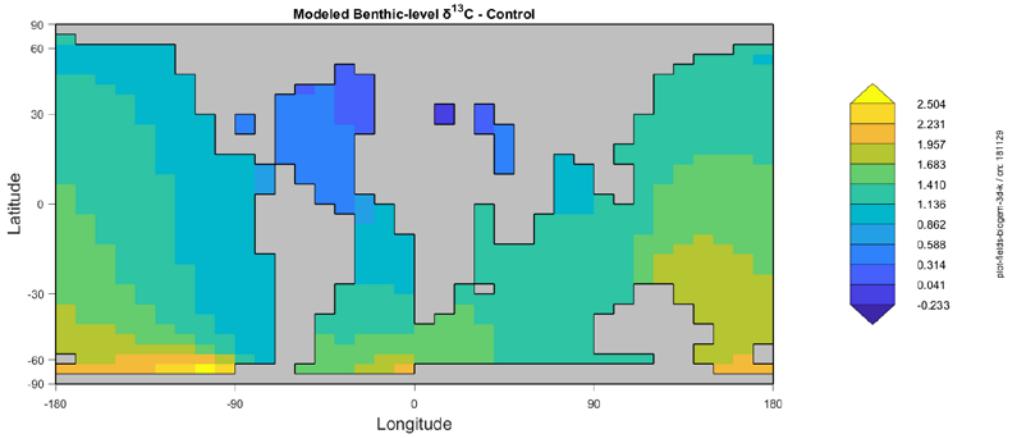

Figure 20: Spatial distribution of modeled benthic-level $\delta^{13}C$, with control experiment parameters.

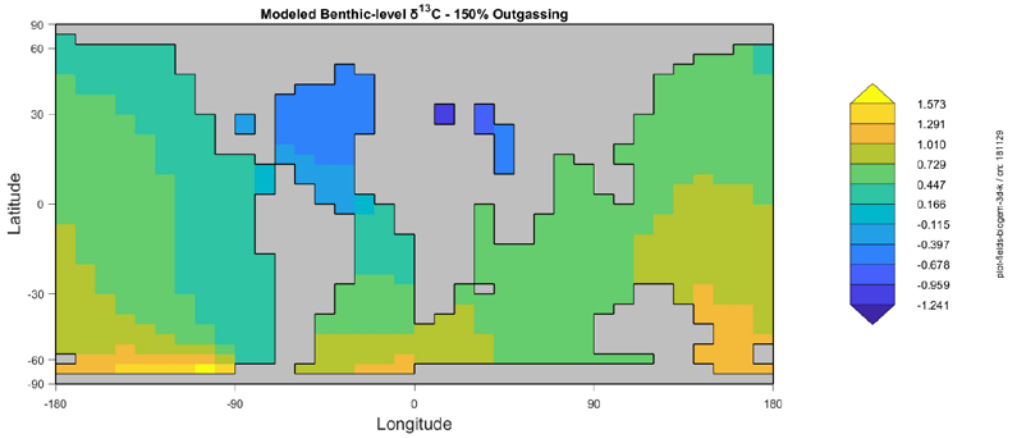

Figure 21: Spatial distribution of modeled benthic-level $\delta^{13}C$, with 150% volcanic outgassing volume experiment parameters.

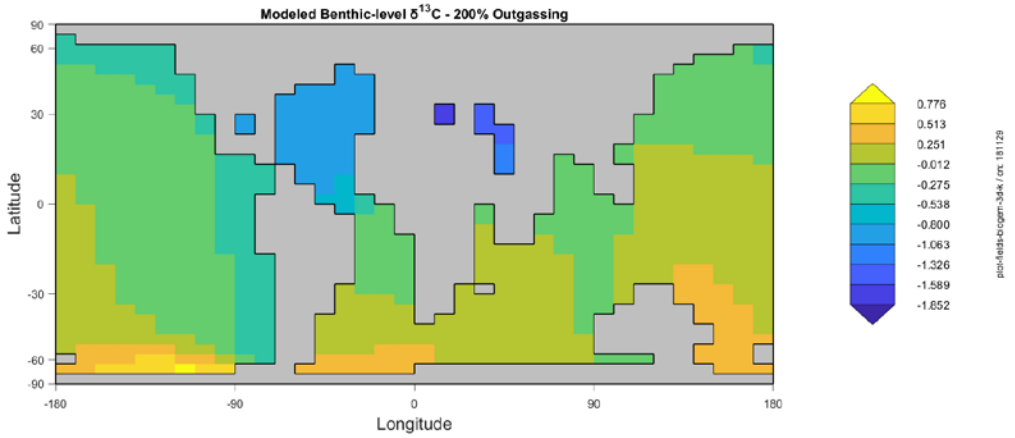

Figure 22: Spatial distribution of modeled benthic-level $\delta^{13}C$, with 200% volcanic outgassing volume experiment parameters.

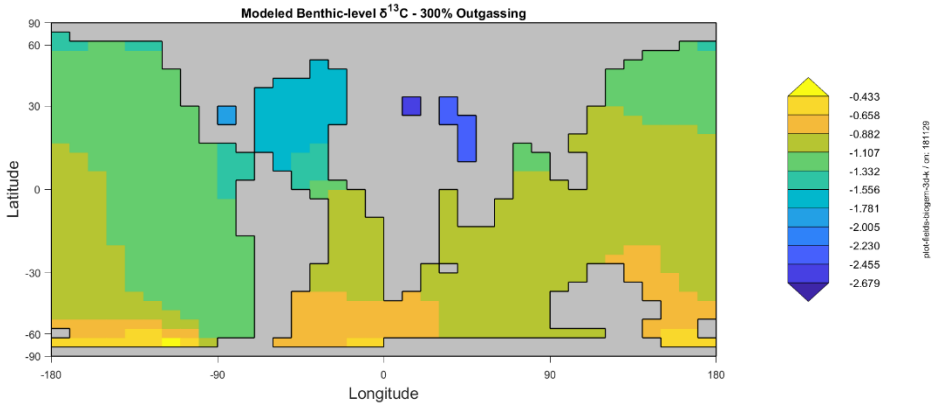

Figure 23: Spatial distribution of modeled benthic-level $\delta^{13}C$, with 300% volcanic outgassing volume experiment parameters.

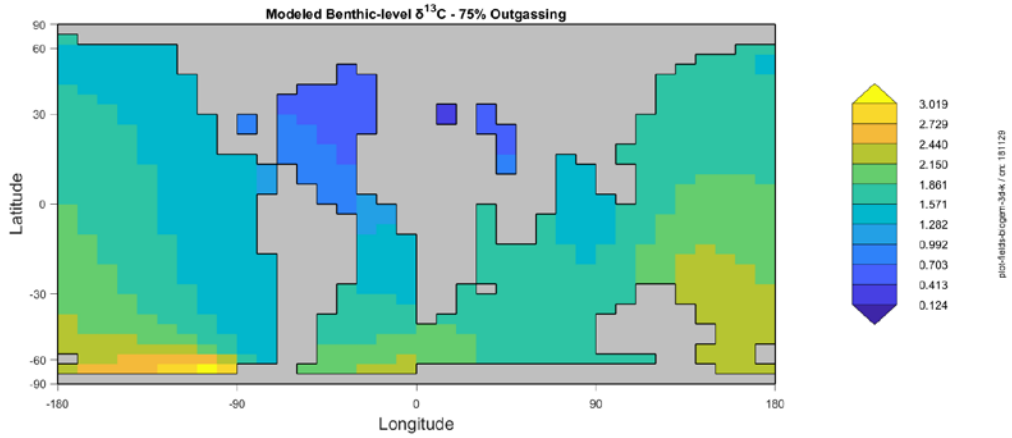

Figure 24: Spatial distribution of modeled benthic-level $\delta^{13}C$, with 75% volcanic outgassing volume experiment parameters.

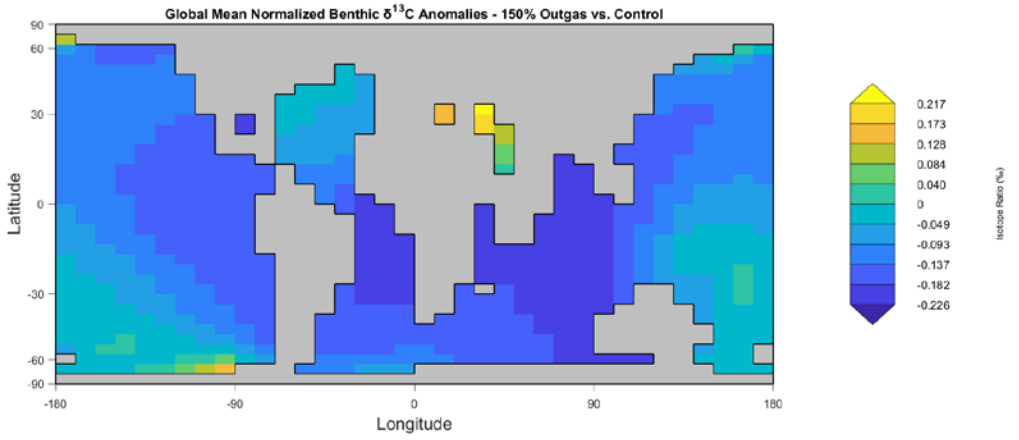

Figure 25: Spatial distribution of modeled benthic-level global $\delta^{13}C$ anomalies to control experiment values, normalized to mean global shift in isotope values, with 150% volcanic outgassing volume experiment parameters.

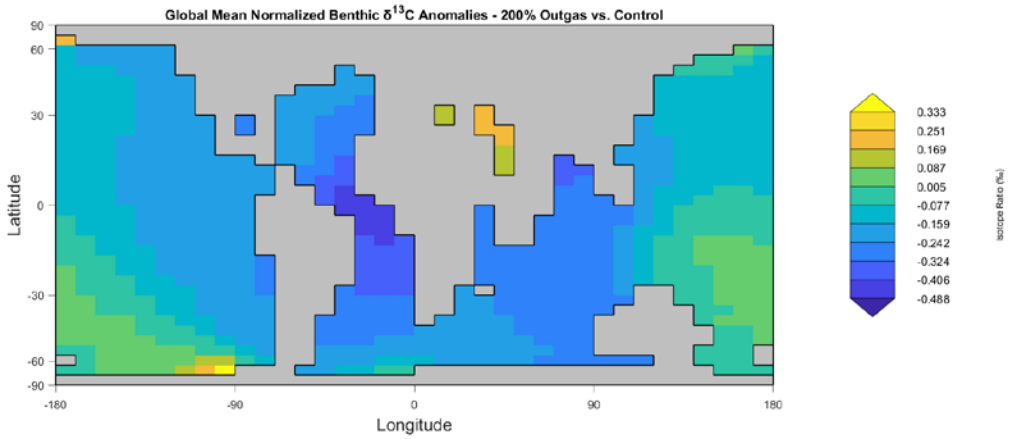

Figure 26: Spatial distribution of modeled benthic-level global $\delta^{13}C$ anomalies to control experiment values, normalized to mean global shift in isotope values, with 200% volcanic outgassing volume experiment parameters.

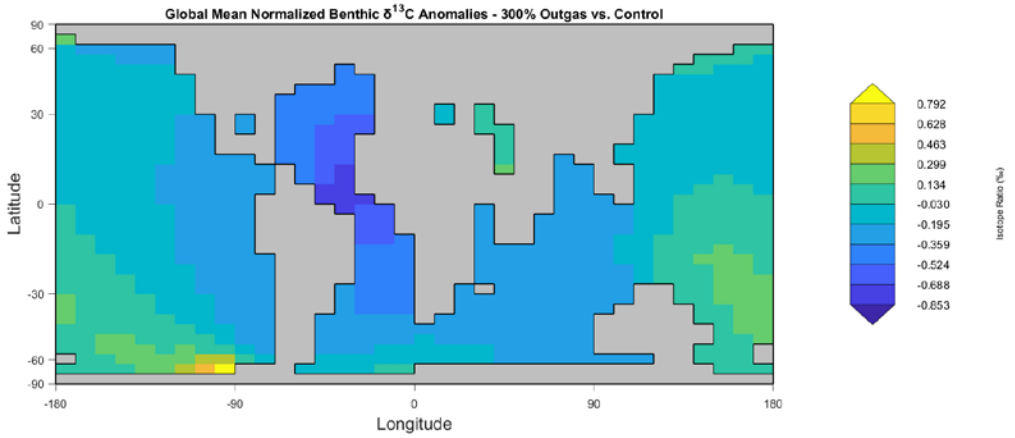

Figure 27: Spatial distribution of modeled benthic-level global $\delta^{13}C$ anomalies to control experiment values, normalized to mean global shift in isotope values, with 300% volcanic outgassing volume experiment parameters.

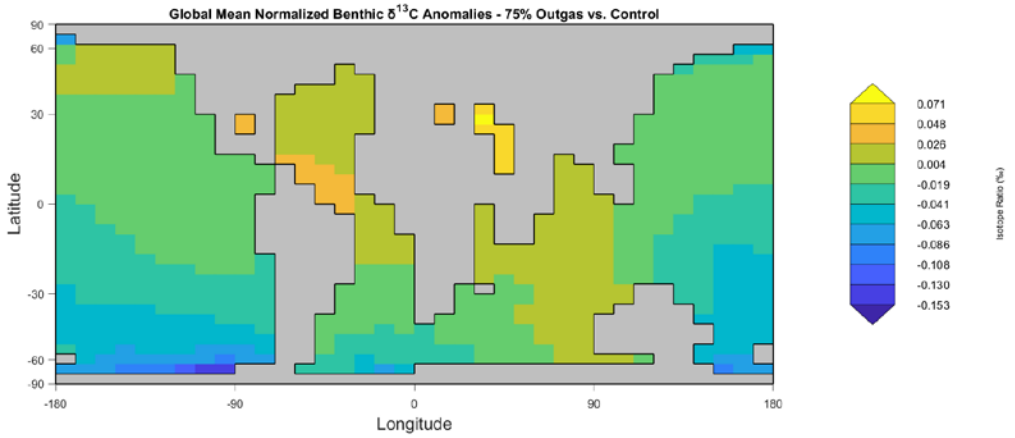

Figure 28: Spatial distribution of modeled benthic-level global $\delta^{13}C$ anomalies to control experiment values, normalized to mean global shift in isotope values, with 75% volcanic outgassing volume experiment parameters.

To summarize, experiments with higher volcanic outgassing flux lead to deep ocean DIC becoming notably lighter in ^{13}C in lower latitudes. Regarding the 150% outgassing flux experiment – in which the offset of mean benthic DIC $\delta^{13}C$ to the control was -0.847‰ – the lowest $\delta^{13}C$ anomaly reaches -0.226‰ over the mean concentration, in the eastern North Atlantic in ocean grid cells adjacent to continent (Figure 25). Other regions of the deep ocean become relatively heavier in $\delta^{13}C$, such as the western Southern Ocean and the northwestern Pacific, and reach a positive $\delta^{13}C$ anomaly of 0.217‰. The 200% outgassing flux experiment had a mean benthic DIC $\delta^{13}C$ offset of -1.518‰ to the control, and the comparison plot shows the decreased $\delta^{13}C$ anomaly migrating more tightly towards the equatorial Atlantic (Figure 26). The negative anomaly also increases in intensity as well, reaching a peak of -0.488‰ below the mean. Other regions that were enriched in ^{13}C in the 150% outgassing volume experiment, such as the Tethys Sea and the southern Atlantic, move up closer to the mean global $\delta^{13}C$. The few regions that showed notable relative $\delta^{13}C$ enrichment in the 150% outgassing experiment continue to do so here as well, with the positive $\delta^{13}C$ anomaly in the Southern Ocean and the northwestern Pacific reaching 0.333‰. The 300% outgassing volume experiment, with an experiment-control global mean benthic $\delta^{13}C$ offset of -2.535‰, shows this effect to an even further exaggerated extent (Figure 27). The zone of relative $\delta^{13}C$ depletion becomes even more greatly confined to the equatorial Atlantic, and the minimum negative $\delta^{13}C$ anomaly in this region lowers to -0.853‰. Notably, the higher-$\delta^{13}C$ region in the Southern Ocean grows even more enriched, reaching a positive relative $\delta^{13}C$ anomaly of 0.792‰. The similar enriched zone in the northwestern Pacific does not

follow suit, however, instead only increasing to about 0.265‰ relative to the global mean benthic $\delta^{13}C$. The hypothetical 75% outgassing scenario – which has an experiment-control mean global $\delta^{13}C$ offset of 0.383‰ - shows patterns that appear similar to the other experiments, but in inverse (Figure 28). The equatorial Atlantic becomes higher in $\delta^{13}C$ relative to the mean, to a maximum anomaly of approximately 0.0483‰, while the western Southern Ocean becomes instead depleted to a minimum $\delta^{13}C$ anomaly of -0.153‰.

I also examined zonally-averaged vertical $\delta^{13}C$ profiles for each experiment. Once again, this utilized the Muffinplot MATLAB functions (Figures 29-33). Plots were generated with a 'k' value set to 0, for a zonal mean vertical slice through the ocean. A global streamfunction overlay was also added in order to compare respective $\delta^{13}C$ shifts in the profile to shifts in overturning circulation. The experimental $\delta^{13}C$ values in these

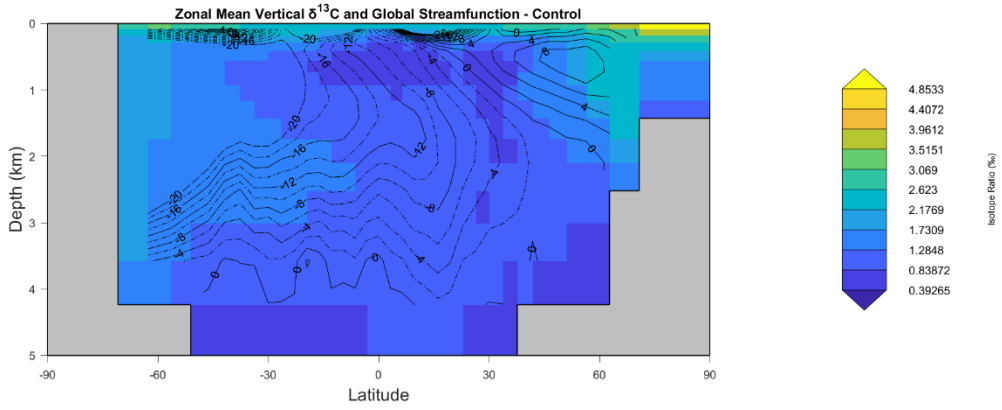

Figure 29: Vertical distribution of modeled DIC $\delta^{13}C$ through the zonal mean, with global streamfunction contours, using control experiment parameters.

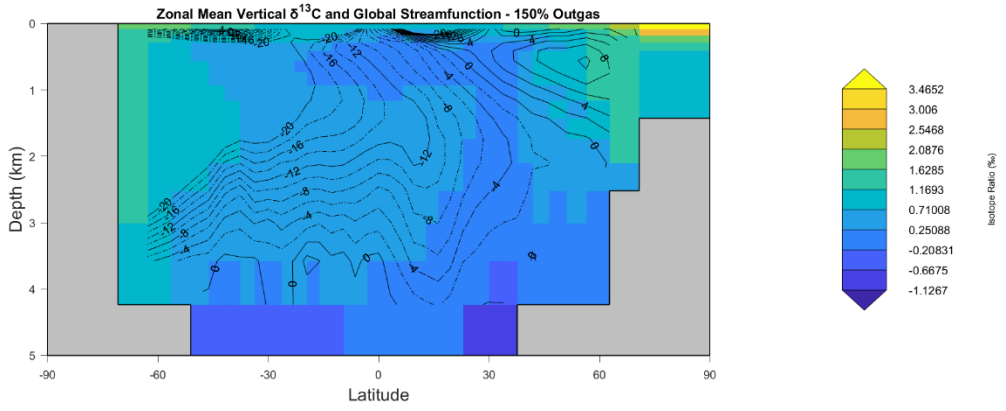

Figure 30: Vertical distribution of modeled DIC $\delta^{13}C$ through the zonal mean, with global streamfunction contours, using 150% volcanic outgassing flux.

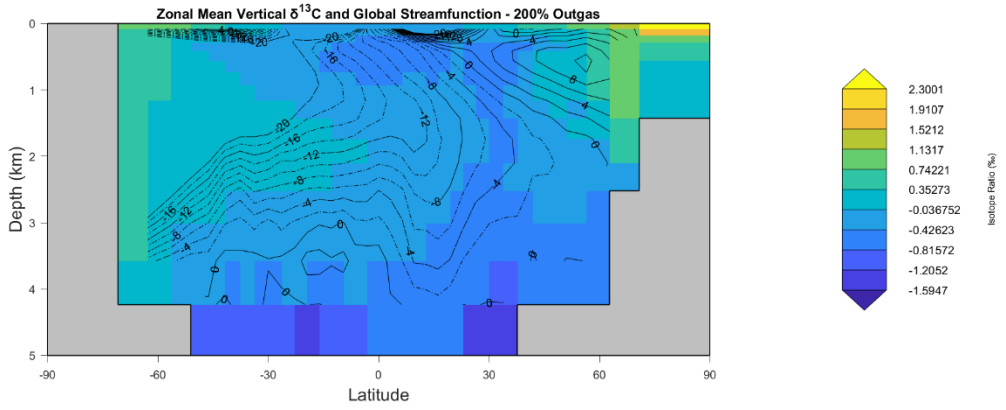

Figure 31: Vertical distribution of modeled DIC $\delta^{13}C$ through the zonal mean, with global streamfunction contours, using 200% volcanic outgassing flux.

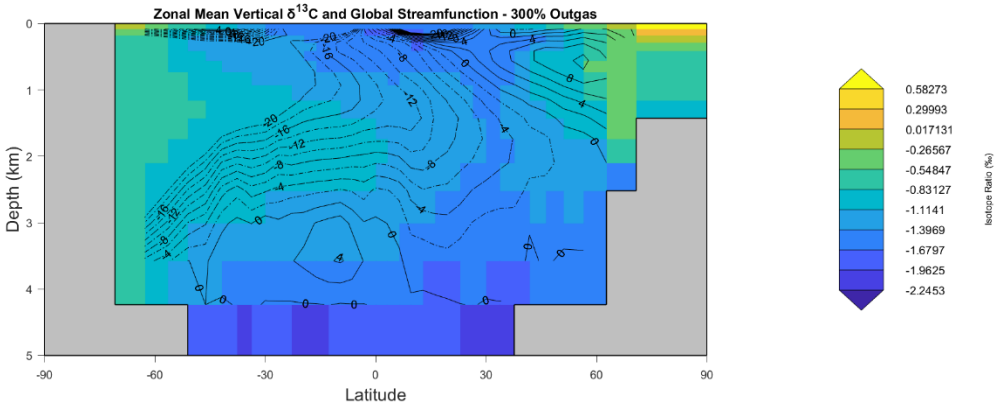

Figure 32: Vertical distribution of modeled DIC $\delta^{13}C$ through the zonal mean, with global streamfunction contours, using 300% volcanic outgassing flux.

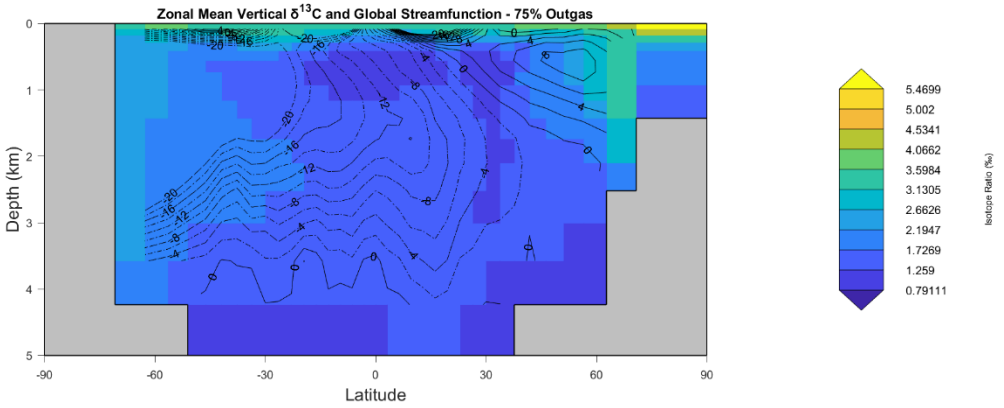

Figure 33: Vertical distribution of modeled DIC $\delta^{13}C$ through the zonal mean, with global streamfunction contours, using 75% volcanic outgassing flux.

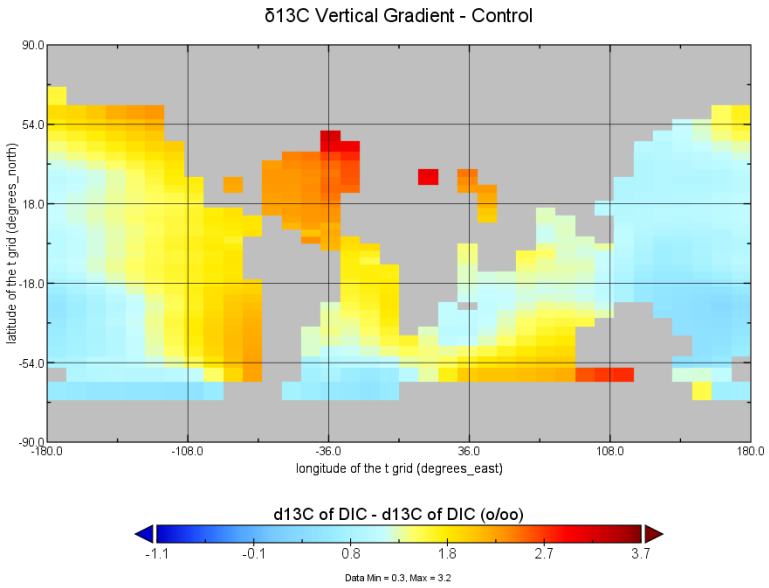

Figure 34: Spatial distributions of modeled vertical surface-benthic $\delta^{13}C$ gradient, with control experiment parameters.

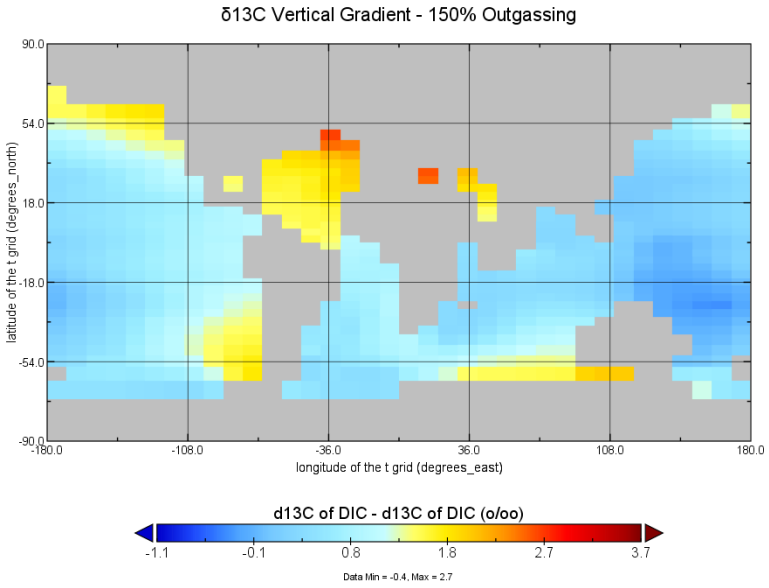

Figure 35: Spatial distributions of modeled vertical surface-benthic $\delta^{13}C$ gradient, with 150% volcanic outgassing flux.

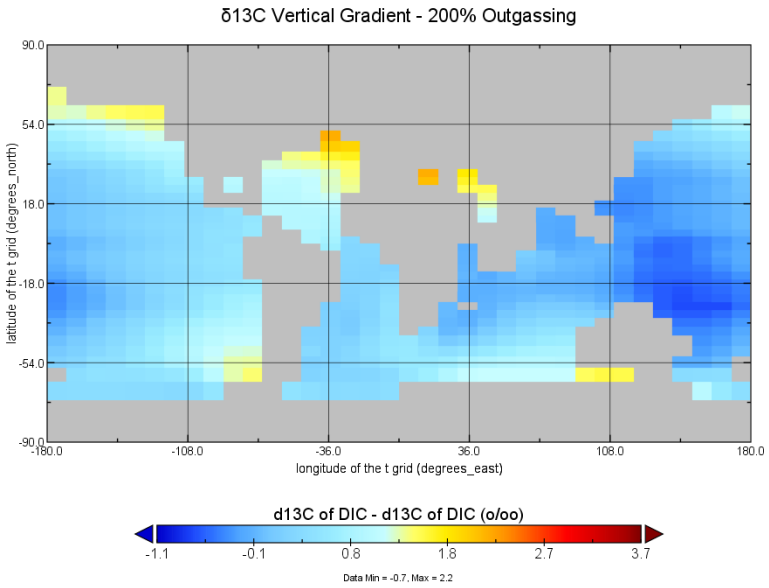

Figure 36: Spatial distributions of modeled vertical surface-benthic $\delta^{13}C$ gradient, with 200% volcanic outgassing flux.

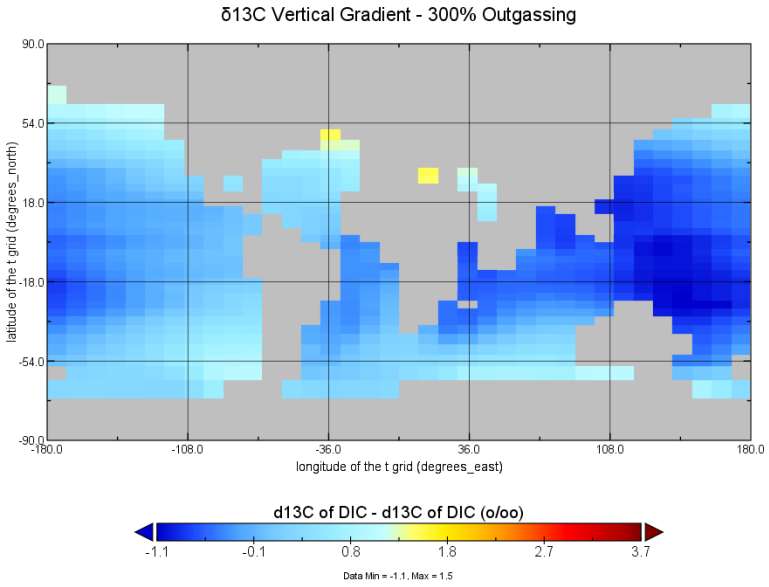

Figure 37: Spatial distributions of modeled vertical surface-benthic $\delta^{13}C$ gradient, with 300% volcanic outgassing flux.

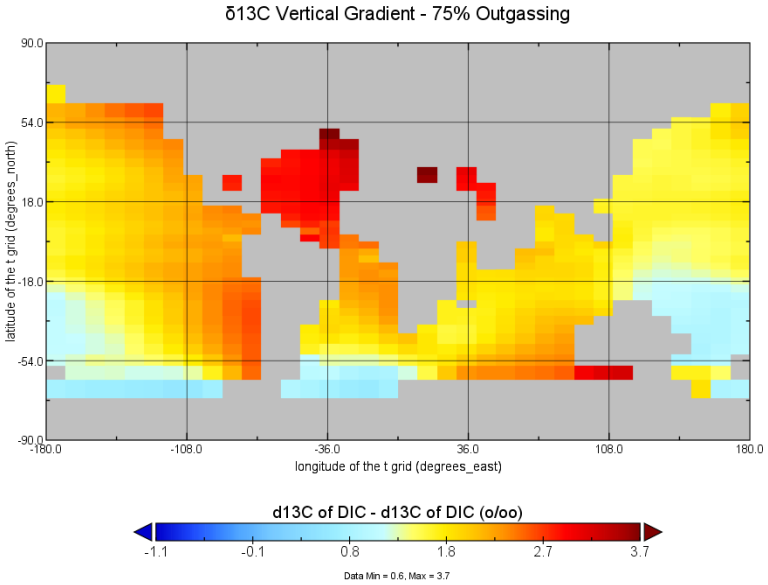

Figure 38: Spatial distributions of modeled vertical surface-benthic $\delta^{13}C$ gradient, with 75% volcanic outgassing flux.

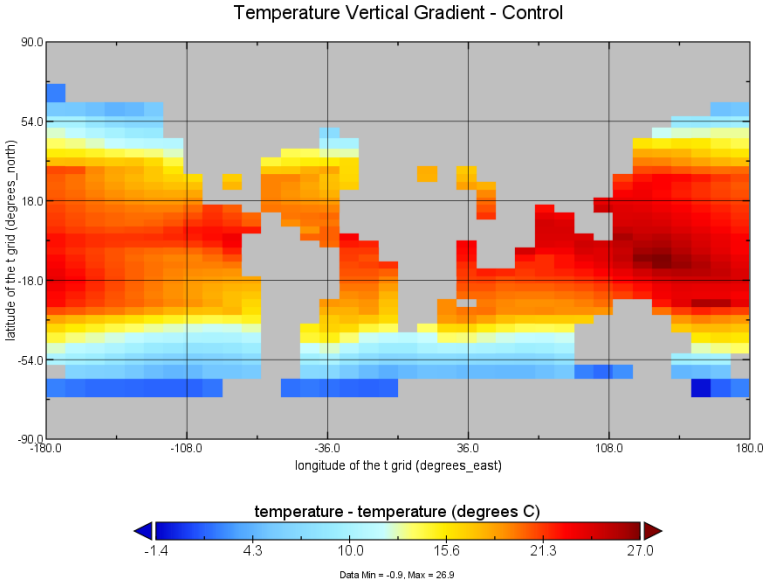

Figure 39: Spatial distributions of modeled vertical surface-benthic temperature gradient, with control experiment parameters.

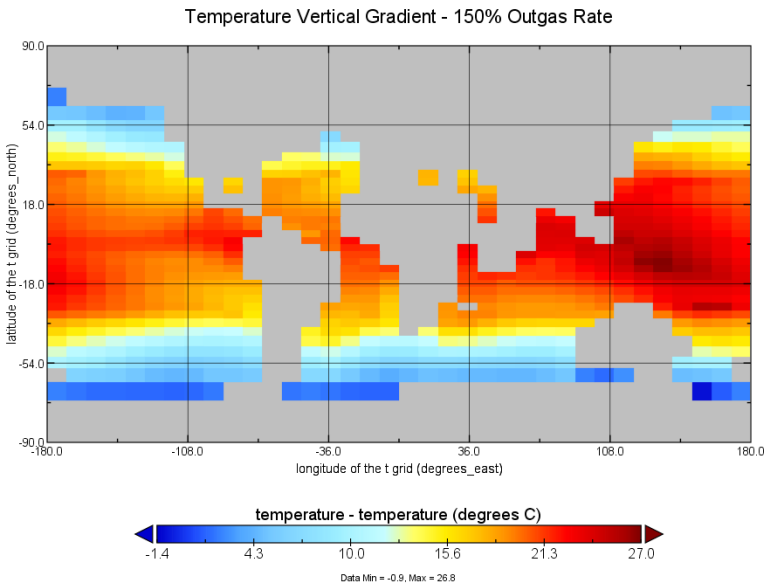

Figure 40: Spatial distributions of modeled vertical surface-benthic temperature gradient, with 150% volcanic outgassing flux.

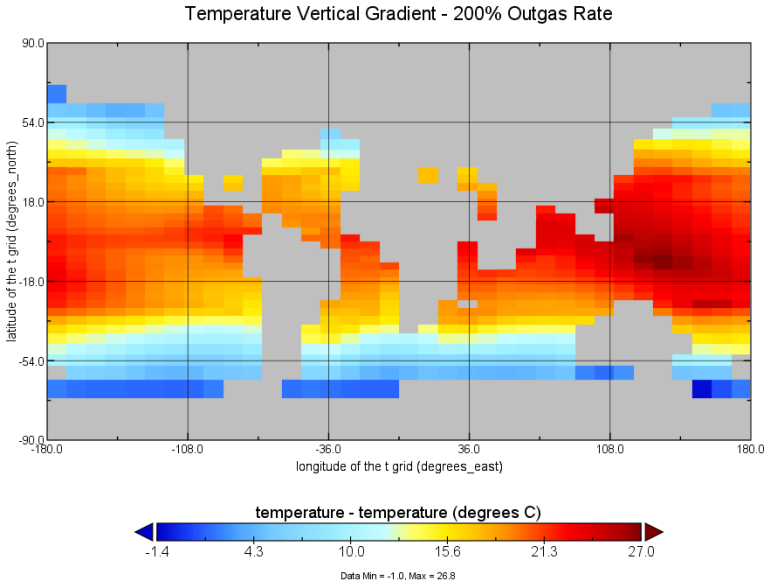

Figure 41: Spatial distributions of modeled vertical surface-benthic temperature gradient, with 200% volcanic outgassing flux.

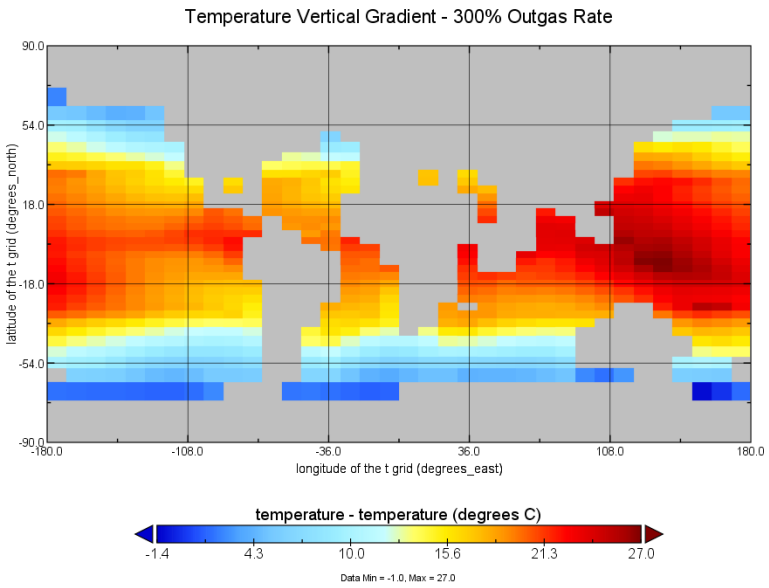

Figure 42: Spatial distributions of modeled vertical surface-benthic temperature gradient, with 300% volcanic outgassing flux.

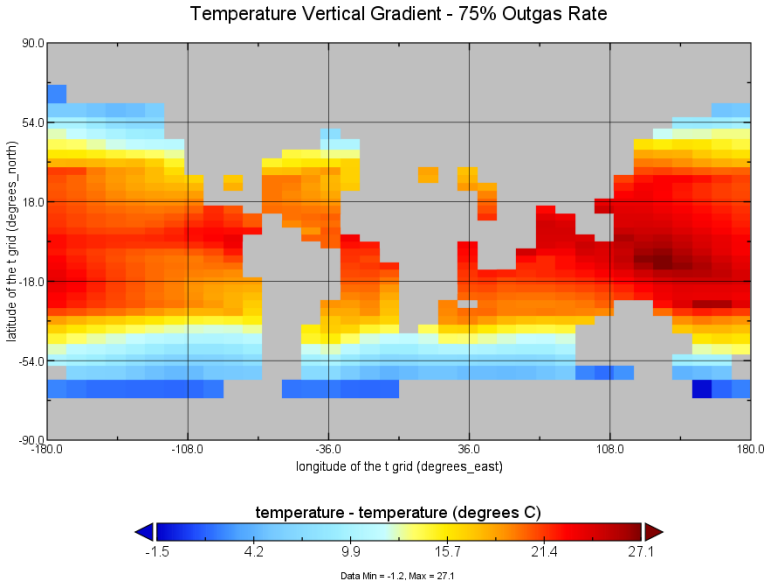

Figure 43: Spatial distributions of modeled vertical surface-benthic temperature gradient, with 75% volcanic outgassing flux.

profiles are not offset to the global mean difference from the control experiment. To summarize the findings, in experiments with increased volcanic outgassing, $\delta^{13}C$-enriched regions begin to form below the surface in the northern high-latitude areas of the ocean, to a depth of about 2 km, and in the southern high-latitude areas, to a depth of up to 4 km (Figures 29-32). The southern tongue of high-$\delta^{13}C$ water, concentrated mainly at a depth of 2 km, extends across latitudes as far as the equator, while the northern region instead remains confined to the latitude from which it originates. The global streamfunction contours generally reflect this well, as a +4 Sverdrup contour begins to form in the deep equatorial ocean with higher volcanic outgassing rates, along with a +12 Sverdrup contour in the subsurface northern high-latitude ocean. In the 75% outgassing rate experiment (Figure 33), we see the opposite effects taking place, as the region of $\delta^{13}C$ enriched waters in the southern high-latitude ocean diminishes in size, and global streamfunction contours also reflect dwindling flows throughout the deep ocean.

Finally, I examined the surface-to-benthic $\delta^{13}C$ and temperature gradient spatially for each experiment (Figures 34-43). Here I utilized the NASA/GISS Panoply data viewing software. For all experiments, ocean regions with a steep vertical $\delta^{13}C$ gradient (i.e. the surface-level $\delta^{13}C$ is considerably higher than the benthic-level $\delta^{13}C$) include the northern Atlantic, as well as the southern Pacific, specifically in proximity to the western coastline. Other ocean regions have a shallower vertical $\delta^{13}C$ gradient. My experiment results demonstrate that the global surface-benthic $\delta^{13}C$ gradient decreases in scenarios with enhanced volcanic outgassing; in the control experiment, the global mean gradient is 1.4‰, while in the 150% outgassing flux scenario this decreases to 0.7‰, in the 200%

outgassing flux scenario it is 0.3‰, and in the 300% outgassing flux scenario it is further reduced (Figures 34-37). In our hypothetical reduced volcanic outgas volume experiment, the global mean gradient increases to a 1.9‰ difference in $\delta^{13}C$ between the surface and benthic levels (Figure 38). Alterations to volcanic outgassing flux appear to have very little effect on the surface-deep ocean temperature gradient, with the only visible changes appearing in the equatorial Atlantic, in the form of a reduction in the gradient equivalent to a few fractions of a degree Celsius in the scenarios of increased outgassing flux (Figures 39-43)

3.3 – MODEL-DATA OVERLAY AND ISOTOPIC VALUE COMPARISONS

Overlaying the isotopic values from the various sites in the Cramer composite onto the equivalent model sites provides one way of evaluating the likelihood of the various modeled volcanic outgassing scenarios. Using cross-plots, I compared the isotope data from the Cramer composite to the equivalent modeled values at corresponding positions and depths, utilizing values from the control experiment, the 150% outgassing flux and 200% outgassing flux experiments. These plots compare data from the Cramer composite averaged at 50 Ma, 55 Ma, and 60 Ma time to both modeled/measured $\delta^{13}C$ and modeled/calculated temperatures. I then calculated linear regressions and coefficients of determination for each plot.

In the comparisons of modeled ocean temperatures to temperature calculated from $\delta^{18}O$, I found that none of the completed model experiments captured the same range of temperatures across the ocean (Figures 44-52). In the 50 Ma time slice, published global

temperatures vary between about 10.5 to 14 °C (a range of 3.5 °C) (Figures 44-46). The 55 Ma time slice of published temperatures similarly shows a range between about 10 to 12.5 °C (2.5°C) (Figures 47-49). Modeled deep ocean temperatures at the conclusion of the control experiment stay around 10.3 °C, with a minimum of 10.26 °C and a maximum of 10.44 °C (a range of 0.18°C), while the 150% outgas volume experiment shows deep ocean temperatures staying closely around 14 °C, with a minimum of 13.8 °C and a maximum of 14.1 °C (a range of 0.3°C) (Figures 44-45, Figures 47-48, Figures 50-51). Both the 60 Ma time slice and the 200% outgas experiments show different patterns. In the 60 Ma time slice, published temperatures are quite notably lower than they are in later time slices, ranging between 4.9 and 8.4 °C (a range of 3.5°C) (Figures 50-52). In the 200% outgas experiments, modeled temperatures are higher and vary slightly more than

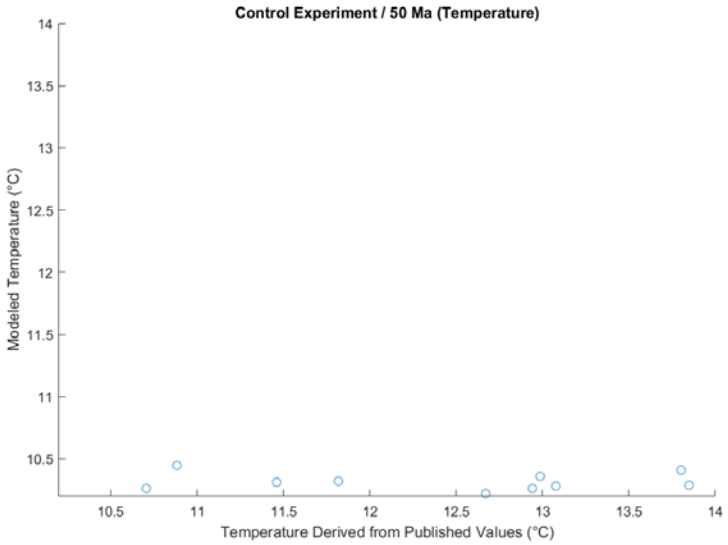

Figure 44: Comparison of temperature values between control model experiment and 50 Ma time slice of published data in the Cramer composite.

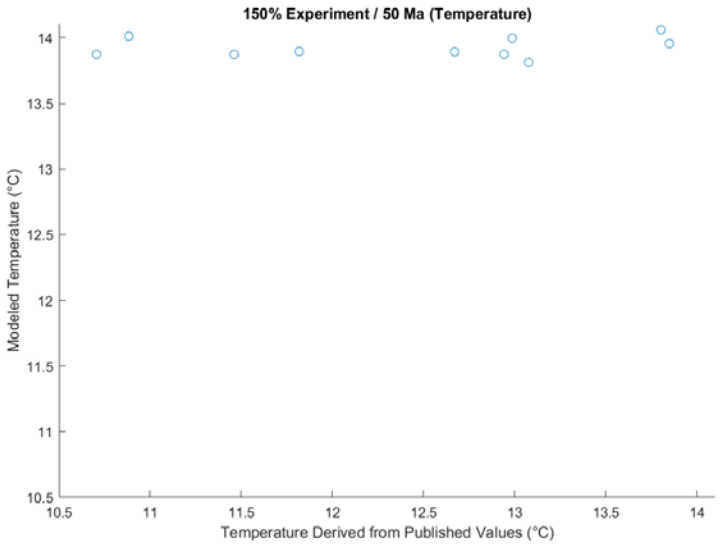

Figure 45: Comparison of temperature values between 150% volcanic outgassing flux experiment and 50 Ma time slice of published data in the Cramer composite.

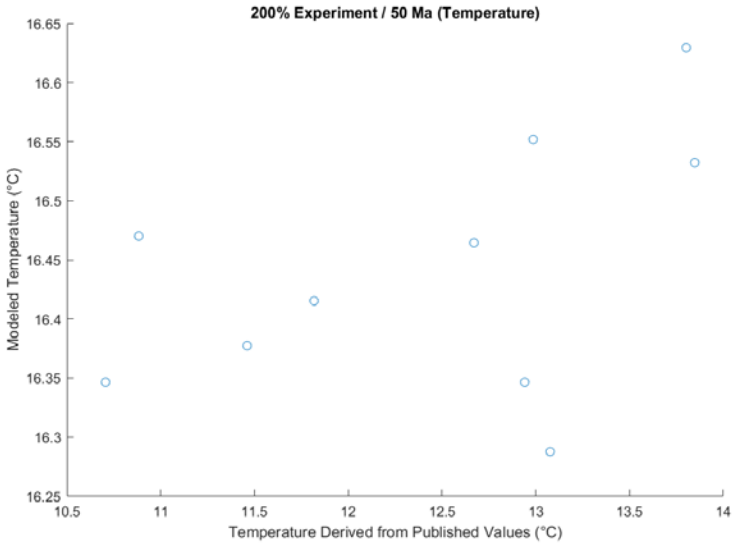

Figure 46: Comparison of temperature values between 200% volcanic outgassing flux experiment and 50 Ma time slice of published data in the Cramer composite.

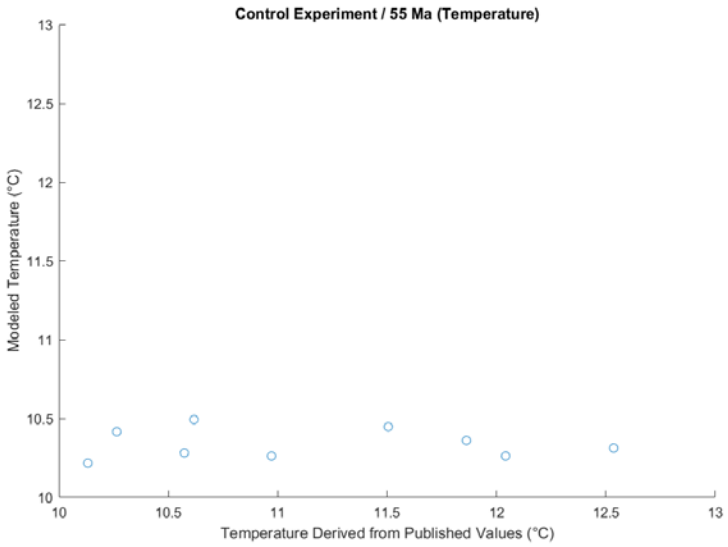

Figure 47: Comparison of temperature values between control model experiment and 55 Ma time slice of published data in the Cramer composite.

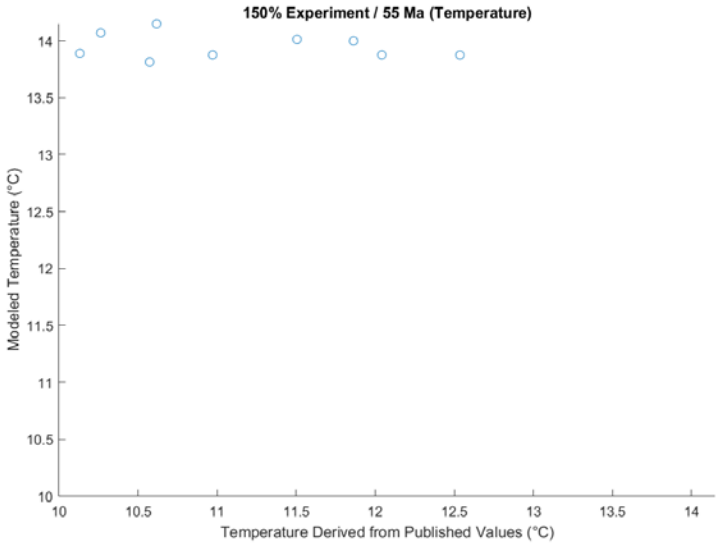

Figure 48: Comparison of temperature values between 150% volcanic outgassing flux experiment and 55 Ma time slice of published data in the Cramer composite.

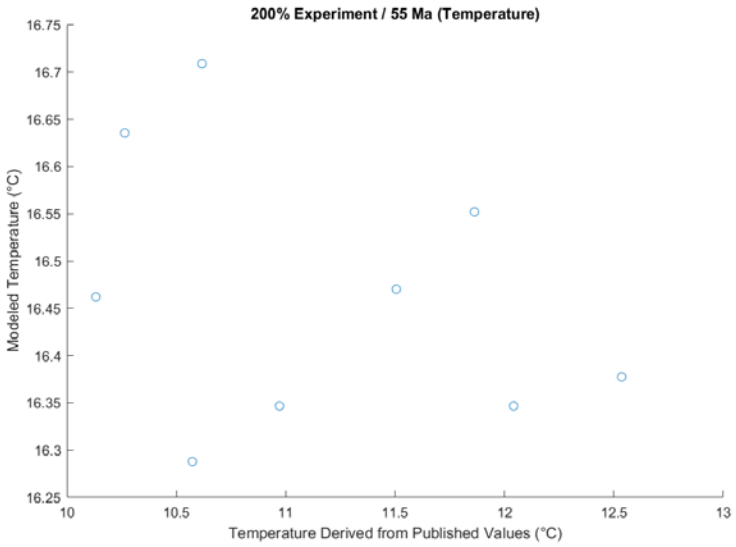

Figure 49: Comparison of temperature values between 200% volcanic outgassing flux experiment and 55 Ma time slice of published data in the Cramer composite.

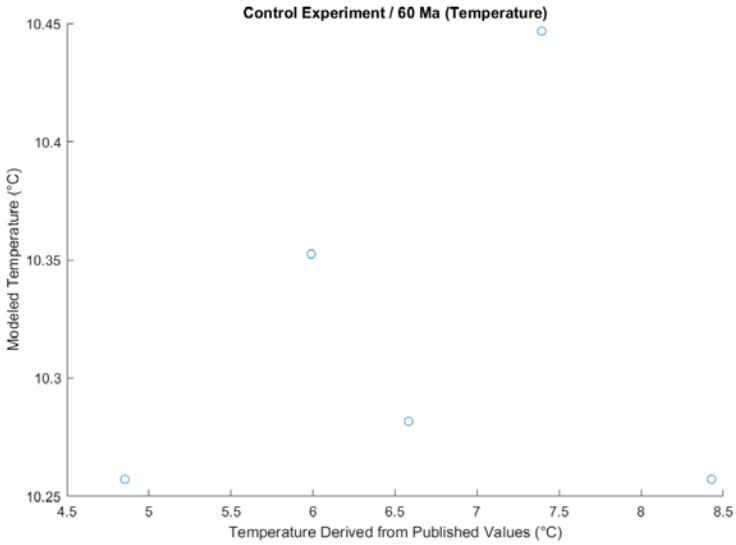

Figure 50: Comparison of temperature values between control model experiment and 60 Ma time slice of published data in the Cramer composite.

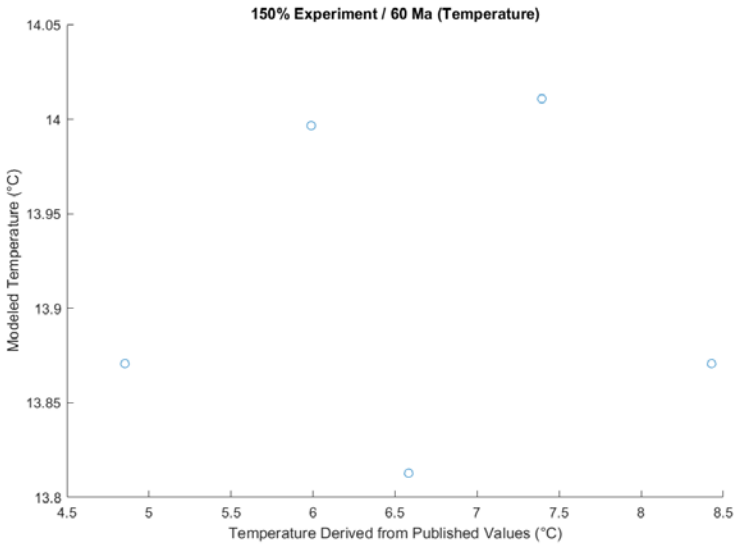

Figure 51: Comparison of temperature values between 150% volcanic outgassing flux experiment and 60 Ma time slice of published data in the Cramer composite.

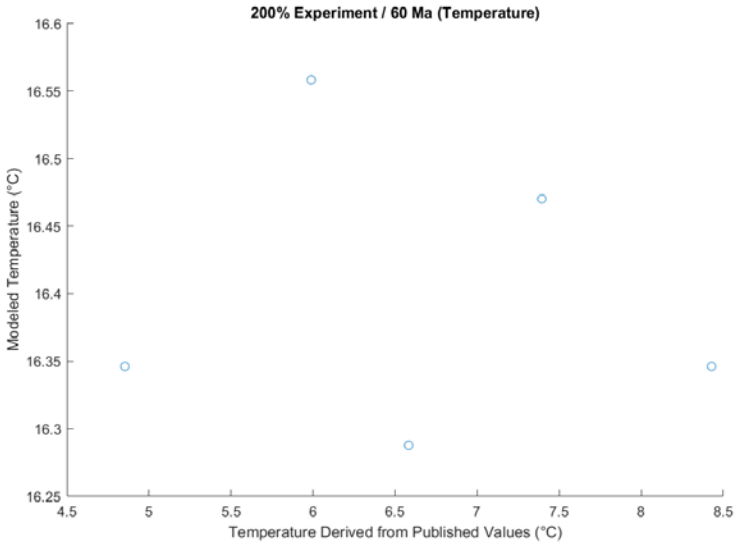

Figure 52: Comparison of temperature values between 200% volcanic outgassing flux experiment and 60 Ma time slice of published data in the Cramer composite.

in other tested model experiments, with a temperature range between 16.3 and 16.65 °C (a range of 0.35°C) (Figure 46, Figure 49, Figure 52).

Modeled $\delta^{13}C$ values and published $\delta^{13}C$ data track each other more closely compared to temperature (Figures 53-61). In the control experiment, modeled benthic DIC $\delta^{13}C$ varies between 1.15‰ and 1.6‰, with three outlier sites showing $\delta^{13}C$ between 0.4‰ and 0.5‰ (Figure 53, Figure 56, Figure 59). In the 150% outgassing experiment, this range shifts to between 0.5‰ to 0.9‰, with the outlier sites showing low $\delta^{13}C$ between -0.5‰ and -0.8‰ (Figure 54, Figure 57, Figure 60). This trend continues in the 200% outgassing experiment, with the typical range shifting to between 0.3‰ to -0.1‰ (a range of 0.4‰) (Figure 55, Figure 58, Figure 61). The published data doesn't show any values as negative as the model, with $\delta^{13}C$ between 0.4‰ and 1.2‰ (a range of

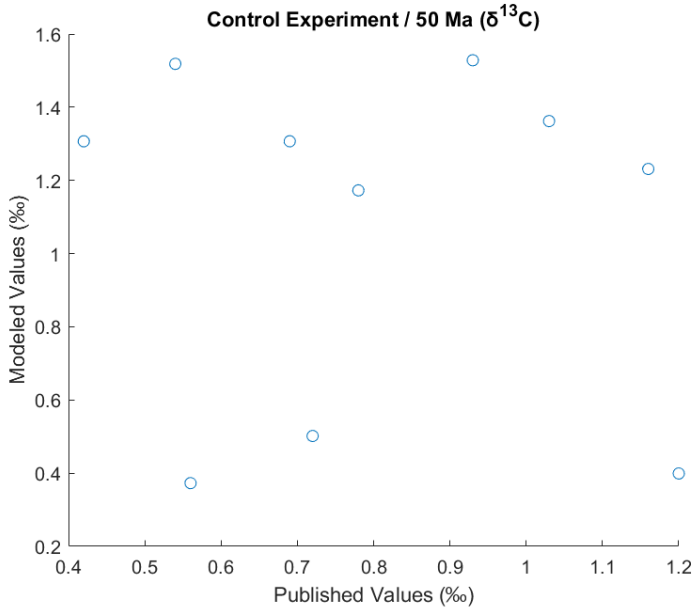

Figure 53: Comparison of $\delta^{13}C$ values between control model experiment and 50 Ma time slice of published data in the Cramer composite.

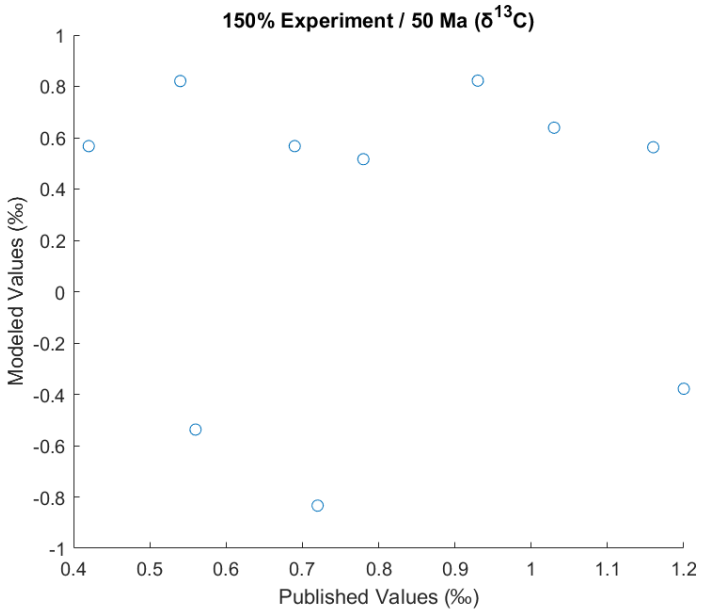

Figure 54: Comparison of $\delta^{13}C$ values between 150% volcanic outgassing flux experiment and 50 Ma time slice of published data in the Cramer composite.

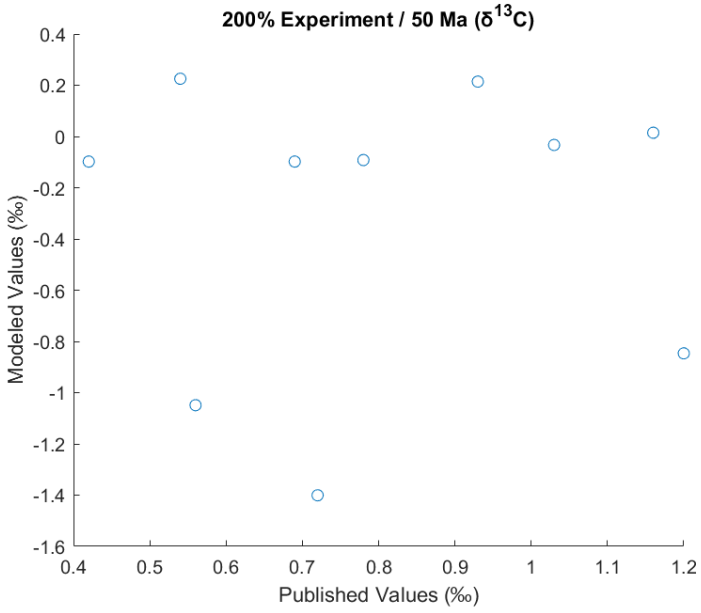

Figure 55: Comparison of $\delta^{13}C$ values between 200% volcanic outgassing flux experiment and 50 Ma time slice of published data in the Cramer composite.

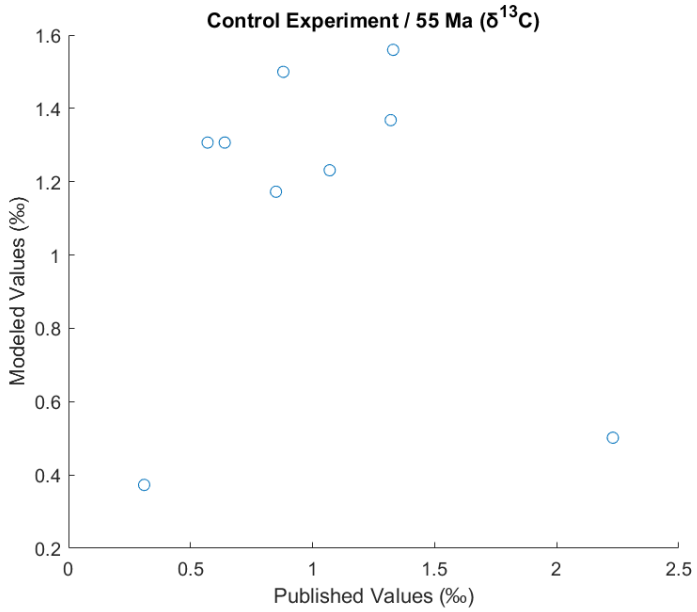

Figure 56: Comparison of $\delta^{13}C$ values between control model experiment and 55 Ma time slice of published data in the Cramer composite.

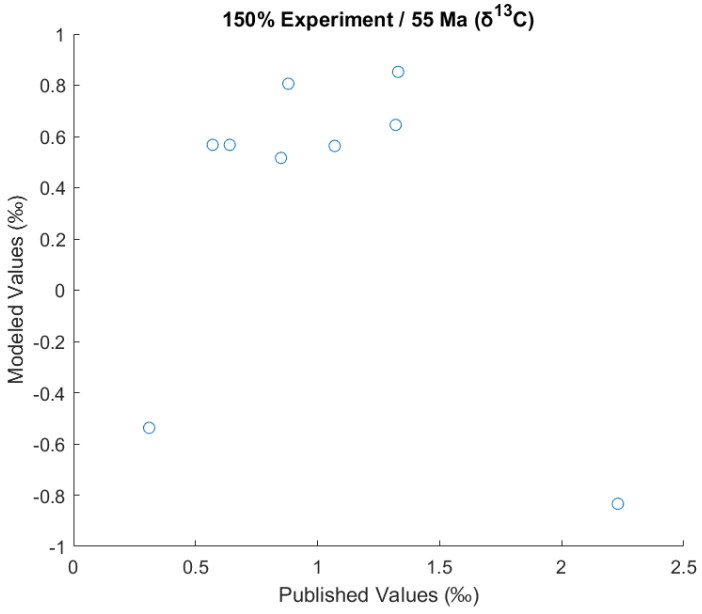

Figure 57: Comparison of $\delta^{13}C$ values between 150% volcanic outgassing flux experiment and 55 Ma time slice of published data in the Cramer composite.

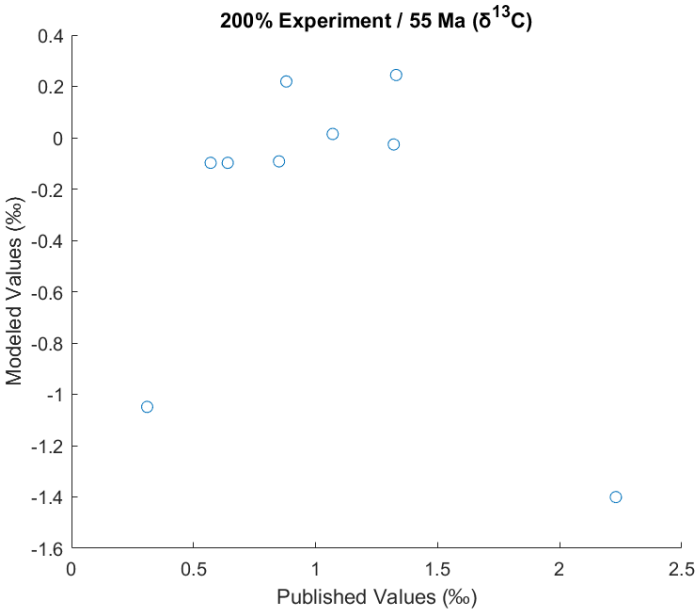

Figure 58: Comparison of $\delta^{13}C$ values between 200% volcanic outgassing flux experiment and 55 Ma time slice of published data in the Cramer composite.

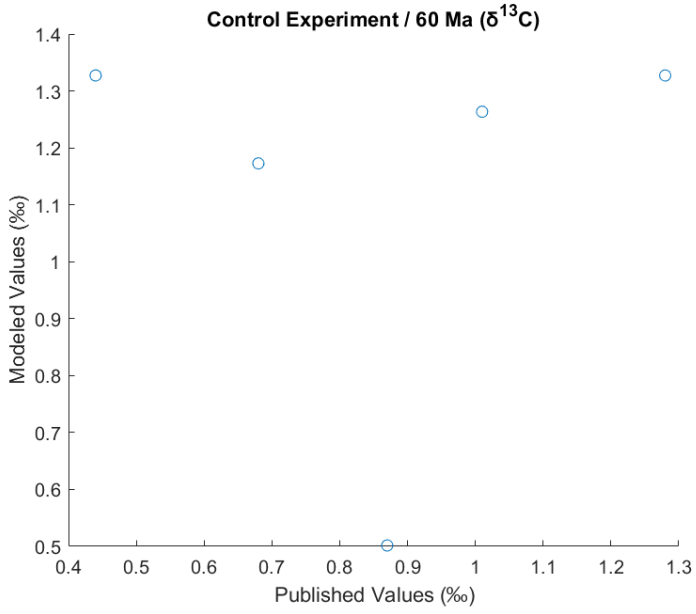

Figure 59: Comparison of $\delta^{13}C$ values between control model experiment and 60 Ma time slice of published data in the Cramer composite.

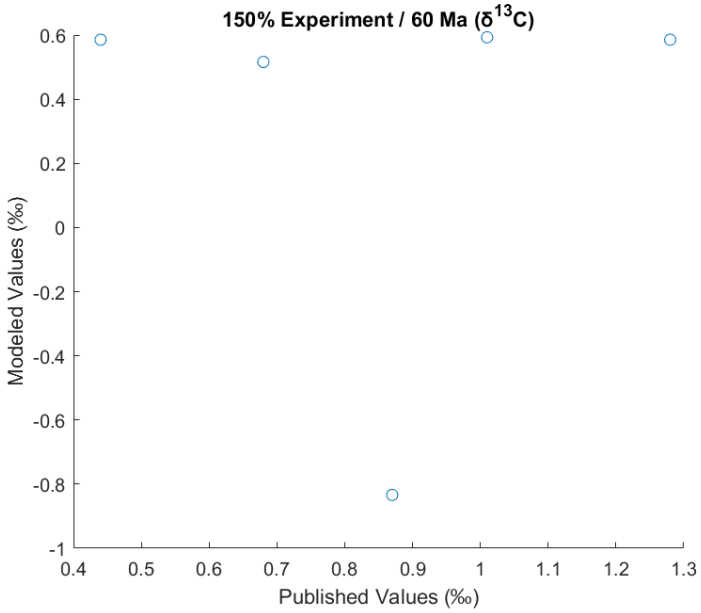

Figure 60: Comparison of $\delta^{13}C$ values between 150% volcanic outgassing flux experiment and 60 Ma time slice of published data in the Cramer composite.

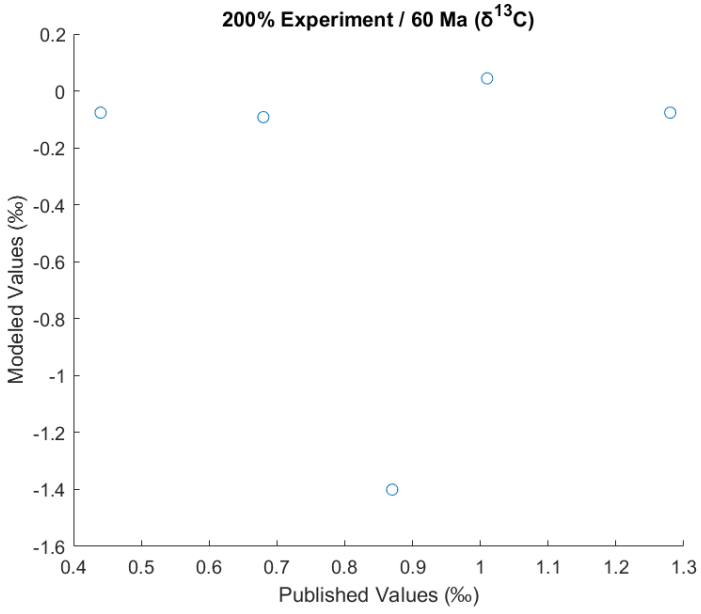

Figure 61: Comparison of $\delta^{13}C$ values between 200% volcanic outgassing flux experiment and 60 Ma time slice of published data in the Cramer composite.

0.8‰) in the 50 Ma time slice, between 0.25‰ and 2.25‰ (a range of 2‰) in the 55 Ma time slice, and between 0.4‰ and 1.3‰ (a range of 0.9‰) in the 60 Ma time slice (Figures 53-61). There is some notable clustering in the 55 Ma time slice, with all but one of the published sites characterized by $\delta^{13}C$ between 0.5‰ and 1.5‰ (Figures 56-58); in other words, the unusually large range of 2‰ in this time slice compared to the others is driven by just one site.

Tables 1 and 2 provide the coefficients of correlation for each comparison of modeled isotope values from each outgassing experiment to each time-slice of published isotope and temperature data, in order to determine which time slice of data from the Cramer composite most resembles which volcanic outgassing experiment. Overall the coefficients of correlation are low; the strongest correlation occurs in the temperature-wise comparison of the 50 Ma time slice to the 200% outgas volume experiment, where the coefficient is just 0.2107, with a p-value is 4.7583×10^{-7}, indicating the result is not significant.

	Published $\delta^{13}C$ per Time Slice			
Modeling Experiment $\delta^{13}C$		50 myr	55 myr	60 myr
	Control	0.009	0.0133	1.69E-04
	150% OG	3.74E-05	0.0907	6.59E-05
	200% OG	0.0014	0.0982	1.29E-05

Table 1: Compilation of correlation coefficients for each corresponding pair of published data time slices and modeling experiments for $\delta^{13}C$ results.

	Published temperature per Time Slice			
Modeling Experiment temperature		50 myr	55 myr	60 myr
	Control	0.0084	0.0024	3.12E-02
	150% OG	5.45E-02	0.0522	3.00E-03
	200% OG	0.2107	0.1063	5.10E-03

Table 2: Compilation of correlation coefficients for each corresponding pair of published data time slices and modeling experiments for $\delta^{18}O$ results converted to temperatures.

Nonetheless, this analysis indicates that the volcanic outgassing experiment that best matches both the 50 Ma and 60 Ma time slices in terms of $\delta^{13}C$ is the control scenario (Table 1). For the 55 Ma $\delta^{13}C$ time slice, the 200% volcanic outgassing flux scenario has the strongest correlation. This changes somewhat in the correlation of temperatures, with the 200% outgas experiment having the strongest correlation to both the 50 and 55 Ma time slices, and the control experiment having the strongest correlation to the 60 Ma time slice (Table 2).

Finally, I used the site overlays to generate plots that compare steady state benthic $\delta^{13}C$ and temperatures between each experiment (Figures 62-79). In terms of the $\delta^{13}C$ plots, we can see a site-by-site decomposition of the model values utilized in the overlay comparisons, indicating that the most negative model sites are those equivalent to DSDP Site 98, DSDP Site 384, and ODP Site 1258 (Figures 62-63, Figure 70), while all others generally had higher benthic $\delta^{13}C$ values (Figures 64-70). In the set of temperature plots, we see that benthic temperatures are very similar from site to site, no matter which volcanic outgassing experiment is considered (Figures 71-79).

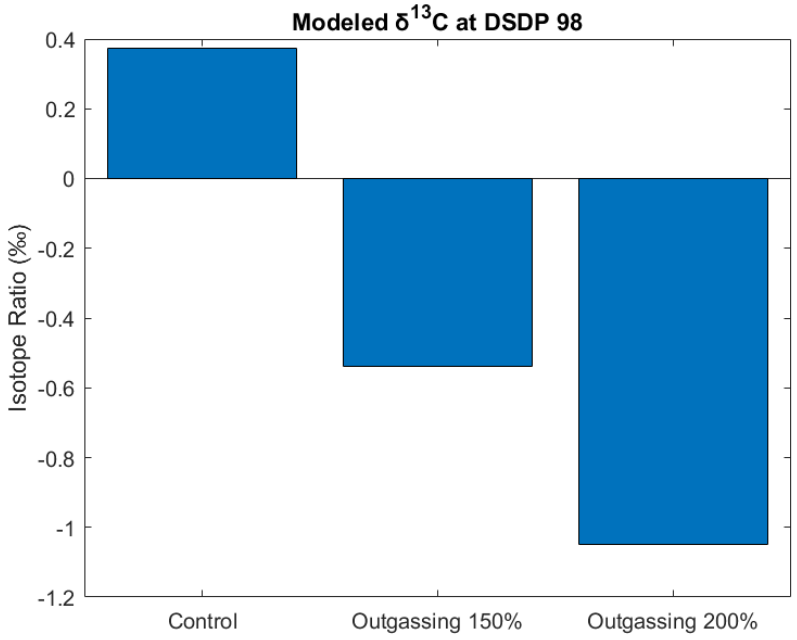

Figure 62: Comparison of end-state $\delta^{13}C$ among various modeling experiments at the geographic location of DSDP Site 98.

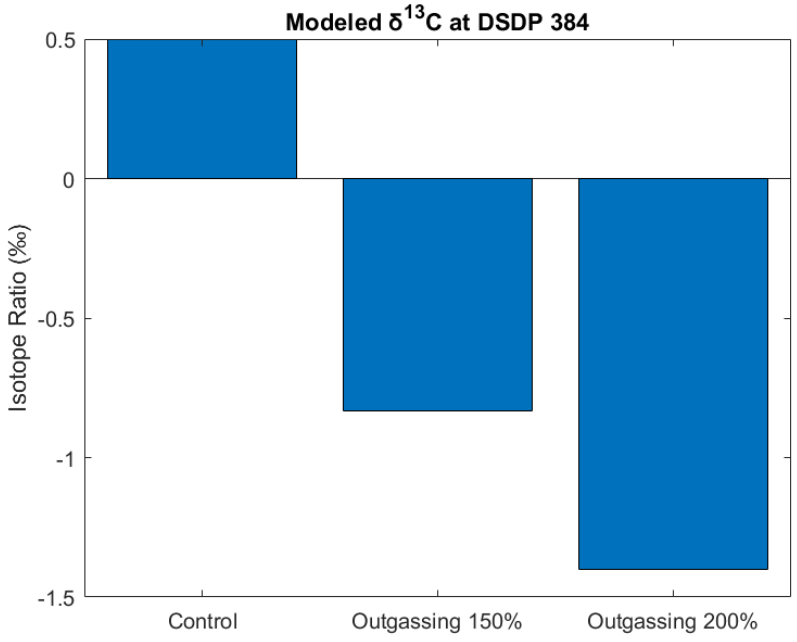

Figure 63: Comparison of end-state $\delta^{13}C$ among various modeling experiments at the geographic location of DSDP Site 384.

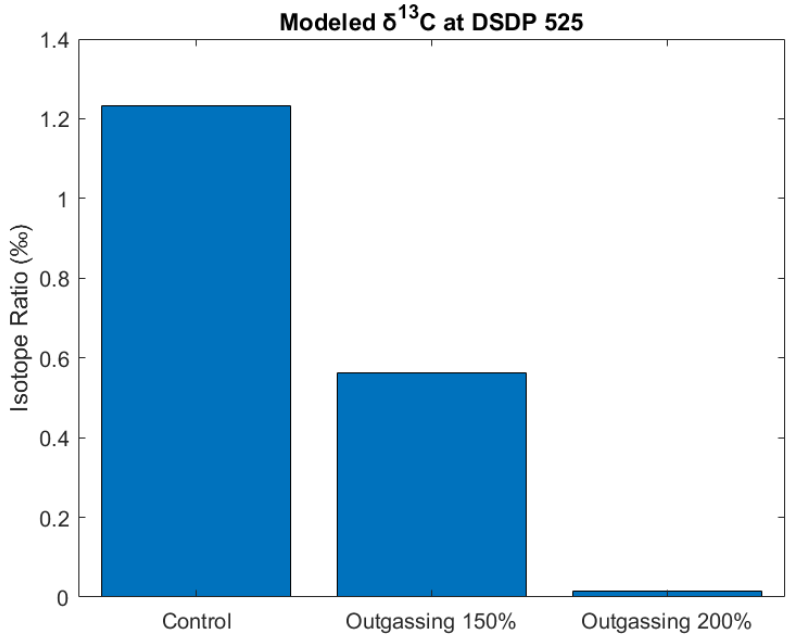

Figure 64: Comparison of end-state $\delta^{13}C$ among various modeling experiments at the geographic location of DSDP Site 525.

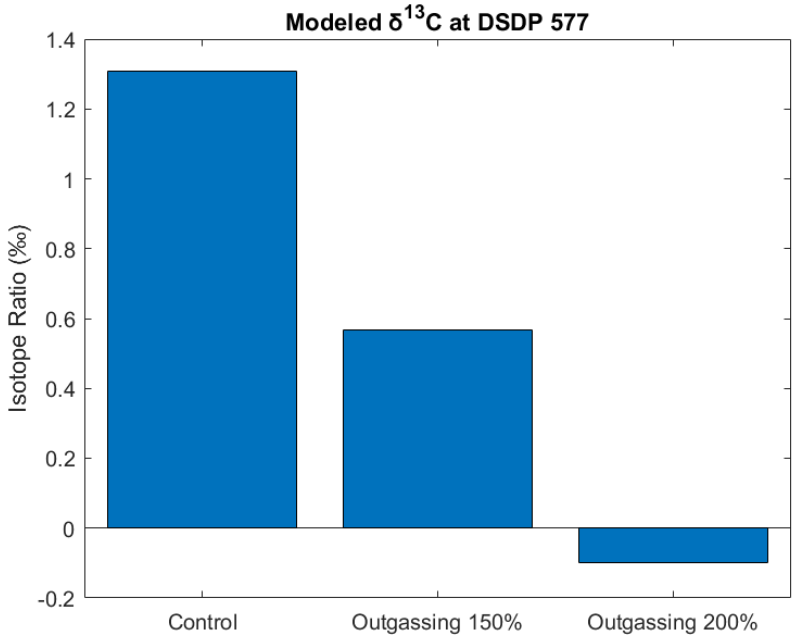

Figure 65: Comparison of end-state $\delta^{13}C$ among various modeling experiments at the geographic location of DSDP Site 577.

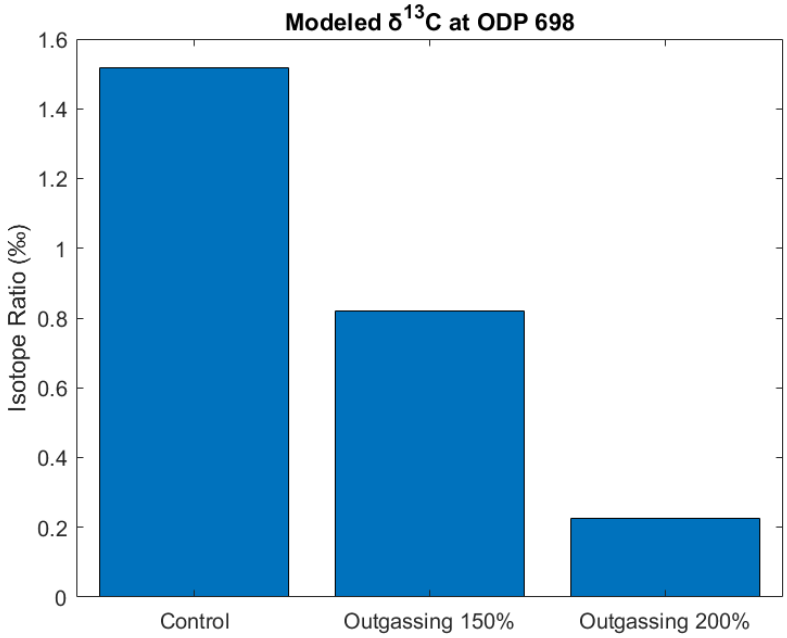

Figure 66: Comparison of end-state $\delta^{13}C$ among various modeling experiments at the geographic location of ODP Site 698.

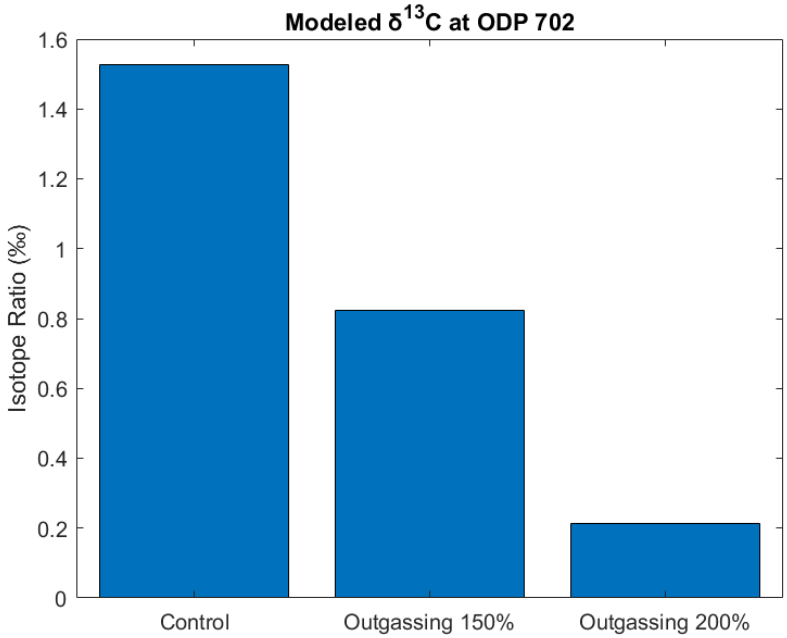

Figure 67: Comparison of end-state $\delta^{13}C$ among various modeling experiments at the geographic location of ODP Site 702.

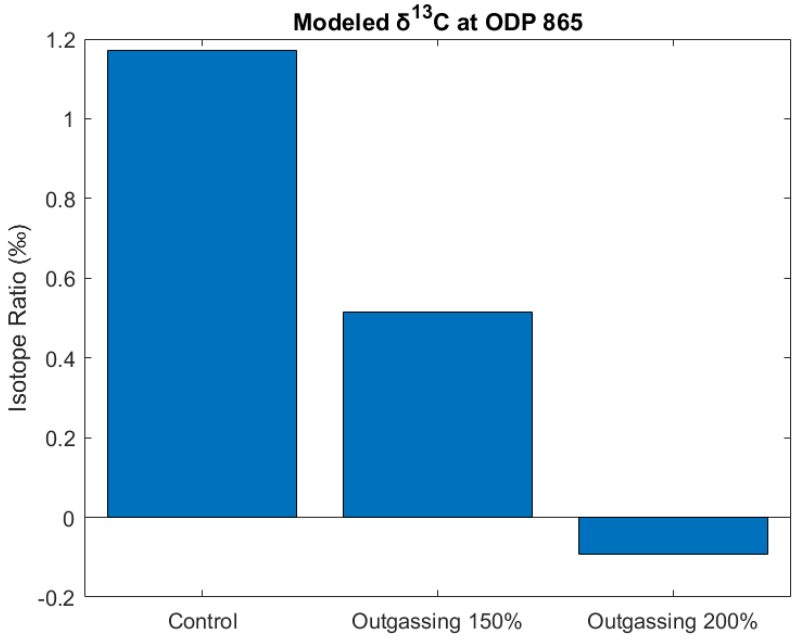

Figure 68: Comparison of end-state $\delta^{13}C$ among various modeling experiments at the geographic location of ODP Site 865.

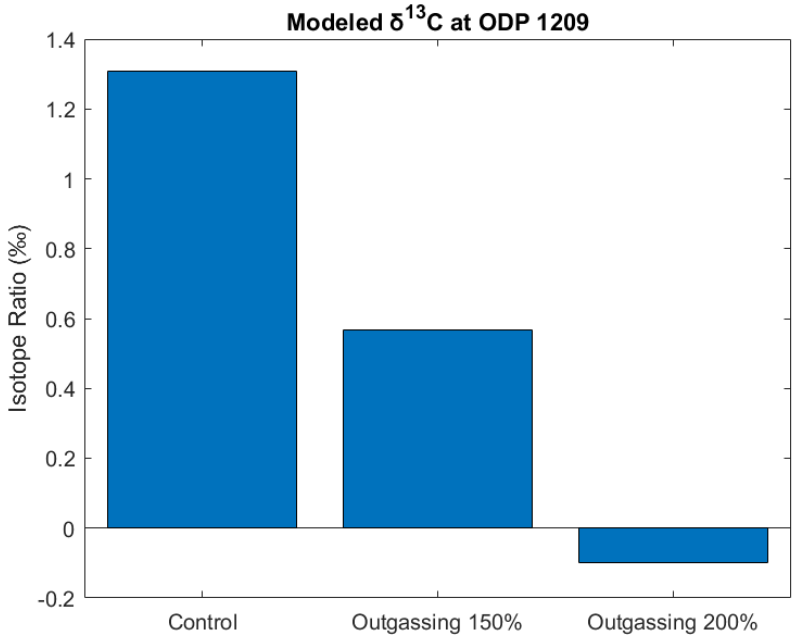

Figure 69: Comparison of end-state $\delta^{13}C$ among various modeling experiments at the geographic location of ODP Site 1209.

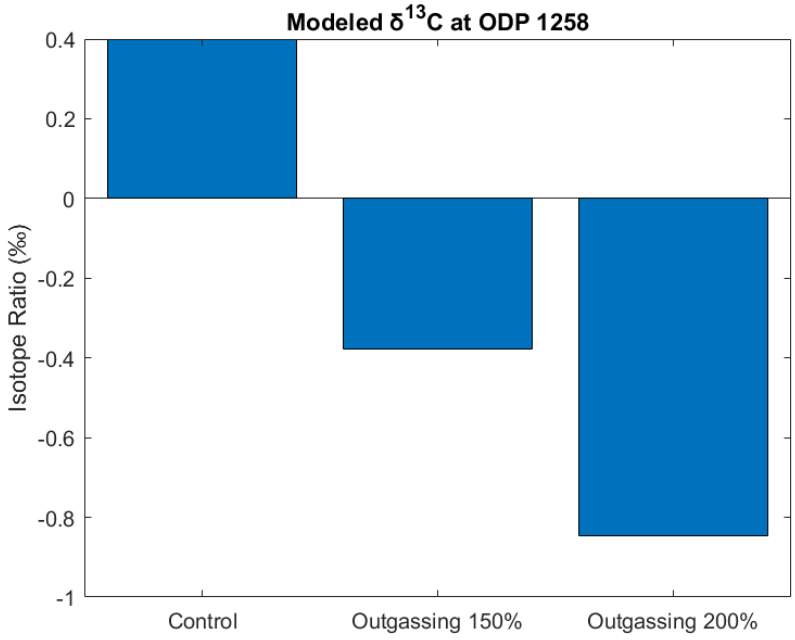

Figure 70: Comparison of end-state $\delta^{13}C$ among various modeling experiments at the geographic location of ODP Site 1258.

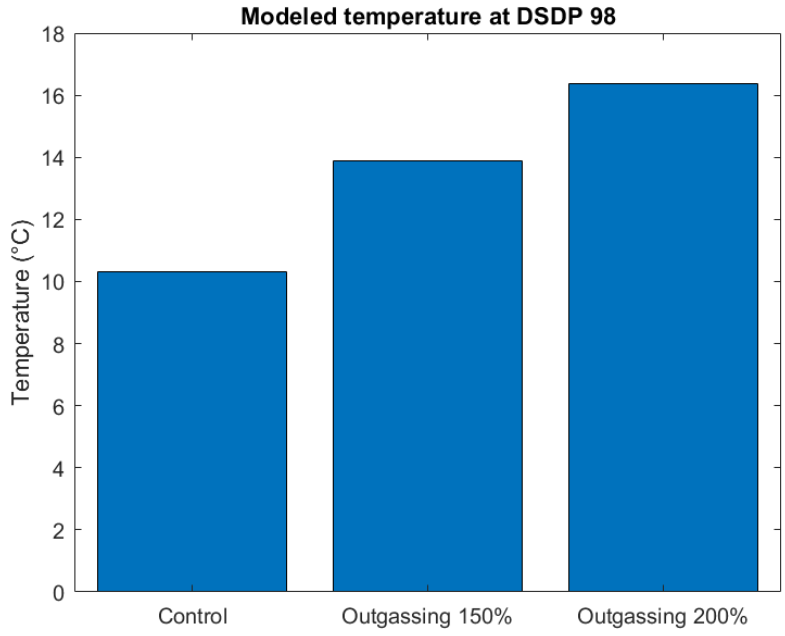

Figure 71: Comparison of end-state temperature among various modeling experiments at the geographic location of DSDP Site 98.

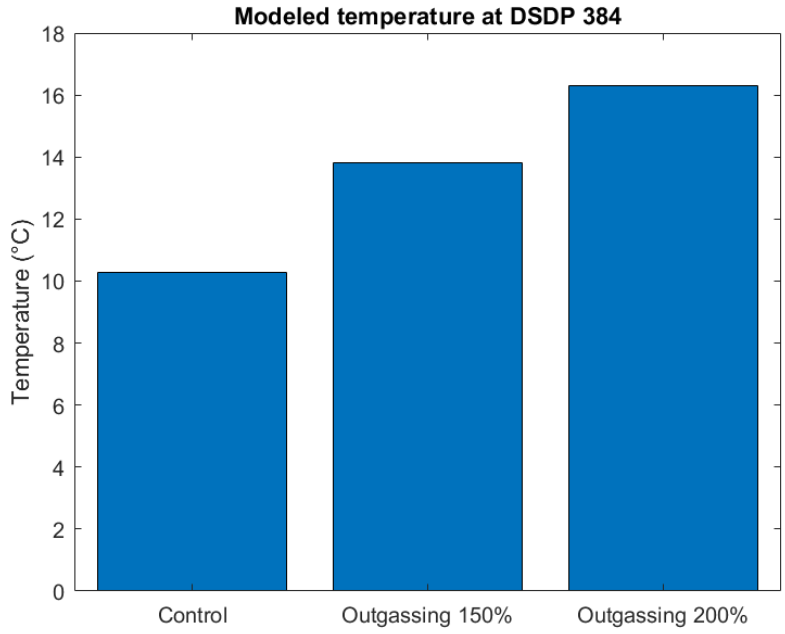

Figure 72: Comparison of end-state temperature among various modeling experiments at the geographic location of DSDP Site 384.

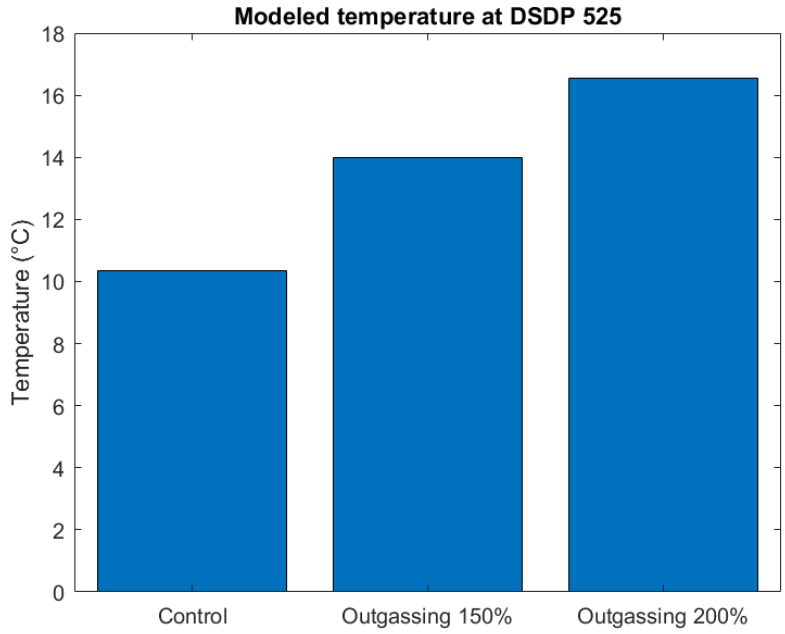

Figure 73: Comparison of end-state temperature among various modeling experiments at the geographic location of DSDP Site 525.

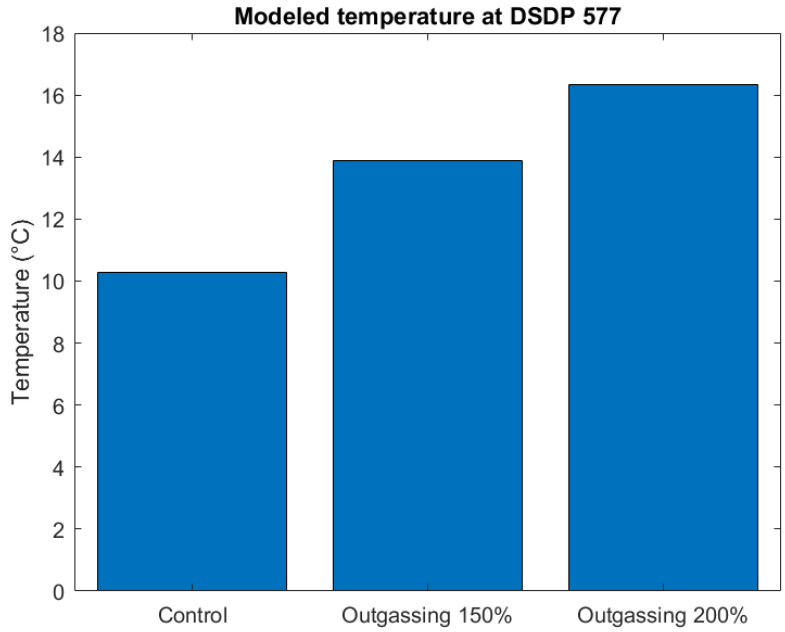

Figure 74: Comparison of end-state temperature among various modeling experiments at the geographic location of DSDP Site 577.

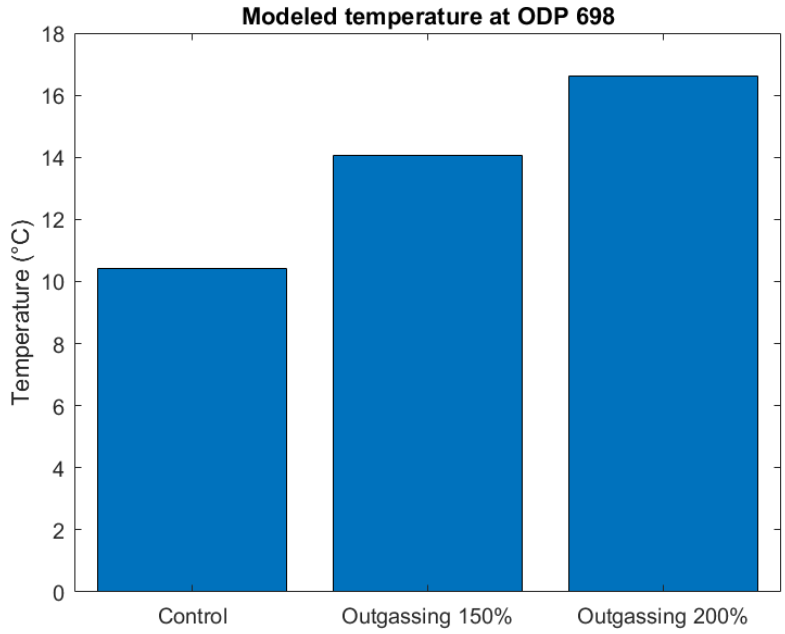

Figure 75: Comparison of end-state temperature among various modeling experiments at the geographic location of ODP Site 698.

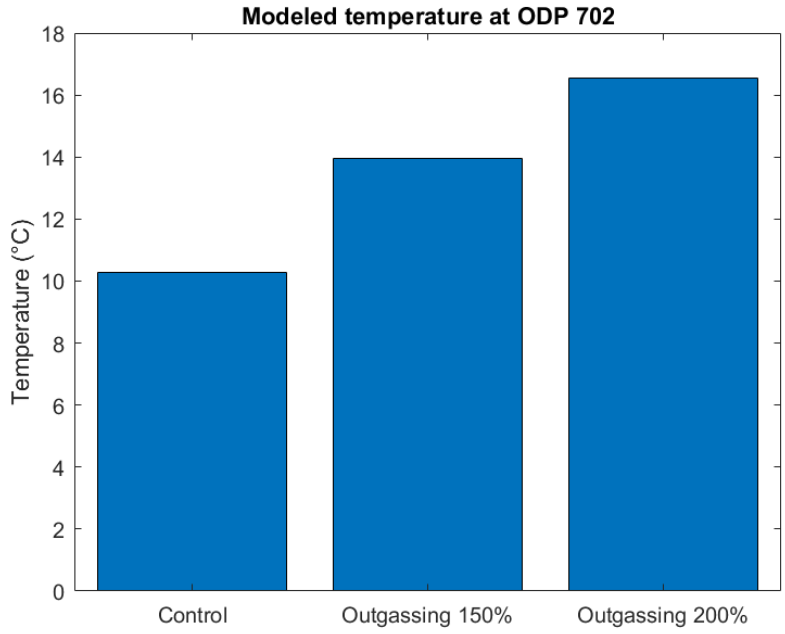

Figure 76: Comparison of end-state temperature among various modeling experiments at the geographic location of ODP Site 702.

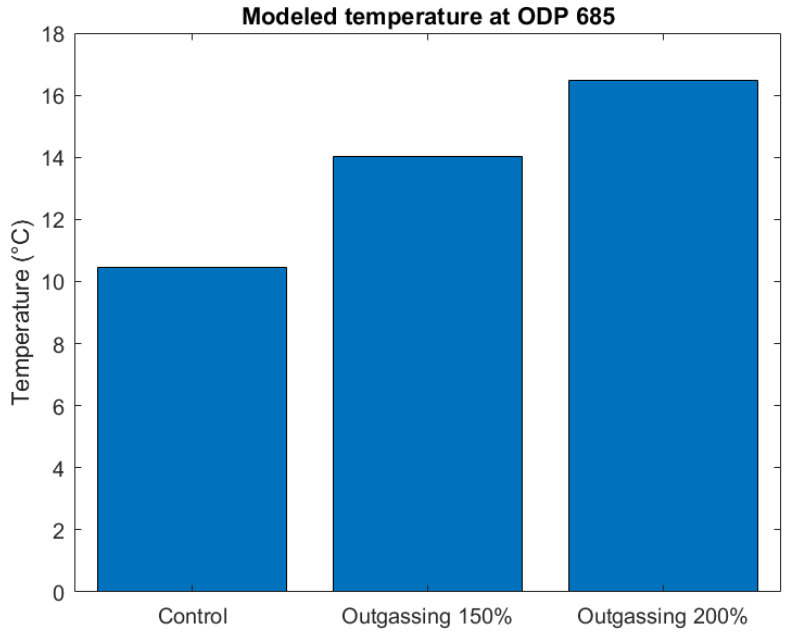

Figure 77: Comparison of end-state temperature among various modeling experiments at the geographic location of ODP Site 865.

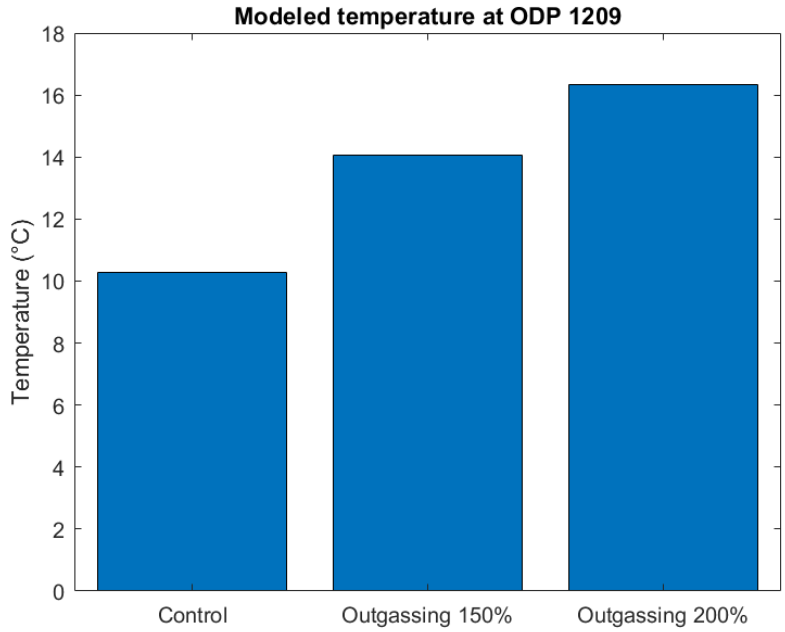

Figure 78: Comparison of end-state temperature among various modeling experiments at the geographic location of ODP Site 1209.

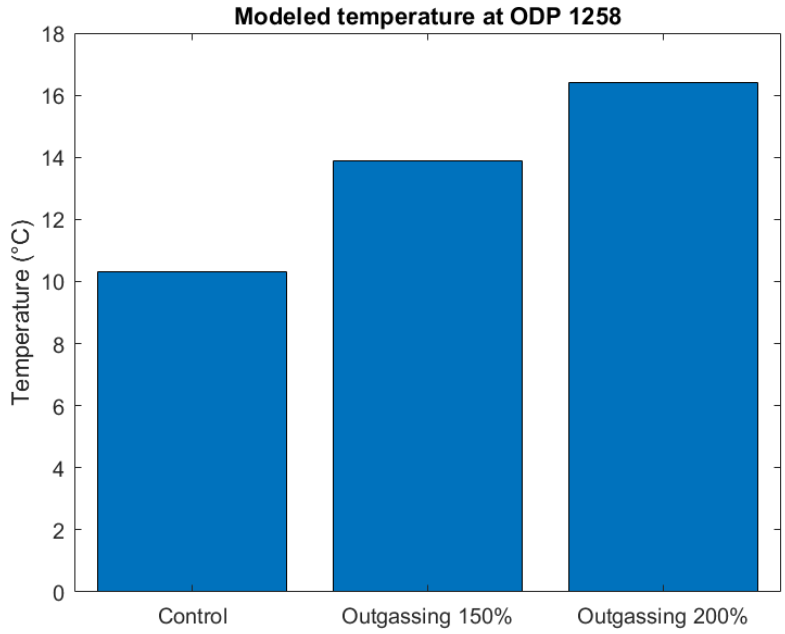

Figure 79: Comparison of end-state temperature among various modeling experiments at the geographic location of ODP Site 1258.

3.4 – BENTHIC FORAMINIFERAL DATASET FOR ODP SITE 1258

In the foraminiferal isotope dataset that was generated for this study, we can observe changes in the benthic marine chemistry at Site 1258 across the dataset's 50-52 Ma age span (Figures 80-81). In the $\delta^{13}C$ record, maximum benthic $\delta^{13}C$ is 0.889‰ at approximately 50.816 Ma, while minimum $\delta^{13}C$ occurs at approximately 51.847 Ma with a ratio of -1.156‰ (Figure 80). There is an overall positive trend in $\delta^{13}C$ from the oldest age to the youngest, with a linear regression approximating a 0.96‰ mean increase over the span of the dataset, with a coefficient of correlation of 0.41. In the $\delta^{18}O$ record, the maximum $\delta^{18}O$ ratio present in the benthic record is -0.566‰ at an age of approximately 51.924 Ma, while minimum $\delta^{18}O$ reaches a ratio of -1.684 at approximately 50.570 Ma (Figure 81). There is a very slightly negative trend in the $\delta^{18}O$ record, as the linear regression approximates a 0.0056‰ decrease in $\delta^{18}O$ over the span of the data, with a coefficient of determination of 0.00006.

When comparing the newly-generated benthic foraminiferal isotope datasets to the bulk carbonate datasets generated for the same site in Turner et al. (2014), it is very apparent that most patterns in the $\delta^{13}C$ signals are coherent to a relatively high degree. When the difference between the two datasets is plotted to approximate the vertical $\delta^{13}C$ gradient, it is revealed that the gradient decreases from oldest to youngest, with a linear regression approximating a 0.26‰ reduction in the difference between the benthic and the surface signal, with a coefficient of determination of 0.104 (Figure 82).

Comparing the $\delta^{18}O$ values of the benthic foraminiferal dataset to those of the bulk carbonate dataset reveals different observations. Patterns in the benthic dataset do not match the surface signal quite as clearly as they do in the $\delta^{13}C$ comparison, and there are even a few points near the 50.7 Ma age in which it appears that the benthic level has a lower $\delta^{18}O$ ratio than the surface (suggestive of higher temperatures). Despite these patterns, plotting the difference between the two signals shows that there is a very slight decrease in the vertical $\delta^{18}O$ gradient through time, in which the linear regression of the bulk-benthic difference approximates a 0.064‰ reduction in the gradient by the end of the dataset, with a coefficient of determination of 0.0048 (Figure 83).

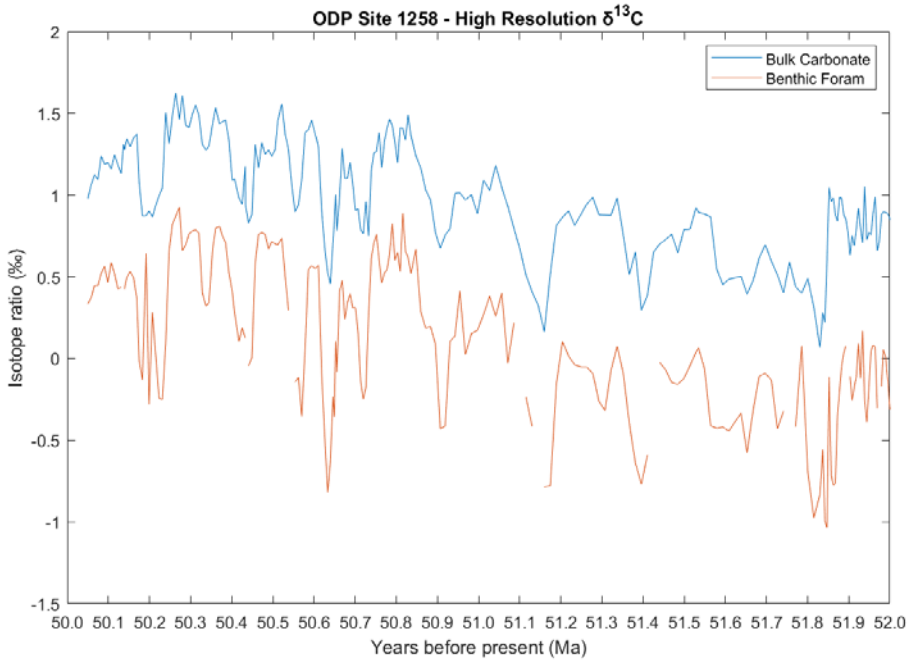

Figure 80: High-resolution $\delta^{13}C$ datasets sampled from ODP Site 1258.

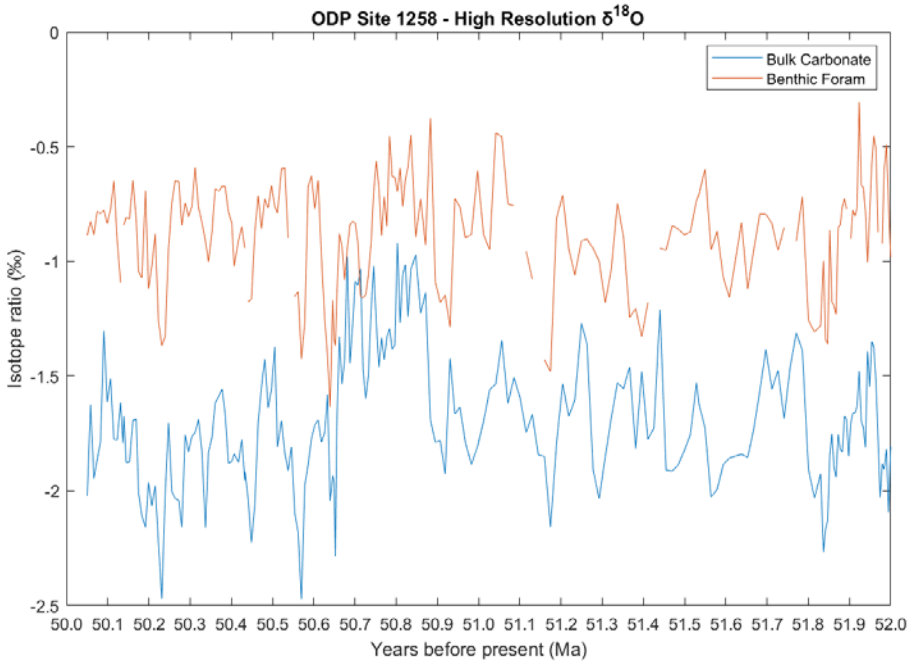

Figure 81: High-resolution $\delta^{18}O$ datasets sampled from ODP Site 1258.

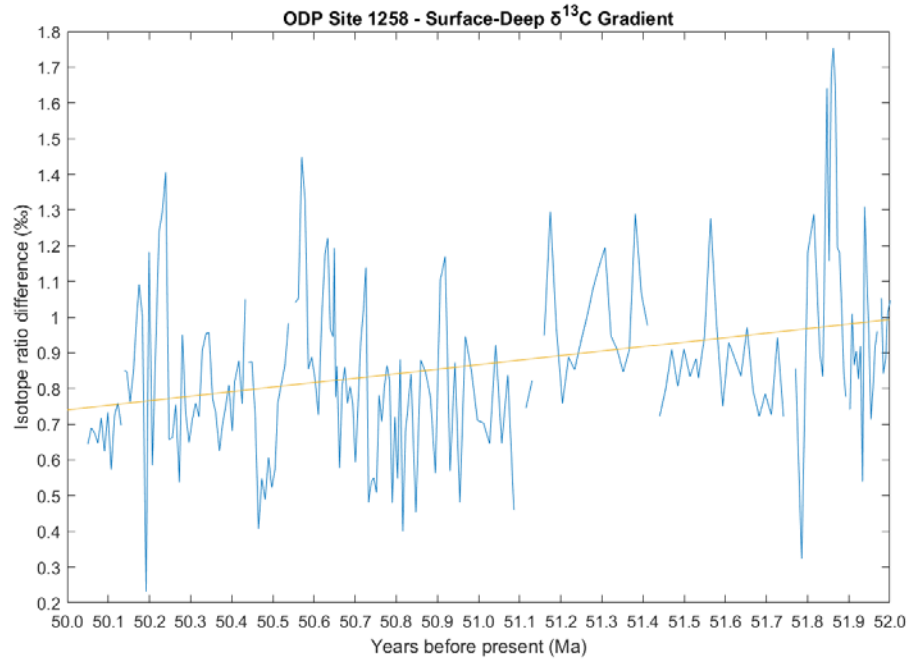

Figure 82: Surface-benthic gradient of $\delta^{13}C$ utilizing the above datasets. The linear regression has been plotted in yellow.

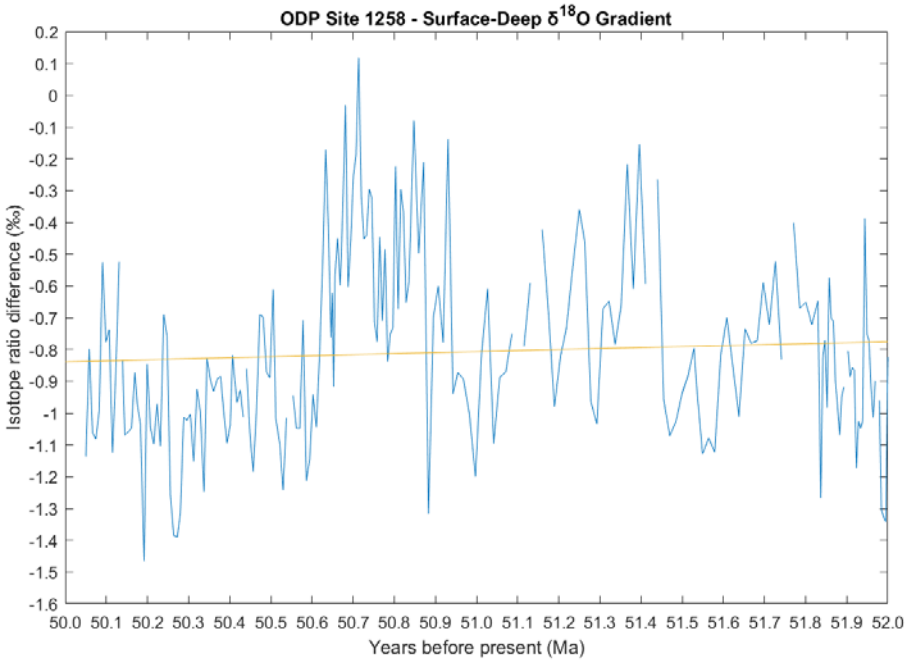

Figure 83: Surface-benthic gradient of $\delta^{13}O$ utilizing the above datasets. The linear regression has been plotted in yellow.

CHAPTER 4 – DISCUSSION

4.1 – LINKS BETWEEN MODEL SIMULATIONS AND DATA

Among the sites within the Cramer compilation that were considered to have sufficiently high resolution through EECO, examining the site-by-site decompositions of the compilation clearly shows, as originally posited, that a significant time gap exists between the benthic carbon and oxygen isotope minima. Furthermore, there is a relatively strong correlation between the size of the signal asynchronicity and the distance of each site from the equator, particularly considering locations in the Southern Ocean. This pattern of shortening time-lag size is consistent with patterns of benthic DIC $\delta^{13}C$

enrichment present in the enhanced volcanic outgassing cGENIE experiments, particularly the 200% outgassing flux scenario. Thus, looking to the distribution of $\delta^{13}C$ throughout the deep ocean may provide explanation for the asynchronicity. When taken together, it is consistent that marine regions modeled with a high positive anomaly of benthic $\delta^{13}C$ match up reasonably well with DSDP/ODP drilling sites that display a large offset between the $\delta^{13}C$ and $\delta^{18}O$ signals. From what we can observe with the modeling experiments, it is plausible that the asynchronicity between isotope signals is tied to the regional variations in $\delta^{13}C$ that arise from global changes to the deep ocean carbon reservoir. It's unfortunate that the Cramer compilation lacked suitable sites within the far northern Atlantic Ocean, at sites comparable to the latitudes in the Southern Ocean – since the northern Atlantic is modeled as the end of the Eocene deep water flow path, its relatively aged waters should reflect a small signal asynchronicity. Proof of this would help to further reinforce the interpretation that the asynchronicity is at least partly related to changing ocean circulation, and would be a great way to lead into further investigation of the mechanisms behind the signal offset.

Observing the spatial distribution of vertical gradients in $\delta^{13}C$ provides a complementary perspective. Regions with a flatter surface-benthic $\delta^{13}C$ gradients in the model are generally associated with greater vertical mixing. From analysis of vertical $\delta^{13}C$ gradients as a function of volcanic outgassing flux, we can see that, while the entirety of the Atlantic experiences gradient flattening to some degree with increased volcanic outgassing, the southern Atlantic and Southern Ocean consistently display a flatter gradient than northern regions of the ocean, with the gradient gradually steepening

as one traces a path northward from the southernmost latitudes. This reproduces the pattern evident from the modeled benthic DIC $\delta^{13}C$ values at ~2300 m water depth, with the southern Atlantic generally having more $\delta^{13}C$ enriched waters at this depth than the northern Atlantic. This is consistent with greater ocean overturning in the Eocene at the southern latitudes. The smooth progression to a steeper gradient in northern latitudes suggests that deep water formed in the southern Atlantic and traveled northward, with the vertical gradient increasing as the deep-ocean water aged. This is corroborated by the modeled global streamfunction overlain on the vertical DIC $\delta^{13}C$ profiles; increased volcanic outgassing results in a global steady-state ocean with enhanced convection in the southern latitudes.

The new high resolution benthic isotopic dataset from ODP Site 1258 also provides evidence for how deep water circulation has changed in the region. When comparing this dataset to the bulk carbonate dataset from Turner et al. (2014), we can observe a steady decrease in the surface-benthic $\delta^{13}C$ gradient, with the linear regression decreasing from a surface-benthic difference of about 1.1‰ at 52 Ma to about 0.9‰ at 50 Ma. This flattening of the vertical $\delta^{13}C$ gradient, along with the minute decrease in the $\delta^{18}O$ gradient, are consistent with modeling experiments with enhanced volcanic outgassing fluxes. When comparing the Site 1258 data to the cGENIE experiments, it appears that the 200% volcanic outgassing flux experiment results in an equatorial South Atlantic region with a vertical $\delta^{13}C$ gradient that matches that of both the start and the end of the dataset fairly well, with a modeled gradient of ~0.9‰, compared to ODP Site 1258's gradient of ~1‰ at 52 Ma, and ~0.8‰ at 50 Ma. By comparison, the $\delta^{13}C$

gradient in this region is ~2.3‰ in the control run, ~1.6‰ in the 150% outgassing flux experiment, and ~0.2‰ in the 300% outgassing flux experiment. More experiments testing different fluxes of volcanic CO_2 outgassing may help to pinpoint likely scenarios that may represent conditions across varying stages across EECO. Using the other experiment gradients as a basis, we can infer that a model experiment with volcanic outgassing flux of slightly less than 150% could better fit the gradient at 52 Ma, while a flux of slightly more than 150% could better fit the gradient at 50 Ma.

None of the modeling experiments were able to consistently reproduce both temperature and $\delta^{13}C$ trends that we observe in the Cramer compilation. The coefficients of correlation between the compared values are extremely low, which suggests that the model experiments are missing some key process and/or forcing. Nevertheless, it appears that the 60 Ma time slice of the Cramer data best matches the conditions modeled in the control experiment in both $\delta^{13}C$ and $\delta^{18}O$, and the 55 Ma time slice likewise best matches the 200% volcanic outgassing flux experiment. These experiments represent significantly different global climate states – in the 200% outgassing flux scenario, atmospheric CO_2 is higher in concentration by about 600 ppm, deep ocean temperatures are 6 °C warmer, and benthic $\delta^{13}C$ is lower by about 1.52‰. Although the correlation between model and data for individual sites is weak, the consistency of the matches is significant. This carries the implication that global warming was driven by enhanced outgassing during this time interval, though the exact magnitude of the forcing could be refined with more experimentation to results that have closer matches to the data. The 50 Ma time slice behaves differently, with the $\delta^{13}C$ signal more closely matching the control experiment,

and the paleotemperatures derived from $\delta^{18}O$ more closely matching the 200% outgassing experiment. This apparent disagreement in volcanic outgassing scenario matches the isotope signal asynchronicity that is prevalent throughout the Cramer compilation, with the global benthic $\delta^{13}C$ signal showing signs of recovery by the 50 Ma time period, while temperatures still reflect conditions of enhanced volcanic outgassing. I believe these results represent an important step towards understanding the mechanism of the isotope signal asynchronicity, and with some refinements to the model experiments, this will help lead to being able to model it directly. Particularly, we need a forcing that can generate heavier $\delta^{13}C$ without lowering temperature.

4.2 – COMPARISONS TO SIMILAR STUDIES

It is important to place my findings in the context of the Cramer et al. (2009) analysis. Cramer examined interbasinal isotopic gradients in order to trace the evolution of ocean chemistry through the late Cretaceous to the early Paleogene. One of the key findings regarding the spatial distribution of $\delta^{13}C$ was that, through the EECO, southern Atlantic benthic $\delta^{13}C$ was consistently higher than that in any other ocean basin, and that spatial reorganization of benthic $\delta^{13}C$ through time is evidence that overturning circulation had continued evolving through the warming events of the early Paleogene (Figure 84). My model results agree with these observations from the data, particularly when assuming a scenario of enhanced outgassing that could have contributed to the EECO.

I can also draw comparisons between the ODP Site 1258 records and data produced by Littler et al. (2014), which generated isotopic data from ODP Site 1262 (on the Walvis Ridge in the southern Atlantic) from the late Paleocene to early Eocene.

Although Littler et al. do not directly evaluate the evolution of vertical gradients in isotope signals, they do include benthic and bulk isotope records from the site spanning 60.5-52.5 Ma, and although there is no temporal overlap with the records used in this study, some interesting observations can be made by comparing them. For the purposes of this comparison, I plotted the bulk carbonate and benthic foraminiferal $\delta^{13}C$ and $\delta^{18}O$ datasets and calculated the gradients between them, just as I did for the ODP Site 1258 datasets (Figures 85-88).

After applying a linear regression, I find that the surface-deep $\delta^{13}C$ gradient decreases from a 1.4‰ difference at ~60.0 Ma to a 1.1‰ difference at ~52.8 Ma. The same methodology applied to the $\delta^{18}O$ signal shows the surface-deep $\delta^{18}O$ gradient decreasing from a -0.88‰ difference at ~60.0 Ma (with calculated surface temperatures of ~11.6 °C, compared to benthic temperatures of 8.4 °C) to a 0.08‰ difference at ~52.8 Ma (with calculated surface temperatures of ~12.4 °C, compared to benthic temperatures of ~14.2 °C), with a gradient reversal at ~53.4 Ma. Although it would be inappropriate to extrapolate the isotope signals of this site to the younger time span of this study (50-52 Ma), the decreasing $\delta^{13}C$ gradient recorded in ODP Site 1262 across the late Paleocene is consistent with the continuing reduction in the gradient found in our ODP Site 1258 dataset. Both of these datasets are pointing to greater overturning throughout the progression of EECO.

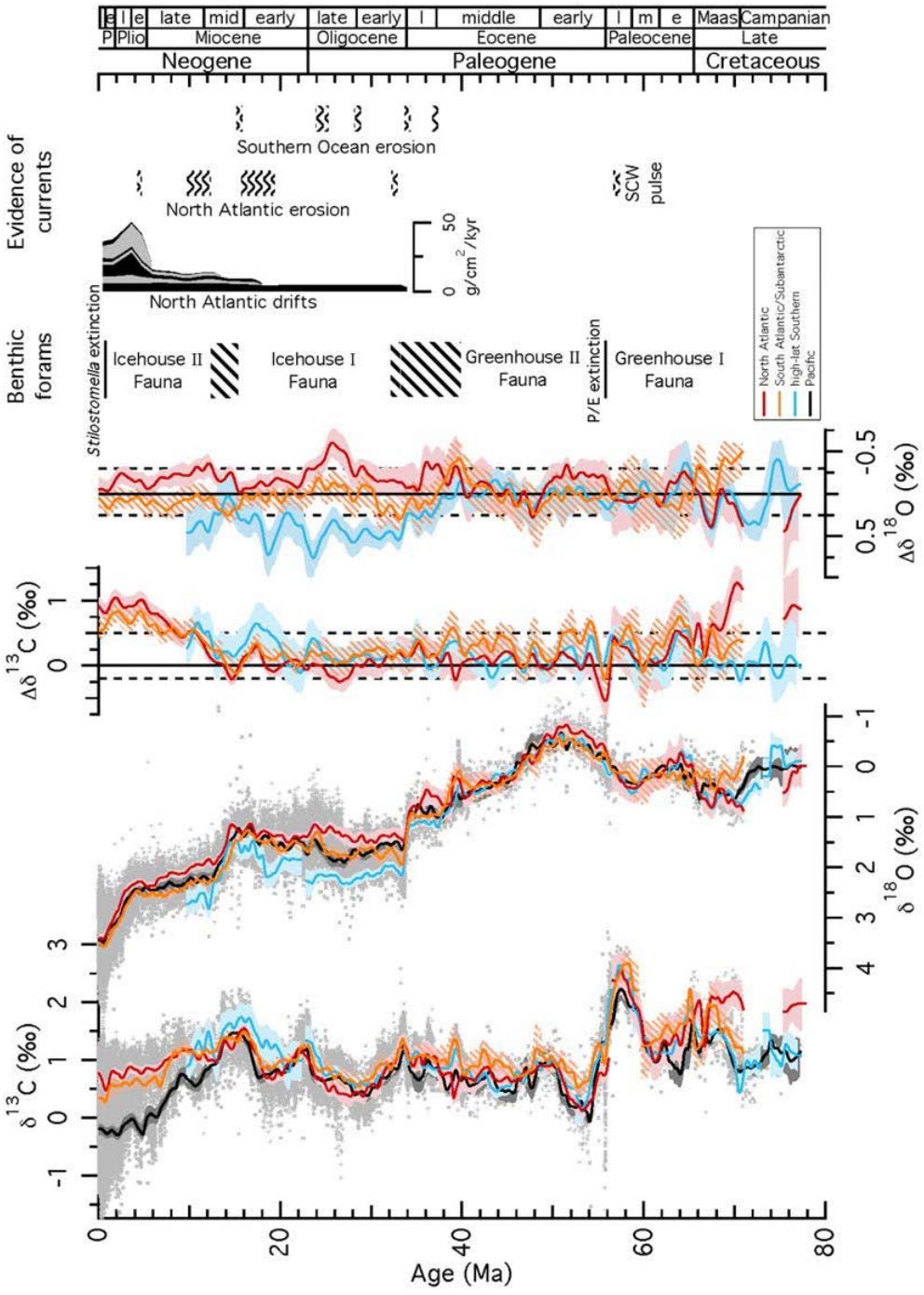

Figure 84: Interbasinal isotopic analysis, from Cramer et al., (2009). The middle two plots, labeled as $\Delta\delta^{13}C$ and $\Delta\delta^{18}O$, outline mean basinal shifts in the surface-benthic gradient of $\delta^{13}C$ and $\delta^{18}O$ respectively.

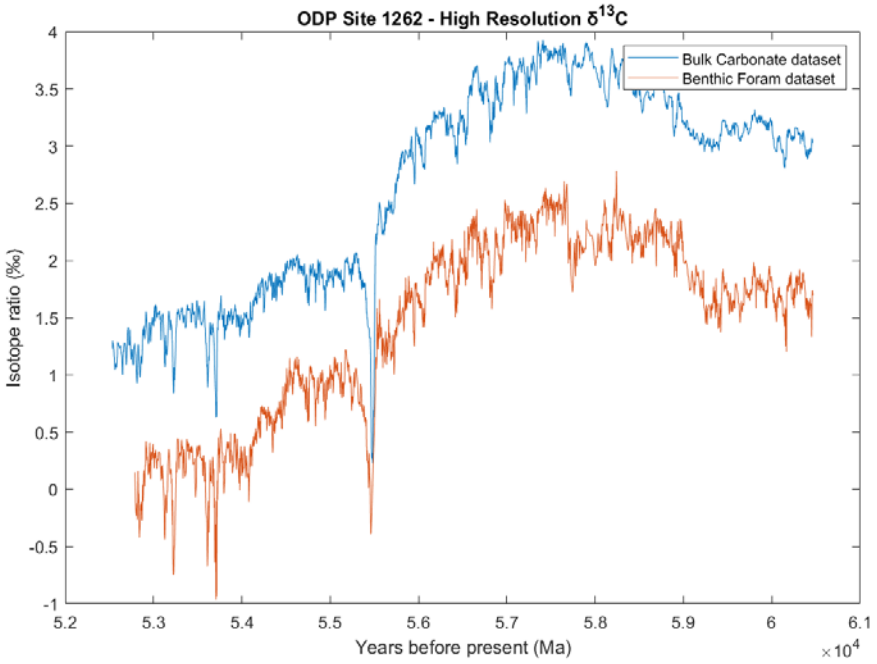

Figure 85: High-resolution $\delta^{13}C$ datasets from ODP Site 1262; data from Littler et al. (2014).

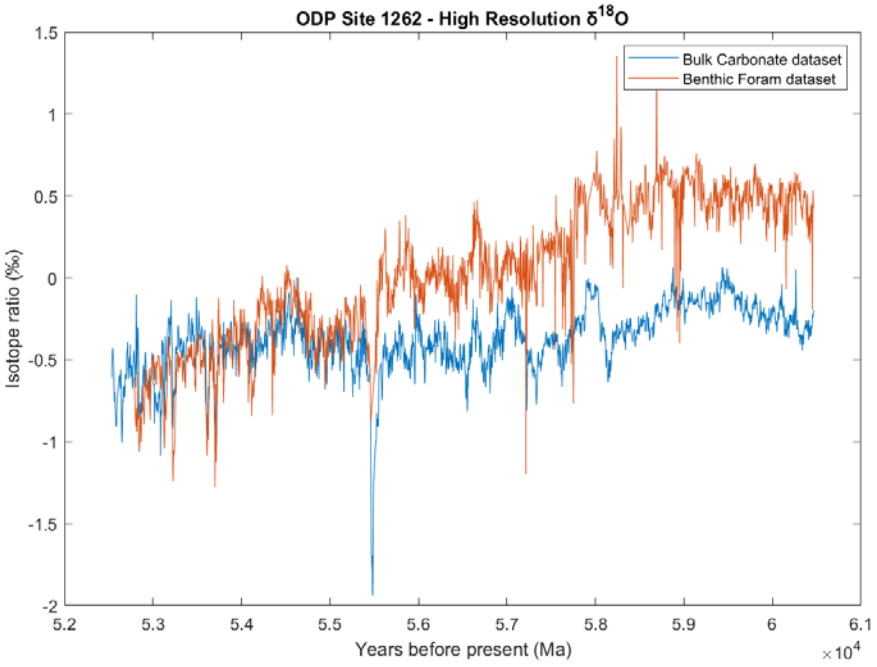

Figure 86: High-resolution $\delta^{13}C$ datasets from ODP Site 1262; data from Littler et al. (2014).

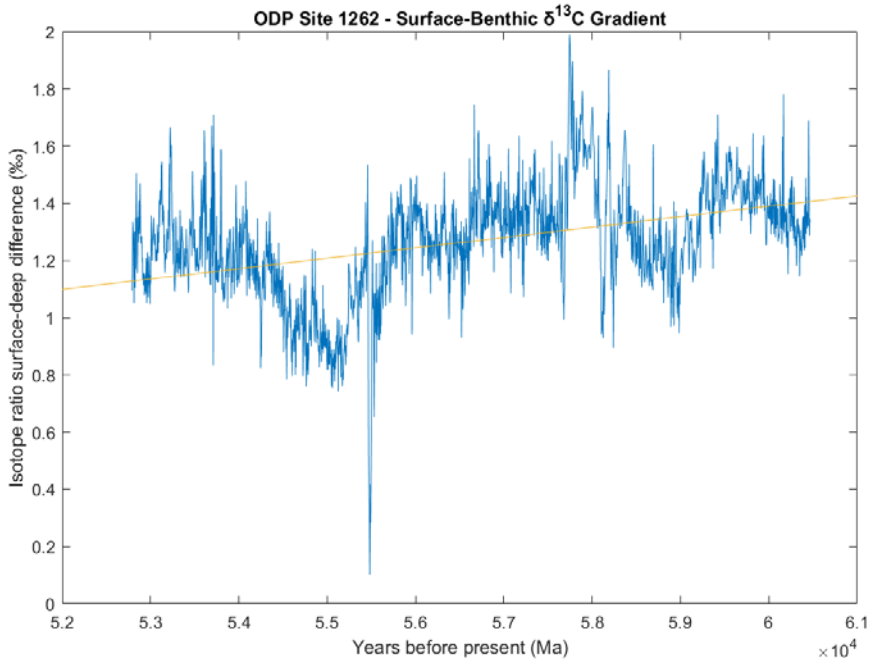

Figure 87: Surface-benthic gradient of $\delta^{13}C$ utilizing the above datasets from Littler et al. (2014). The linear regression has been plotted in yellow.

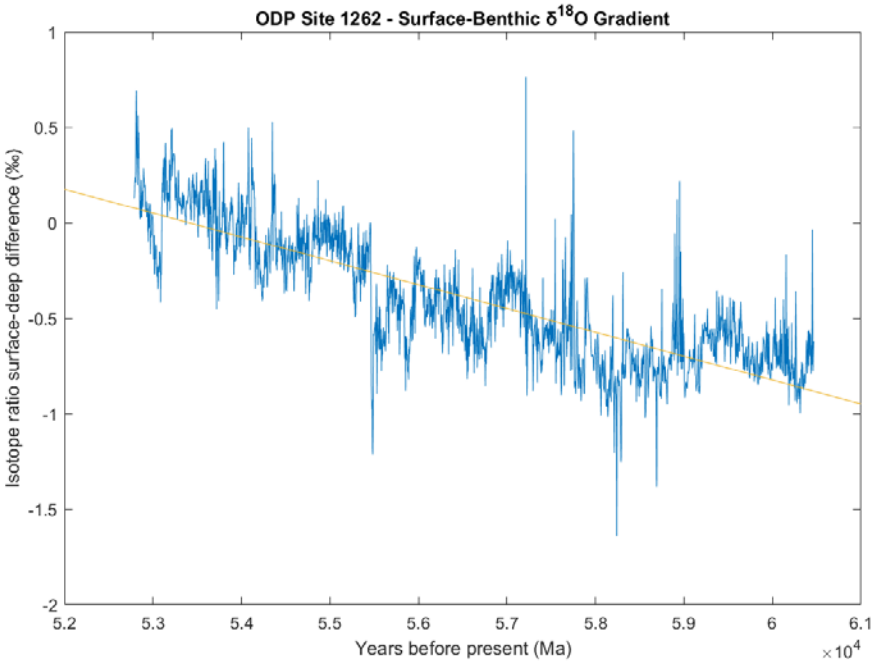

Figure 88: Surface-benthic gradient of $\delta^{18}O$ utilizing the above datasets from Littler et al. (2014). The linear regression has been plotted in yellow.

The surface-deep $\delta^{18}O$ gradient at ODP Site 1262 shows surface temperature as significantly higher than bottom water temperatures at the start of the dataset, with this difference decreasing with time. Since ODP Site 1263 is situated in the southern Atlantic, where the presence of overturning conditions would result in surface temperatures that should be expected to more closely approximate deep ocean temperatures, this pattern is logically sound. The reversal of the gradient, however, is suspect. It is unrealistic that warmer would exist at benthic depths below cooler water at the surface for long intervals of time. The surface-deep $\delta^{18}O$ gradient at ODP Site 1258, however, stays negative throughout the duration of the dataset, showing that temperatures stayed consistently higher at the surface compared to benthic depths. The gradient reversal is not present in the ODP Site 1258 dataset. The most parsimonious interpretation for this reversal is that the lower surface temperatures in the 1262 data are an artifact. Bulk carbonate isotopic datasets may contain large amounts of diagenetic calcite, which tends to skew surface $\delta^{18}O$ values to heavier values (Baker et al., 1982). Therefore, careful consideration is needed when comparing pure benthic foraminiferal carbonate isotope values to those from bulk carbonates. Zachos et al. (2010) has pointed out that bulk carbonate samples from ODP Site 1262 have notable diagenesis of calcite, so this is within the realm of expectation. The surface-deep $\delta^{18}O$ gradient generated from the ODP Site 1258 also happens to contain some "reversals", but these didn't appear to affect the overall trend in any significant way. Gradient reversals aside, the $\delta^{18}O$ data collected from ODP Site 1262 point to deep water temperatures that gradually more closely match surface temperatures until the gradient reaches an eventual minimum, which contrasts with the

only very slight variations in the surface-deep temperature gradient observed at ODP Site 1258. I believe that the more dramatic changes in the gradient local to the southern Atlantic site differentiate it as a region where overturning took place, while the minor fluctuation in the gradient seen in the equatorial Atlantic is indicative only of a signal overprinting that resulted from volcanic fluxes to the DIC pool. The large decreases in the $\delta^{18}O$ gradient that we see at ODP Site 1262 suggest greater vertical mixing had to take place to equalize surface and deep ocean temperatures.

4.3 – SHORTCOMINGS AND FUTURE PATHS

One clear missing piece from my cGENIE experiments is a representation of organic carbon deposition that can change in conjunction with changes in atmospheric CO_2 and temperature. With a more complete carbon cycle, I may have been able to produce model results that more closely matched the data published in the Cramer et al. (2009) compilation, and I would have been more able to confidently match various carbon cycle scenarios to late Paleocene to early Eocene climate trends. New developments in cGENIE allow the preservation of organic carbon in sediments (Hülse et al., 2018). Utilizing this model in future cGENIE experiments would allow for more complete evaluation of carbon-cycle processes that might be responsible for the combined temperature and $\delta^{13}C$ characteristics of EECO and thus achieve stronger agreement with published data. Finally, it would also be prudent to toggle the activity of biological productivity in the model, in order to test its impact on benthic $\delta^{13}C$ patterns.

Additionally, we are continuing to extend the ODP Site 1258 benthic dataset to the entire duration covered by the existing bulk isotope dataset. When complete, it will be possible to compare the surface-benthic isotope gradients from 49.7-54.4 Ma, overlapping the Site 1262 records. The complete dataset will allow for a broader examination of how the surface to deep gradient changes across the warming leading into EECO and up to the onset of global cooling.

CHAPTER 5 – SUMMARY

My analysis of site-wise decompositions of the Cramer et al. (2009) dataset has shown that the asynchronicity between benthic-level $\delta^{13}C$ and $\delta^{18}O$ during EECO has regional variability in size, which roughly corresponds to an increased offset between the carbon and oxygen isotope signals with increased distance from the equator. My cGENIE model experiments, in turn, showed that enhanced volcanic outgassing produces significant variability in benthic DIC $\delta^{13}C$ patterns across space. Therefore, it is apparent that changes in ocean overturning and deep-water circulation during EECO are part of the story in understanding the asynchronicity. Although the lack of organic carbon burial in my cGENIE experiments has prevented a precise pinpointing of the drivers of EECO as recorded in the fossil isotope record, the fact that even volcanic outgassing alone can produce regionally-unique benthic signals rather than globally uniform shifts is very significant in its own right. With the creation of a new high-resolution benthic isotopic dataset from ODP Site 1258 to provide a higher resolution understanding of the equatorial Atlantic during EECO, I have also gained additional insight to the changing

input of deepwater into the region, finding that the gradually decreasing surface-benthic gradient in $\delta^{13}C$ indicates gradual introduction of more freshly-overturned water in the region during the later portions of the EECO event. This concurs with global isotopic patterns observed in the composite dataset from Cramer et al. (2009). With future work, we may be able to more precisely model the climate forcing that led to the warmest temperatures of the entire Cenozoic Era.

BIBLIOGRAPHY

Baker, P. A., Gieskes, J. M., and Elderfield, H. J. J. o. S. R., 1982, Diagenesis of carbonates in deep-sea sediments; evidence from Sr/Ca ratios and interstitial dissolved Sr (super 2+) data, v. 52, no. 1, p. 71-82.

Bemis, B. E., Spero, H. J., Bijma, J., and Lea, D. W. J. P., 1998, Reevaluation of the oxygen isotopic composition of planktonic foraminifera: Experimental results and revised paleotemperature equations, v. 13, no. 2, p. 150-160.

Bice, K. L., and Norris, R. D., Data report: Stable isotope ratios of foraminifers from ODP Leg 207, Sites 1257, 1258, and 1260 and a cleaning procedure for foraminifers in organic-rich shales, *in* Proceedings Proc. Ocean Drill. Program Sci. Results2005, Volume 207.

Cao, L., Eby, M., Ridgwell, A., Caldeira, K., Archer, D., Ishida, A., Joos, F., Matsumoto, K., Mikolajewicz, U., and Moucher, A. J. B., 2009, The role of ocean transport in the uptake of anthropogenic CO2, v. 6, p. 375-390.

Cramer, B., Toggweiler, J., Wright, J., Katz, M., Miller, K. J. P., and Paleoclimatology, 2009, Ocean overturning since the Late Cretaceous: Inferences from a new benthic foraminiferal isotope compilation, v. 24, no. 4.

Dickson, A. J., Cohen, A. S., Coe, A. L., Davies, M., Shcherbinina, E. A., and Gavrilov, Y. O. J. P., Palaeoclimatology, Palaeoecology, 2015, Evidence for weathering and volcanism during the PETM from Arctic Ocean and Peri-Tethys osmium isotope records, v. 438, p. 300-307.

Edwards, N. R., and Marsh, R. J. C. D., 2005, Uncertainties due to transport-parameter sensitivity in an efficient 3-D ocean-climate model, v. 24, no. 4, p. 415-433.

Egger, H., and Brückl, E. J. I. J. o. E. S., 2006, Gigantic volcanic eruptions and climatic change in the early Eocene, v. 95, no. 6, p. 1065-1070.

Eldrett, J. S., Harding, I. C., Firth, J. V., and Roberts, A. P. J. M. G., 2004, Magnetostratigraphic calibration of Eocene–Oligocene dinoflagellate cyst biostratigraphy from the Norwegian–Greenland Sea, v. 204, no. 1, p. 91-127.

Epstein, S., and Mayeda, T. J. G. e. c. a., 1953, Variation of O18 content of waters from natural sources, v. 4, no. 5, p. 213-224.

Freeman, K. H., and Hayes, J. J. G. B. C., 1992, Fractionation of carbon isotopes by phytoplankton and estimates of ancient CO2 levels, v. 6, no. 2, p. 185-198.

Friedman, I., O'NEIL, J., and Cebula, G. J. G. N., 1982, Two new carbonate stable-isotope standards, v. 6, no. 1, p. 11-12.

Hayes, J. M., Strauss, H., and Kaufman, A. J. J. C. G., 1999, The abundance of 13C in marine organic matter and isotopic fractionation in the global biogeochemical cycle of carbon during the past 800 Ma, v. 161, no. 1-3, p. 103-125.

Hülse, D., Arndt, S., Daines, S., Regnier, P., and Ridgwell, A. J. G. M. D., 2018, OMEN-SED 1.0: a novel, numerically efficient organic matter sediment diagenesis module for coupling to Earth system models, v. 11, no. 7, p. 2649-2689.

Katz, M. E., Katz, D. R., Wright, J. D., Miller, K. G., Pak, D. K., Shackleton, N. J., Thomas, E. J. P., and Paleoclimatology, 2003, Early Cenozoic benthic foraminiferal isotopes: Species reliability and interspecies correction factors, v. 18, no. 2.

Kim, S.-T., and O'Neil, J. R. J. G. e. C. A., 1997, Equilibrium and nonequilibrium oxygen isotope effects in synthetic carbonates, v. 61, no. 16, p. 3461-3475.

Komar, N., Zeebe, R., and Dickens, G. J. P., 2013, Understanding long-term carbon cycle trends: The late Paleocene through the early Eocene, v. 28, no. 4, p. 650-662.

Kroopnick, P., Weiss, R., Craig, H. J. E., and Letters, P. S., 1972, Total CO2, 13C, and dissolved oxygen-18O at Geosecs II in the North Atlantic, v. 16, no. 1, p. 103-110.

Kump, L. R., and Arthur, M. A. J. C. G., 1999, Interpreting carbon-isotope excursions: carbonates and organic matter, v. 161, no. 1-3, p. 181-198.

Littler, K., Röhl, U., Westerhold, T., Zachos, J. C. J. E., and Letters, P. S., 2014, A high-resolution benthic stable-isotope record for the South Atlantic: Implications for orbital-scale changes in Late Paleocene–Early Eocene climate and carbon cycling, v. 401, p. 18-30.

McCrea, J. M. J. T. J. o. C. P., 1950, On the isotopic chemistry of carbonates and a paleotemperature scale, v. 18, no. 6, p. 849-857.

Raymo, M. E., and Ruddiman, W. F. J. N., 1992, Tectonic forcing of late Cenozoic climate, v. 359, no. 6391, p. 117.

Ridgwell, A., Hargreaves, J., Edwards, N. R., Annan, J., Lenton, T. M., Marsh, R., Yool, A., and Watson, A. J. B., 2007, Marine geochemical data assimilation in an efficient Earth System Model of global biogeochemical cycling, v. 4, no. 1, p. 87-104.

Ridgwell, A., and Schmidt, D. N. J. N. G., 2010, Past constraints on the vulnerability of marine calcifiers to massive carbon dioxide release, v. 3, no. 3, p. 196.

Saunders, A., Fitton, J., Kerr, A., Norry, M., Kent, R. J. L. i. p. C., oceanic,, and volcanism, p. f., 1997, The north Atlantic igneous province, v. 100, p. 45-93.

Schmitz, M. D., and Davydov, V. I. J. G. B., 2012, Quantitative radiometric and biostratigraphic calibration of the Pennsylvanian–Early Permian (Cisuralian) time scale and pan-Euramerican chronostratigraphic correlation, v. 124, no. 3-4, p. 549-577.

Shackleton, N. J. G. S., London, Special Publications, 1987, The carbon isotope record of the Cenozoic: History of organic carbon burial and of oxygen in the ocean and atmosphere, v. 26, no. 1, p. 423-434.

Spero, H. J., Bijma, J., Lea, D. W., and Bemis, B. E. J. N., 1997, Effect of seawater carbonate concentration on foraminiferal carbon and oxygen isotopes, v. 390, no. 6659, p. 497.

Thomas, E., and Shackleton, N. J. J. G. S., London, Special Publications, 1996, The Paleocene-Eocene benthic foraminiferal extinction and stable isotope anomalies, v. 101, no. 1, p. 401-441.

Turner, S. K., Sexton, P. F., Charles, C. D., and Norris, R. D. J. N. G., 2014, Persistence of carbon release events through the peak of early Eocene global warmth, v. 7, no. 10, p. 748-751.

Weaver, A. J., Eby, M., Wiebe, E. C., Bitz, C. M., Duffy, P. B., Ewen, T. L., Fanning, A. F., Holland, M. M., MacFadyen, A., and Matthews, H. D. J. A.-O., 2001, The UVic Earth System Climate Model: Model description, climatology, and applications to past, present and future climates, v. 39, no. 4, p. 361-428.

Westerhold, T., and Röhl, U. J. C. o. t. P., 2009, High resolution cyclostratigraphy of the early Eocene–new insights into the origin of the Cenozoic cooling trend, v. 5, no. 3, p. 309-327.

Zachos, J., Pagani, M., Sloan, L., Thomas, E., and Billups, K. J. s., 2001, Trends, rhythms, and aberrations in global climate 65 Ma to present, v. 292, no. 5517, p. 686-693.

Zachos, J. C., Dickens, G. R., and Zeebe, R. E. J. N., 2008, An early Cenozoic perspective on greenhouse warming and carbon-cycle dynamics, v. 451, no. 7176, p. 279.

Zachos, J. C., McCarren, H. K., Murphy, B., Röhl, U., and Westerhold, T., 2010, (Figure 2) Stable carbon and oxygen isotope records of ODP Site 208-1262, Supplement to: Zachos, JC et al. (2010): Tempo and scale of late Paleocene and early Eocene carbon isotope cycles: Implications for the origin of hyperthermals. Earth and Planetary Science Letters, 299(1-2), 242-249, https://doi.org/10.1016/j.epsl.2010.09.004, PANGAEA.

Zeebe, R. E., Zachos, J. C., and Dickens, G. R. J. N. G., 2009, Carbon dioxide forcing alone insufficient to explain Palaeocene–Eocene Thermal Maximum warming, v. 2, no. 8, p. 576.